

CHARACTERIZING THE INORGANIC/ORGANIC INTERFACE IN  
CANCER BONE METASTASIS

A Dissertation

Presented to the Faculty of the Graduate School

of Cornell University

In Partial Fulfillment of the Requirements for the Degree of

Doctor of Philosophy

By

Fei Wu

August 2016

© 2016 Fei Wu

# CHARACTERIZING THE INORGANIC/ORGANIC INTERFACE IN CANCER BONE METASTASIS

Fei Wu, Ph.D.  
Cornell University 2016

Bone metastasis frequently occurs in patients with advanced breast cancer and remains a major source of mortality. At the molecular level, bone is a nanocomposite composed of inorganic bone mineral deposited within an organic extracellular matrix (ECM). Although the exact mechanisms of bone metastasis remain unclear, the nanoscale materials properties of bone mineral have been implicated in this process. Bone apatite is closely related to synthetic hydroxyapatite (HAP,  $\text{Ca}_{10}(\text{PO}_4)_6(\text{OH})_2$ ) in terms of structural and mechanical properties. Additionally, although the primary protein content of bone is collagen I, the glycoprotein fibronectin (Fn) is essential in maintaining the overall integrity of the bone matrix. Importantly, *in vivo*, neither breast cancer cells nor normal bone cells interact directly with the bone mineral but rather with the protein film adsorbed onto the mineral surface. Therefore, we hypothesized that breast cancer cell functions were regulated by differential fibronectin adsorption onto hydroxyapatite, which led to pathological remodeling of the bone matrix and sustained bone metastasis.

Three model systems containing HAP and Fn were developed for this thesis. In model system I, a library of synthetic HAP nanoparticles were utilized to investigate the effect of mineral size, shape, and crystallinity on Fn conformation, using Förster resonance energy transfer (FRET) spectroscopy. In model system II, Fn-functionalized large geologic HAP crystals were used instead of HAP nanoparticles to avoid cellular uptake when investigating

subsequent cell functions. Overall our FRET analysis (models I and II) revealed that Fn conformation depended on size, surface chemistry, and roughness of underlying HAP. When breast cancer cells were seeded on the Fn-coated HAP crystal facets (model II), our data indicated high secretion levels of proangiogenic and proinflammatory factors associated with the presence of unfolded Fn conformations, likely caused by differential engagement of cell receptors integrins with the underlying Fn. Finally, in model system III, Fn fibrillar structures (mimicking the bone matrix) were fabricated and characterized in presence of HAP nanoparticles, suggesting that the presence of microcalcifications found in tumorous/inflamed tissues affects both the structural and mechanical properties of the surrounding ECM.

Collectively, our study of cellular behavior regulated by mineral/ECM interactions provides insights into the pathogenesis of breast cancer bone metastasis as well as other HAP-related inflammation.

## BIOGRAPHICAL SKETCH

Fei Wu was born in 1988 to Maoyuan Wu and Chuanfen Xu in Rizhao, Shandong, China. She grew up as top of her class, receiving various awards in math and Chinese painting competitions. She found true pleasure and a sense of accomplishment in learning, and desired to explore science for benefiting humans' welfare. After graduating ranked number one from Rizhao First High School in June 2007, she went on to pursue her interest in science at Fudan University in Shanghai, China.

At Fudan University, she chose Macromolecular Materials and Engineering as desired field of study. She joined Prof. Huisheng Peng's research group focused on polymer/carbon nanotube composites as an undergraduate research assistant in 2009. Later she became the project leader of a senior project studying block copolymer self-assembly, funded by FDUROP in 2010. During summer vacation, she participated in social services to protect local dialect in Nanhui, Shanghai. While studying at Fudan, she became more and more interested in materials for biomedical applications, and decided to pursue graduate study in this area in the US.

Fei joined Prof. Delphine Gourdon's research group in the Department of Materials Science and Engineering at Cornell University in August 2011. She has worked on many projects towards developing biomaterials platforms to understand the mechanisms implicated in breast cancer metastasis to bone. During her Ph.D. study, she has published three peer reviewed journal articles and presented at six conferences. She will become the first person in the family history to have earned a Ph.D. in August, 2016. After graduation, Fei will continue pursuing her interest in the application of biomedical materials to help develop next generation life science tools and improve people's healthcare.

## DEDICATION

To my family

## ACKNOWLEDGEMENTS

This work would not have been possible without the support and mentorship of many individuals and funding agencies. I would like to thank first and foremost, my advisor and committee chair Professor Delphine Gourdon for her mentorship and enthusiasm throughout my study at Cornell University. She has been an incredible support and inspiration. To my committee members Professor Lara Estroff and Professor Eve Donnelly, thank you for being supportive. To my collaborators Professor Lara Estroff and Professor Claudia Fischbach-Teschl, and their group members, thank you for welcoming me to your lab. To my group members, especially Dr. Karin Wang, Dr. Roberto Carlos Andresen Eguiluz, Sierra Cook, Weisi Chen, Brian Gillis, and Jinho Chang, thank you for your help. To wonderful facility managers and staff at Cornell, Dr. Michael Rutzke (SCS), Carol Bayles (BRC), Maura Weathers (CCMR), and John Grazul (CCMR). To my family for their love and cheers. I would also like to thank my funding sources, the National Science Foundation, the National Institutes of Health, the Cornell Center for Materials Research, the Nanobiotechnology Center, and Professor Gourdon.

## TABLE OF CONTENTS

Biographical Sketch.....	iii
Dedication.....	iv
Acknowledgements.....	v
List of Figures.....	xiii
List of Tables.....	xxi
List of Abbreviations .....	xxii
Chapter 1. Introduction.....	1
1.1 Background and motivation.....	1
1.2 Experimental design.....	6
1.3 Thesis overview.....	9
1.4 Conclusions.....	11
References.....	13
Chapter 2. Differential Fibronectin Adsorption on Synthetic Hydroxyapatite Nanoparticles: Effect of Size, Shape, and Crystallinity.....	19
2.1 Abstract.....	19
2.2 Introduction.....	20
2.3 Materials and methods.....	23
2.3.1 Hydroxyapatite nanoparticle synthesis.....	23
2.3.2 Hydroxyapatite nanoparticles characterization .....	24
2.3.3 Fibronectin and FRET labeling.....	25
2.3.4 Fabrication of 2D platforms.....	26
2.3.5 FRET data acquisition.....	26
2.3.6 Statistical analysis.....	27
2.4 Results.....	27
2.4.1 Hydroxyapatite nanoparticles characterization.....	27
2.4.2 Fibronectin deposition and conformation at various hydroxyapatite concentrations....	32
2.4.3 Size and Morphology of hydroxyapatite nanoparticle agglomerates.....	37
2.5 Discussion.....	40
2.5.1 Effect of hydroxyapatite nanoparticle surface chemistry on fibronectin adsorption....	41
2.5.2 Evolving size and morphology of hydroxyapatite agglomerates with increasing particle concentration.....	43
2.5.3 Effect of hydroxyapatite agglomerate size and morphology on fibronectin adsorption.....	44
2.6 Conclusions.....	48
References.....	49
Chapter 3. Differential Fibronectin Adsorption on Geologic Apatite Crystal Facets: Effect of Surface Chemistry and Roughness.....	55

3.1 Abstract.....	55
3.2 Introduction.....	56
3.3 Materials and methods.....	59
3.3.1 Geologic apatite crystals.....	59
3.3.2 HAP facets preparation.....	59
3.3.3 HAP surface chemistry and roughness characterization.....	60
3.3.4 Fibronectin FRET labeling and adsorption.....	60
3.3.5 FRET data acquisition.....	61
3.3.6 Statistical analysis.....	62
3.4 Results.....	62
3.4.1 Apatite crystal bulk properties.....	62
3.4.2 HAP facets with controlled surface chemistry and roughness.....	63
3.4.3 Fibronectin deposition and conformation on hydroxyapatite facets.....	67
3.5 Discussion.....	72
3.6 Conclusions.....	76
References.....	78

Chapter 4. Fibronectin-Mediated Breast Cancer Cells Interactions with Geologic Apatite Crystal Facets.....83

4.1 Abstract.....	83
4.2 Introduction.....	84
4.3 Materials and methods.....	86
4.3.1 Cell culture and seeding.....	86
4.3.2 Cell viability and adhesion assay.....	88
4.3.3 Immunostaining and confocal imaging.....	89
4.3.4 VEGF and IL-8 secretion.....	90
4.3.5 HAP facets cleaning.....	90
4.3.6 Statistical analysis.....	90
4.4 Results.....	91
4.4.1 Breast cancer cell viability.....	91
4.4.2 Breast cancer cell adhesion.....	93
4.4.3 Focal adhesion formation.....	94
4.4.4 VEGF secretion.....	97
4.4.5 IL-8 secretion.....	98
4.5 Discussion.....	100
4.6 Conclusions.....	104
References.....	106

Chapter 5. Osteoblast-like Cell Functions on Fibronectin-coated Geologic Apatite Crystal Facets.....110

5.1 Abstract.....	110
5.2 Introduction.....	111
5.3 Materials and methods.....	114

5.3.1 Cell culture and seeding.....	114
5.3.2 Cell viability and adhesion assay.....	115
5.3.3 Immunostaining and confocal imaging.....	116
5.3.4 HAP facets cleaning.....	117
5.3.5 Statistical analysis.....	117
5.4 Results.....	117
5.4.1 Pre-osteoblast cell viability.....	117
5.4.2 Pre-osteoblast cell adhesion.....	118
5.4.3 Focal adhesion formation.....	119
5.5 Discussion.....	123
5.6 Conclusions.....	127
References.....	129
Chapter 6. Conclusions and Future Directions.....	134
References.....	137
Appendix A. Altered Conformational and Mechanical Properties of Fibronectin Fibers in Presence of Hydroxyapatite Nanoparticles.....	139
A.1 Introduction.....	139
A.2 Materials and methods.....	141
A.2.1 HAP nanoparticles synthesis and characterization.....	141
A.2.2 Fabrication of Fn fibers and Fn-HAP composite fibers.....	141
A.2.3 PDMS surface modification and strain device.....	142
A.2.4 FRET confocal imaging.....	142
A.2.5 MEMS device.....	143
A.2.6 TEM imaging.....	143
A.3 Results and Discussion.....	143
A.4 Outlook.....	154
References.....	155
Appendix B. Fibronectin Conformation on Mica Surfaces as a Function of Curvature.....	157
B.1 Introduction.....	157
B.2 Materials and methods.....	157
B.2.1 Preparation of mica surfaces.....	157
B.2.2 FRET imaging and analysis.....	158
B.2.3 Statistical analysis.....	158
B.3 Results and Discussion.....	158
B.4 Outlook.....	160
References.....	161

## LIST OF FIGURES

<b>Figure 2.1.</b> pXRD pattern and FTIR spectra of HAP nanoparticles. The phase of both HAP1 and HAP2 was confirmed to be pure HAP, major peaks labeled with Miller indices.....	28
<b>Figure 2.2.</b> TEM images of dialyzed HAP1 and HAP2 nanoparticles synthesized through a wet precipitation method (hydrothermal treatment for 6 days).....	30
<b>Figure 2.3.</b> Size distributions along c-axis of HAP and HAP2 nanoparticles (TEM).....	31
<b>Figure 2.4.</b> Zeta potential of HAP nanoparticles at various concentrations in PBS.....	32
<b>Figure 2.5.</b> Confocal images for 0.05 mg/mL HAP1 nanoparticles incubated with Fn: (A) Donor channel, (B) acceptor channel, and (C) transmission light channel. (D) Color-coded FRET ratio map, with high FRET ratio color coded in red (compact Fn) and low FRET ratio in blue (unfolded Fn). (E) FRET ratio histogram for the same field of view.....	34
<b>Figure 2.6.</b> Soluble calibration of FRET ratio ( <i>i.e.</i> , acceptor intensity/donor intensity) as a function of chemical denaturant (guanidine hydrochloride, GdnHCl) concentration.....	35
<b>Figure 2.7.</b> (A) FRET ratio and (B) amount of Fn adsorbed onto HAP1 and HAP2 at various HAP concentrations, after incubation at 4 °C for 24 hrs. As a comparison, FRET ratio and quantity of Fn adsorbed onto coverglass (in absence of HAP) are indicated by green arrows.....	36
<b>Figure 2.8.</b> Confocal z-stack 3D reconstruction: size and morphology of HAP1 nanoparticle agglomerates at (A) 0.01 mg/mL, (B) 0.05 mg/mL, and (C) 0.1 mg/mL incubated with Fn in PBS.....	38

**Figure 2.9.** Confocal z-stack 3D reconstruction: size and morphology of HAP2 nanoparticle agglomerates at (A) 0.01 mg/mL, (B) 0.05 mg/mL, and (C) 0.1 mg/mL incubated with Fn in PBS.....39

**Figure 2.10.** Mechanisms proposed for the effect of HAP materials properties on Fn adsorption: (A) effect of HAP surface charge and (B) effect of HAP agglomerate size and morphology.....41

**Figure 2.11.** FRET ratios of Fn adsorbed as a function of z height at (A) 0.01 mg/mL, (B) 0.05 mg/mL, and (C) 0.1 mg/mL HAP nanoparticles.....46

**Figure 3.1** (A) Elemental compositions of geologic apatite crystals G1, G2, and G3 were determined by ICP-AES analysis. Only elements with concentrations larger than 0.01 mg/L are shown. (B) pXRD patterns of G1, G2, and G3.....63

**Figure 3.2** Representative (A) AFM image of a smooth HAP facet and (B) optical profiler image of a rough HAP facet, with the line profile of a cross section marked in green shown at the bottom of each image.....65

**Figure 3.3** Linear regression fit for zeta potentials measured as a function of surface displacement. Y intercept at zero displacement of each linear regression fit was subtracted from zeta potential of tracer particles to extrapolate the surface zeta potential for each HAP facet.....67

**Figure 3.4** Confocal images for a rough HAP facet coated with FRET labeled Fn: (A) donor channel, (B) acceptor channel, and (C) transmission light channel. (D) Color-coded FRET ratio map, with high FRET ratio color coded in red (compact Fn) and low FRET ratio in blue

(unfolded Fn). (E) FRET ratio histogram with schematics of Fn conformation correlated to the FRET calibration values.....68

**Figure 3.5** Soluble calibration of FRET ratio (*i.e.*, acceptor intensity/donor intensity) as a function of chemical denaturant (guanidine hydrochloride, GdnHCl) concentration. The schematics at left illustrate Fn conformations at various FRET ratios obtained via circular dichroism measurements.....69

**Figure 3.6** Confocal images for a smooth HAP facet coated with FRET labeled Fn: (A) donor channel, (B) acceptor channel, and (C) transmission light channel. (D) Color-coded FRET ratio map for region of analysis (region in focus), with high FRET ratio color coded in red (compact Fn) and low FRET ratio in blue (unfolded Fn). (E) FRET ratio histogram for region of analysis, with schematics of Fn conformation correlated to the FRET calibration values.....70

**Figure 3.7** (A) FRET ratios and (B) amount of Fn adsorbed onto HAP facets with varied surface chemistry and roughness, after incubation at 4 °C for 24 h. Coverglasses coated with FRET labeled Fn were used as control surfaces in all experiments.....71

**Figure 3.8** Common facets observed in hexagonal hydroxyapatite crystal. {100} and {001} are equivalent in the hexagonal lattice.....74

**Figure 3.9** Schematic of how surface chemistry or topography affect Fn conformation and deposition.....76

**Figure 4.1** Preparation of HAP/PDMS system for cell culture studies.....88

**Figure 4.2** Merged fluorescence image acquired for Live/Dead assay. Live cells were stained in green and dead cells were stained in red.....92

**Figure 4.3** MDA-MB-231 breast cancer cell viability after seeding for either (A) 6 h or (B) 24 h on Fn coated HAP facets and control coverglass, as quantified via Live/Dead assay.....93

**Figure 4.4** MDA-MB-231 breast cancer cell adhesion after initial seeding for either (A) 6 h or (B) 24 h on Fn coated HAP facets and control coverglass, as quantified by the number of live cells via Live/Dead assay.....94

**Figure 4.5** Representative confocal images of immunostained vinculin in MDA-MB-231 cells seeded on Fn coated (A) (100)S, (B) (001)S, (C) (100)R, and (D) (001)R HAP facets, after 24 h in culture.....95

**Figure 4.6** Focal adhesion (FA) analysis of MDA-MB-231 cells on Fn coated HAP facets after culturing for 24 h: (A) the number of FAs formed per cell, (B) FA area, (C) FA length, and (D) FA width. FA area, length, and width were obtained by fitting ellipse for each FA (ImageJ). Vinculin was immunostained for visualizing FAs.....96

**Figure 4.7** Frequency distributions of (A) FA area, (B) FA length, and (C) FA width in MDA-MB-231 cells seeded on Fn coated HAP facets, after 24 h in culture.....97

**Figure 4.8** VEGF secretion by MDA-MB-231 breast cancer cells as analyzed via ELISA assay of media collected either (A) 6 h or (B) 24 h after initial seeding on Fn coated HAP facets and control coverglass. Values were normalized by the number of live cells adhered.....98

**Figure 4.9** IL-8 secretion by MDA-MB-231 breast cancer cells as analyzed via ELISA assay of media collected (A) 6 h and (B) 24 h after initial seeding on Fn coated HAP facets and control coverglass. Values were normalized by the number of live cells adhered.....99

**Figure 5.1** Live/Dead confocal images acquired for (A) 100S, (B) 001S, (C) 100R, and (D) 001R after culturing for 2 h. Live cells were stained in green and dead cells in red. Only one representative confocal tile image is shown for each HAP facet.....118

**Figure 5.2** Number of pre-osteoblasts adhered per unit area after culturing for 2 h on Fn coated HAP facets and control coverglass.....119

**Figure 5.3** Representative confocal images of immunostained vinculin in MC3T3-E1 pre-osteoblast cells seeded on Fn coated (A) 100S, (B) 001S, (C) 100R, and (D) 001R HAP facets.....120

**Figure 5.4** Focal adhesion (FA) analysis of MC3T3-E1 pre-osteoblast cells after culturing for 2 h on Fn coated HAP facets and control coverglass : (A) number of FAs per cell, (B) FA area, (C) FA length, and (D) FA width. Immunofluorescence of vinculin was used to identify and characterize FAs.....122

**Figure 5.5** Frequency distributions of (A) FA area, (B) FA length, and (C) FA width of MC3T3-E1 pre-osteoblast cells seeded on Fn coated HAP facets after culturing for 2 h.....123

**Figure A.1** Fn conformational changes as a function of fiber strain for pure Fn fibers and Fn-HAP1 composite fibers. Fn-HAP1 fibers were pulled from solution containing 0.3 mg/mL Fn and 0.7 mg/mL HAP1 nanoparticles.....145

<b>Figure A.2</b> Schematic of a fiber (yellow) suspended over a trench pulled by the tip on the force sensor. Displacement is the distance that the tip travels.....	147
<b>Figure A.3</b> Fiber diameter measured using confocal bright field images. Fn-HAP1 composite fibers are pulled from solution containing 2 mg/mL HAP1 nanoparticles.....	147
<b>Figure A.4</b> Representative force-strain profile for a Fn-HAP1 composite fiber pulled from solution containing 0.3 mg/mL Fn and 8.4 mg/mL HAP1 nanoparticles.....	148
<b>Figure A.5</b> Stress-strain profile for the same Fn-HAP1 composite fiber as shown in Figure A.4 before slippage occurred.....	149
<b>Figure A.6</b> Young's modulus of the same Fn-HAP1 composite fiber as shown in Figure A.5 before slippage occurred.....	150
<b>Figure A.7</b> Stress-strain curves of pure Fn and Fn-HAP composite fibers. Fn-HAP fibers were pulled from solution containing 0.3 mg/mL Fn and 1 mg/mL HAP1 nanoparticles.....	151
<b>Figure A.8</b> TEM images of Fn-HAP1 composite fibers pulled from solution containing 0.3 mg/mL Fn and either (A) 0.01 mg/mL HAP1 particles or (C) 2 mg/mL HAP1 particles. (B) and (D) are zoomed in images of (A) and (C), respectively.....	152
<b>Figure A.9</b> TEM images of Fn-HAP1 composite fibers pulled from solution containing 0.3 mg/mL Fn and either (A) 0.01 mg/mL HAP1 particles or (C) 2 mg/mL HAP1 particles. (B) and (D) are zoomed in images of (A) and (C), respectively.....	153

**Figure B.1** FRET ratios of Fn molecules adsorbed on freshly cleaved mica surfaces at 4 °C for 24 h: either flat mica or mica surfaces with radius of curvatures of 2 cm (r2), 1 cm (r1), and 0.5 cm (r0.5) were used.....159

## LIST OF TABLES

<b>Table 2.1.</b> Summary of hydrothermal treatment time, sizes and splitting factors of the HAP nanoparticles.....	29
<b>Table 3.1</b> Summary of surface roughness and surface zeta potential of HAP facets.....	66

## LIST OF ABBREVIATIONS

HAP	Hydroxyapatite, $\text{Ca}_{10}(\text{PO}_4)_6(\text{OH})_2$
Fn	Fibronectin
FRET	Förster resonance energy transfer
ECM	Extracellular matrix
AFM	Atomic force microscopy
PBS	Phosphate buffered saline
pXRD	Powder X-ray diffraction
FTIR	Fourier transform infrared spectroscopy
TEM	Transmission electron microscopy
LDE	Laser doppler electrophoresis
GdnHCl	Guanidine hydrochloride
2D	2-dimensional
3D	3-dimensional
VEGF	Vascular endothelial growth factor
IL-8	Interleukin-8
ICP-AES	Inductively coupled plasma atomic emission spectrometry
FA	Focal adhesion
PDMS	Polydimethylsiloxane
DI water	Deionized water
FBS	Fetal bovine serum
P/S	Penicillin/streptomycin
$\alpha$ -MEM	$\alpha$ modification of minimum essential medium
EthD-1	Ethidium homodimer
DMEM/F12	Dulbecco's Modified Eagle Medium: Nutrient Mixture F-12
PBS-X	0.05% Triton-X in phosphate buffered saline
NMWL	Nominal molecular weight limit
SDS	Sodium dodecyl sulfate
GAG	Glycosaminoglycan

PTHrP	Parathyroid hormone-related protein
IL-6	Interleukin-6
IL-11	Interleukin-11
TGF- $\beta$	Transforming growth factor $\beta$
SAM	Self-assembled monolayer
IL-I $\beta$	Interleukin I $\beta$
MEMS	Micro-electro-mechanical system
SFA	Surface forces apparatus

# **Chapter 1.**

## **Introduction**

### **1.1 Background and motivation**

Bone is one of the primary metastatic sites for various common human cancers, including breast cancer and prostate cancer, and is the site of the most significant tumor burden in many patients at advanced stage [1,2]. In order to develop effective treatment for bone metastasis, it is important to understand what characteristics of the bone microenvironment (often radically different from that of the primary tumor) attract and support cancer metastasis, survival, and growth in bone. Bone is a nanocomposite material with hierarchical structure, composed of inorganic bone mineral deposited within an organic fibrillar extracellular matrix (ECM) [3]. This mineralized organic matrix is under constant remodeling by osteoclasts resorbing old matrix and osteoblasts depositing new matrix [4]. Cancer metastasis to bone induces pathological remodeling of the bone matrix by perturbing the balance between bone deposition and bone degradation. The presence of tumor cells alters cell-cell interactions in the bone microenvironment. In the case of breast cancer cells invasion of the bone tissue, osteolysis takes place, induced by suppression of osteoblasts and activation of osteoclasts [5–8]. A well-known model developed to explain this process is the ‘vicious cycle’ model: briefly, tumor cell secretion of growth factors enhances osteoclasts-mediated bone degradation, releasing new growth factors stored in the bone matrix, which further promotes tumor growth and secretion of more growth factors [9]. In addition to cell-cell interactions, it is well acknowledged that cell-matrix interactions also play a critical role in regulating tumor cell fate. There has been increasing

evidence that the nanoscale materials properties of bone apatite may modulate the pathogenesis of breast cancer bone metastasis [7,10,11]. However, the cellular and molecular mechanisms of this process, in particular whether and how the mineral/ECM interface is involved, remains unclear.

Synthetic hydroxyapatite (HAP,  $\text{Ca}_{10}(\text{PO}_4)_6(\text{OH})_2$ ) has been widely used in previous studies to mimic bone apatite by recapitulating several of its materials properties, such as size, crystallinity, and carbonate substitution. Due to bone remodeling, the crystal size, chemical composition, and distribution of bone mineral vary as a function of age and disease progression. Compared with synthetic HAP, bone apatite has lower crystallinity and more substitution ions in the crystal lattice [12–15]. The presence of HAP in polymer scaffolds was reported to increase tumor cell adhesion, proliferation, and secretion of pro-inflammatory factor interleukin-8 (IL-8), which is a potential activator of osteoclast-mediated bone resorption [7,10]. Furthermore, HAP materials properties including nanoparticle size, crystallinity, carbonate incorporation, and morphology of mineral coating, all showed combined and/or individual effects on breast cancer cell growth and secretion [11,16]. However, it remains a challenge to deconvolute the roles of HAP surface chemistry and topography in regulating both cancer and bone cells functions. Furthermore, whether cells sense the mineral materials properties directly or indirectly (via interactions with the organic ECM) also requires investigation.

The bone ECM is composed primarily of collagen I (90%), proteoglycans, and glycoproteins. We focused on the glycoprotein fibronectin (Fn), a 440 kDa dimeric glycoprotein composed of three types of repeating modules among which half of them are mechanically unstable and subject to drastic conformational changes (molecular unfolding) [17]. Fn is the first bone matrix protein deposited by osteoblasts; it plays an essential role in the subsequent deposition of

collagen I and later in maintaining the integrity of the collagen matrix [18–23]. Circulating plasma Fn molecules produced by the liver are also found in the bone matrix [24]. Plasma Fn actually represents the predominant source of Fn affecting bone mineralization and matrix properties, while osteoblast-derived Fn locally modulates osteoblast differentiation without appreciably changing matrix properties [24]. As a critical mechanotransducer, Fn is known to sense and respond to chemical, physical, and mechanical signals from the microenvironment [17,25]. More specifically, the force-induced conformational changes of Fn can regulate the type of binding sites that are exposed or disrupted on the protein. For example, the cell binding domain located on Fn-III<sub>9-10</sub>, which is recognized by cell surface receptors notably integrins, is very sensitive to mechanical strain and its unfolding will lead to differential integrin engagement [26–28]. These conformational-dependent binding events ultimately influence downstream cellular behaviors to regulate or dysregulate homeostasis *in vivo* [29–31]. Previous studies have shown that osteogenesis, osteoblast differentiation, and survival of matured osteoblast all depend on integrin-mediated interactions between osteoblasts and Fn [32,33].

Fn mechanobiology also plays a critical role in regulating tumorigenesis [34]. The up-regulation of Fn in the primary tumor microenvironment has been associated with increased mortality among patients with breast and prostate cancers [35]. As Fn has numerous binding sites for cells, other ECM proteins, and growth factors [20], the conformational changes of Fn can mediate a variety of cancer cell functions including adhesion, proliferation, and proangiogenic/proinflammatory secretion, but also migration and tissue invasion, which are crucial for cells to detach from the primary tumor and start their journey to a metastatic site.

Cancer cell adhesion to the surrounding ECM is an essential step required for cell migration and invasion, a hallmark of the metastatic cascade. As a major ECM adhesive protein, Fn has

been implicated in modulating tumor cell migration, invasion, and apoptotic responses of breast cancer cells [36–38]. Transmembrane receptors notably integrins, a family of 24 ubiquitous  $\alpha/\beta$  heterodimers, have been identified as key regulators in these processes. Each integrin binds to a specific set of extracellular ligands, transducing (in and out) biochemical, physical, and mechanical signals for cells to sense and respond to their microenvironment [39]. During cell attachment to ECM ligands, integrins cluster on the cell surface and act as a platform for recruiting cellular and signaling accessory proteins, forming structures called focal adhesions (FAs) that link the ECM to the actin cytoskeleton. The engagement of different integrins may either enhance or inhibit tumorigenesis during breast cancer progression [40]. For example,  $\beta_1$  integrins play a specific role in regulating breast cancer cell adhesion and spreading, formation of FAs, and cell invasion through complex ECM environments [41]. Thus Fn conformational changes may regulate integrin binding and subsequent cell fate during breast cancer metastasis.

During tumor progression, the formation of new blood vessels, a process called angiogenesis, is critical for tumor growth and metastasis [42]. Tumor cells promote angiogenesis by up-regulating proangiogenic factors [43]. Dysregulated cell-ECM interactions and integrin signaling have been reported to be associated with altered signaling of a major proangiogenic factor, vascular endothelial growth factor (VEGF) [44–46]. A proinflammatory factor, interleukin-8 (IL-8), can also promote angiogenic responses in endothelial cells, increase tumor cell survival and proliferation, and potentiate tumor cell migration and invasion. [10,47,48]. Moreover, IL-8 acts as a mediator of osteolysis induced by bone metastasis, and is dramatically up-regulated in breast cancer cells that preferentially metastasize to bone [7,10]. In fact, a strong correlation has been established between IL-8 expression and the metastatic potential of breast cancer cells [49]. Circulating plasma Fn was also shown to enhance blood vessel formation and facilitate tumor

growth by increasing soluble VEGF contents and VEGF-mediated signaling [35]. Finally, an integrin switch activated by Fn conformational changes that promotes VEGF secretion by breast cancer associated stromal cells has also been identified [45]. Thus Fn mechanobiology may underlie proangiogenic signaling pathways that promote tumor growth and metastasis.

To elucidate whether HAP materials properties alter cellular functions and whether Fn mediates these alterations, two types of cell culture platforms containing HAP and Fn were developed for this thesis. In the first platform developed, a library of HAP nanoparticles was synthesized to investigate the effect of nanoparticle size, shape, and crystallinity on the deposition and conformation of Fn molecules (determined via Förster resonance energy transfer (FRET) mapping). In the second platform developed, geologic HAP crystal facets rather than nanoparticles were used for studying subsequent cellular behaviors to (i) avoid cytotoxicity due to cell uptake of nanoparticles, and (ii) deconvolute the effects of HAP surface chemistry and surface topography/roughness. Our findings indicate that HAP surface chemistry and topography/roughness have both individual and combined effects on adhesion as well as on proangiogenic and pro-inflammatory secretions of breast cancer cells, through Fn-mediated interactions. Osteoblast adhesion and FA assembly were also investigated to understand whether bone remodeling is likewise altered by HAP induced dysregulation of Fn. Our data show differential assembly of FAs depending on both surface chemistry and surface topography, while the latter seemed to play a predominant role. The larger size of FA complexes formed on rough HAP facets was associated with higher amounts of more compact Fn adsorbed, which is likely attributed to the interactions between Fn and osteoblasts surface receptors.

Collectively, our study of the regulation of cell functions (including cell survival, adhesion, FA assembly, and secretion) by inorganic/organic interactions provides insights into the

pathogenesis of cancer bone metastasis as well as other HAP-related inflammation. The altered organic matrix properties caused by interactions with inorganic minerals may provide niches for nurturing tumor cells that arrive at the secondary site, bone. In particular, we have shown that the unfolding of Fn molecules is correlated with upregulated proangiogenic and proinflammatory secretion by breast cancer cells, which can subsequently promote the formation of new blood vessels and induce altered pre-osteoblast activities. Together, these altered breast cancer and osteoblast cell functions mediate pathologic bone remodeling that could in turn result in further modifications of the mineral materials properties.

## **1.2 Experimental design**

### 1.2.1 Source of hydroxyapatite

Hydroxyapatite (HAP) is closely related to the mineral component of bone and teeth in both structural and mechanical properties [15]. It is also a naturally occurring geologic mineral that is ubiquitous in various rocks because of its wide stability in geological processes. The bone and teeth apatite have different properties from the geologic apatite because they are formed in different ways. For example, nano-sized bone apatite has higher solubility and lower crystallinity than macroscale geologic apatite. Both of them have substitution ions in the crystal lattice, although the species and concentration of these ions are different. Synthetic stoichiometric HAP nanoparticles resemble bone mineral in size, shape, and crystallinity, but lack substitution ions. Additionally, nanoparticles can be cytotoxic to cells due to potential cellular uptake, unless they are embedded in polymer scaffolds. Macroscale geologic apatite crystals not only helped solving this problem but also allowed us to control independently different materials properties. The

geologic apatite crystals used had similar substitution ions as bone apatite, although with much higher crystallinity. The preparation and characterization of synthetic HAP nanoparticles and geologic HAP facets will be discussed in Chapter 2 and Chapter 3, respectively.

### 1.2.2 Source of fibronectin

*In vivo*, fibronectin (Fn) is present in soluble molecular form in body fluids (300 µg/mL in plasma, less in other fluids) and in insoluble fibrillar form in tissue ECMs. There are two types of Fn, namely plasma Fn and cellular Fn. They are synthesized by different types of cells but are very similar in structure and properties. Cellular Fn contains variable amounts of either or both ED-A and ED-B alternative splicing regions that are absent in plasma Fn [50]. One major source of plasma Fn is hepatocytes in the liver, while fibroblasts and endothelial cells are major producers of cellular Fn [51]. Human plasma Fn used in this study was obtained from Invitrogen (Thermo Fisher Scientific), and reconstituted with DI water to 1 mg/mL stock solution stored at -80 °C. The stock solution was diluted with 1x phosphate buffered saline (PBS) to desired concentrations before use. Fn solutions were used either to coat HAP surfaces for studying single molecule conformation (described in Chapter 2 and Chapter 3), or to manually pull Fn fibers for studying fiber level conformational and mechanical properties (described in Appendix A).

### 1.2.3 Source of cells

Two types of cells were used for this thesis: MDA-MB-231 (ATCC® HTB26™) human breast cancer cells, and MC3T3-E1 subclone 4 (ATCC® CRL2593™) mouse pre-osteoblast cells.

Breast cancer is heterogeneous, and could be classified into at least five subtypes: luminal A, luminal B, HER2, basal, and claudin-low, based on gene expression profiling and the immunohistochemical expression of oestrogen receptor (ER $\alpha$ ), progesterone receptor (PR) and human epidermal growth factor receptor 2 (HER2) [52][53]. A number of breast cancer cell lines have been developed for *in vivo* and *in vitro* studies to understand breast carcinomas. The most widely used cell lines include MCF-7, T-47D, and MDA-MB-231 [54]. MDA-MB-231 cell line belongs to the claudin-low subtype, which lacks expression of ER $\alpha$ , PR, and HER2, and is associated with poor prognosis. They are highly invasive *in vitro* and relatively poorly invasive *in vivo*, and therefore often used as *in vitro* models for studying breast cancer metastasis. The population of this cell line is heterogeneous and distinct sub-populations can be obtained based on preferential metastatic site (bone or brain) [55].

The MC3T3-E1 subclone 4 cell line is isolated from the cloned phenotypically heterogeneous MC3T3-E1 cell line (from mouse calvaria). Low subclone cell lines (e.g., subclone 4 and 14) exhibit high levels of osteoblast differentiation and form a well mineralized ECM after 10 days, while high subclone cell lines (e.g., subclone 24 and 30) exhibit low level of osteoblast differentiation and do not form ECM [56]. Thus the MC3T3-E1 subclone 4 cell line is a good model for studying *in vitro* osteoblast differentiation, particularly ECM signaling. Their behaviors are similar to primary calvarial osteoblasts.

It needs to be noted that these cell lines may not fully reflect the *in vivo* response due to genetic modifications as compared with primary cells that are harvested directly from the tissue of interest.

#### 1.2.4 Requirements for cell culture platform

Standard cell culture conditions were used for cell behavior studies in this thesis. Basic environmental considerations for culturing cells include temperature, humidity, appropriate growth medium, pH, and osmolality. Typical culture medium contains amino acids, vitamins, inorganic salts, glucose, and serum as a source of growth factors, hormones, and attachment factors for cells, and should be optimized based on cell type [57]. In this thesis, cells were maintained at 37 °C and 5% CO<sub>2</sub> in  $\alpha$ MEM (Sigma Aldrich) supplemented with 10% fetal bovine serum (FBS, Atlanta Biologicals) and 1% penicillin/streptomycin (P/S, Quality Biological).  $\alpha$ MEM is the  $\alpha$  modification of Minimum Essential Medium (MEM), which contains amino acids, salts, vitamins and so on. FBS contains many growth factors that support embryonic growth, bovine serum albumin, glucose, as well as other defined and undefined components. The addition of P/S prevents bacterial contamination of cell cultures. The cell culture platforms developed in this thesis were all tested for good cell viability before cell function studies described in Chapter 4 and Chapter 5.

### **1.3 Thesis overview**

The scope of this thesis was to develop cell culture platforms to investigate the role of HAP/Fn molecular interactions in mediating cellular behaviors during cancer bone metastasis. In order to control HAP materials properties, two strategies were used. The first strategy utilized synthetic HAP nanoparticles, and the second strategy utilized geologic apatite single crystals. FRET spectroscopy was used to probe differential Fn conformation and deposition as a function of HAP materials properties. Fn coated HAP facets generated using the second strategy were

then used for studying altered cellular behaviors to establish a correlation with differential Fn conformation and deposition mediated by HAP surface properties.

In Chapter 2, the synthesis and characterization of a library of HAP nanoparticles are described. Using a two-step hydrothermal synthesis method, HAP nanoparticles with controlled size, shape, and crystallinity were obtained. FRET spectroscopy was used to quantify the deposition and conformation of Fn adsorbed onto HAP nanoparticles with various materials properties. Both single nanoparticles surface charge and particle agglomerates size and morphology were found to trigger differential Fn adsorption at the HAP surface.

In Chapter 3, geologic HAP single crystals were cut along two specific crystallographic orientations and polished to two desired roughness levels to generate HAP facets with controlled surface chemistry and topography/roughness. This strategy allowed us to deconvolute the effects of surface chemistry and topography on Fn adsorption, and to avoid cytotoxicity due to eventual uptake of nanoparticles by cells. Fn deposition and conformation were analyzed via FRET, and the individual effects of surface chemistry and topography are discussed.

In Chapter 4, using the Fn coated geologic HAP facets characterized in Chapter 3 as cell culture platforms, MDA-MB-231 breast cancer cells were introduced to evaluate cell viability and adhesion, FA assembly, and proangiogenic secretion of VEGF and IL-8. HAP surface chemistry and topography had both individual and combined effects on Fn-mediated breast cancer cell functions, in particular FA assembly and proangiogenic secretion.

In Chapter 5, MC3T3-E1 pre-osteoblasts were seeded onto Fn coated geologic HAP facets to investigate early osteoblast adhesion and FA assembly. FA assembly, in particular FA size, was found to depend on both HAP surface chemistry and topography.

In Appendix A, fabrication of artificial Fn fibers and Fn-HAP nanocomposite fibers is described. HAP nanoparticles developed in Chapter 2 were either used to decorate the surface of Fn fibers or incorporated inside Fn fibers to form Fn-HAP composite fibers. Preliminary results for altered conformational and mechanical properties of Fn fibers in presence of HAP nanoparticles are discussed to provide implications for altered structural and mechanical properties of inflamed tissues.

In Appendix B, FRET was used to measure Fn conformation adsorbed on mica as a function of surface curvature. Atomically smooth mica was glued on silica discs with various radii of curvature that were used for surface forces apparatus studies. Our results indicate that, at fixed concentration and nanoscale roughness, Fn conformation depends on the macroscopic curvature of the underlying surface.

In Appendix C, the sequestration of VEGF within Fn fibers in cell deposited matrices was measured using a ratiometric method to investigate how Fn conformational changes affect VEGF binding. Our results indicate that Fn conformation in the ECM plays critical roles in mediating both the direct sequestration of growth factors by the ECM and the indirect (integrin-mediated) secretion of cells in contact with the ECM.

## **1.4 Conclusions**

This thesis focuses on developing cell culture platforms containing HAP and Fn to elucidate the role of inorganic/organic interface in cancer bone metastasis and HAP-related inflammation. A combination of materials science and biochemical approaches was utilized to (i) quantify the effects of HAP materials properties on the deposition and conformation of Fn molecules; (ii)

determine the downstream behavior of breast cancer cells and osteoblast cells; (iii) measure altered conformational and mechanical properties of Fn fibers in presence of HAP. Overall, insights gained by these structural and mechanical studies not only increase our understanding of breast cancer bone metastasis and other HAP-related inflammation, but also have important implications for the design of safe biomaterials platforms for tissue regeneration applications.

## REFERENCES

- [1] N. Sathiakumar, E. Delzell, M.A. Morrissey, C. Falkson, M. Yong, V. Chia, et al., Mortality following bone metastasis and skeletal-related events among women with breast cancer: a population-based analysis of U.S. Medicare beneficiaries, 1999-2006., *Breast Cancer Res. Treat.* 131 (2012) 231–8. doi:10.1007/s10549-011-1721-x.
- [2] M. Harries, A. Taylor, L. Holmberg, O. Agbaje, H. Garmo, S. Kabilan, et al., Incidence of bone metastases and survival after a diagnosis of bone metastases in breast cancer patients, *Cancer Epidemiol.* 38 (2014) 427–434. doi:10.1016/j.canep.2014.05.005.
- [3] S. Weiner, H.D. Wagner, *The Material Bone: Structure-Mechanical Function Relations*, *Annu. Rev. Mater. Sci.* 28 (1998) 271–298. doi:10.1146/annurev.matsci.28.1.271.
- [4] M.D. McKee, W.N. Addison, M.T. Kaartinen, Hierarchies of extracellular matrix and mineral organization in bone of the craniofacial complex and skeleton., *Cells. Tissues. Organs.* 181 (2005) 176–88. doi:10.1159/000091379.
- [5] M. Kinder, E. Chislock, K.M. Bussard, L. Shuman, A.M. Mastro, Metastatic breast cancer induces an osteoblast inflammatory response, *Exp. Cell Res.* 314 (2008) 173–183. doi:10.1016/j.yexcr.2007.09.021.
- [6] K.M. Bussard, D.J. Venzon, A.M. Mastro, Osteoblasts are a major source of inflammatory cytokines in the tumor microenvironment of bone metastatic breast cancer, *J. Cell. Biochem.* 111 (2010) 1138–1148. doi:10.1002/jcb.22799.
- [7] M.S. Bendre, D.C. Montague, T. Peery, N.S. Akel, D. Gaddy, L.J. Suva, Interleukin-8 stimulation of osteoclastogenesis and bone resorption is a mechanism for the increased osteolysis of metastatic bone disease, *Bone.* 33 (2003) 28–37. doi:10.1016/S8756-3282(03)00086-3.
- [8] R.R. Mercer, A.M. Mastro, Cytokines secreted by bone-metastatic breast cancer cells alter the expression pattern of f-actin and reduce focal adhesion plaques in osteoblasts through PI3K, *Exp. Cell Res.* 310 (2005) 270–281. doi:10.1016/j.yexcr.2005.07.029.
- [9] T.A. Guise, W.M. Kozlow, A. Heras-Herzig, S.S. Padalecki, J.J. Yin, J.M. Chirgwin, Molecular mechanisms of breast cancer metastases to bone., *Clin. Breast Cancer.* 5 Suppl (2005) S46–53. doi:10.3816/CBC.2005.s.004.

- [10] S.P. Pathi, C. Kowalczewski, R. Tadipatri, C. Fischbach, A novel 3-D mineralized tumor model to study breast cancer bone metastasis., *PLoS One*. 5 (2010) e8849. doi:10.1371/journal.pone.0008849.
- [11] S.P. Pathi, D.D.W. Lin, J.R. Dorvee, L.A. Estroff, C. Fischbach, Hydroxyapatite nanoparticle-containing scaffolds for the study of breast cancer bone metastasis., *Biomaterials*. 32 (2011) 5112–22. doi:10.1016/j.biomaterials.2011.03.055.
- [12] R.G. Hanschin, W.B. Stern, X-ray diffraction studies on the lattice perfection of human bone apatite (Crista iliaca)., *Bone*. 16 (1995) 355S–363S. <http://www.ncbi.nlm.nih.gov/pubmed/7626325>.
- [13] A. Boskey, Bone mineral crystal size., *Osteoporos. Int*. 14 (2003) S16–20. doi:10.1007/s00198-003-1468-2.
- [14] J.S. Yerramshetty, C. Lind, O. Akkus, The compositional and physicochemical homogeneity of male femoral cortex increases after the sixth decade., *Bone*. 39 (2006) 1236–43. doi:10.1016/j.bone.2006.06.002.
- [15] A.L. Boskey, Mineralization of bones and teeth, *Elements*. 3 (2007) 385–391. doi:10.2113/GSELEMENTS.3.6.385.
- [16] S. Choi, S. Coonrod, L. Estroff, C. Fischbach, Chemical and physical properties of carbonated hydroxyapatite affect breast cancer cell behavior, *Acta Biomater*. 24 (2015) 333–342. doi:10.1016/j.actbio.2015.06.001.
- [17] M.J. Bradshaw, M.L. Smith, Multiscale relationships between fibronectin structure and functional properties., *Acta Biomater*. 10 (2014) 1524–31. doi:10.1016/j.actbio.2013.08.027.
- [18] R.E. Weiss, A.H. Reddi, Appearance of fibronectin during the differentiation of cartilage, bone, and bone marrow., *J. Cell Biol*. 88 (1981) 630–6. doi:10.1083/jcb.88.3.630.
- [19] E.A. Cowles, M.E. DeRome, G. Pastizzo, L.L. Brailey, G.A. Gronowicz, Mineralization and the expression of matrix proteins during in vivo bone development, *Calcif Tissue Int*. 62 (1998) 74–82.
- [20] P. Singh, C. Carraher, J.E. Schwarzbauer, Assembly of fibronectin extracellular matrix, *Annu. Rev. Cell Dev. Biol*. 26 (2010) 397–419. doi:10.1146/annurev-cellbio-100109-

104020.

- [21] S.L. Dallas, Q. Chen, P. Sivakumar, Dynamics of assembly and reorganization of extracellular matrix proteins., *Curr. Top. Dev. Biol.* 75 (2006) 1–24. doi:10.1016/S0070-2153(06)75001-3.
- [22] J. Sottile, D.C. Hocking, Fibronectin polymerization regulates the composition and stability of extracellular matrix fibrils and cell-matrix adhesions, *Mol. Biol. Cell.* 13 (2002) 3546–3559. doi:10.1091/mbc.E02-01-0048.
- [23] P.G. Grzesik, Wojciech J, Robey, Bone Matrix RGD Glycoproteins: Immunolocalization Bone Cells In Vitro, *J. Bone Miner. Res.* 9 (1994) 487–496.
- [24] A. Bentmann, N. Kawelke, D. Moss, H. Zentgraf, Y. Bala, I. Berger, et al., Circulating fibronectin affects bone matrix, whereas osteoblast fibronectin modulates osteoblast function., *J. Bone Miner. Res.* 25 (2010) 706–715. doi:10.1359/jbmr.091011.
- [25] K.C. Clause, T.H. Barker, Extracellular matrix signaling in morphogenesis and repair., *Curr. Opin. Biotechnol.* 24 (2013) 830–3. doi:10.1016/j.copbio.2013.04.011.
- [26] S. Johansson, G. Svineng, K. Wennerberg, L. Lohikangas, Fibronectin-integrin interactions, *Front. Biosci.* 2 (1997) 126–146.
- [27] A. Krammer, D. Craig, W.E. Thomas, K. Schulten, V. Vogel, A structural model for force regulated integrin binding to fibronectin's RGD-synergy site, *Matrix Biol.* 21 (2002) 139–147. doi:10.1016/S0945-053X(01)00197-4.
- [28] T.A. Petrie, J.R. Capadona, C.D. Reyes, A.J. García, Integrin specificity and enhanced cellular activities associated with surfaces presenting a recombinant fibronectin fragment compared to RGD supports, *Biomaterials.* 27 (2006) 5459–5470. doi:10.1016/j.biomaterials.2006.06.027.
- [29] M.L. Smith, D. Gourdon, W.C. Little, K.E. Kubow, R.A. Eguiluz, S. Luna-Morris, et al., Force-induced unfolding of fibronectin in the extracellular matrix of living cells., *PLoS Biol.* 5 (2007) e268. doi:10.1371/journal.pbio.0050268.
- [30] A.M.D. Wan, E.M. Chandler, M. Madhavan, D.W. Infanger, C.K. Ober, D. Gourdon, et al., Fibronectin conformation regulates the proangiogenic capability of tumor-associated adipogenic stromal cells., *Biochim. Biophys. Acta.* 1830 (2013) 4314–20.

doi:10.1016/j.bbagen.2013.03.033.

- [31] S.K. Akiyama, K. Olden, K.M. Yamada, Fibronectin and integrins in invasion and metastasis., *Cancer Metastasis Rev.* 14 (1995) 173–89.  
<http://www.ncbi.nlm.nih.gov/pubmed/8548867>.
- [32] A.M. Moursi, R.K. Globus, C.H. Damsky, Interactions between integrin receptors and fibronectin are required for calvarial osteoblast differentiation in vitro., *J. Cell Sci.* 110 ( Pt 1 (1997) 2187–2196.
- [33] R.K. Globus, S.B. Doty, J.C. Lull, E. Holmuhamedov, M.J. Humphries, C.H. Damsky, Fibronectin is a survival factor for differentiated osteoblasts., *J. Cell Sci.* 111 (1998) 1385–1393.
- [34] K. Wang, B.R. Seo, C. Fischbach, D. Gourdon, Fibronectin Mechanobiology Regulates Tumorigenesis, *Cell. Mol. Bioeng.* (2015). doi:10.1007/s12195-015-0417-4.
- [35] A. von Au, M. Vasel, S. Kraft, C. Sens, N. Hackl, A. Marx, et al., Circulating Fibronectin Controls Tumor Growth, *Neoplasia.* 15 (2013) 925–IN24. doi:10.1593/neo.13762.
- [36] G. Maity, P.R. Choudhury, T. Sen, K.K. Ganguly, H. Sil, A. Chatterjee, Culture of human breast cancer cell line (MDA-MB-231) on fibronectin-coated surface induces pro-matrix metalloproteinase-9 expression and activity, *Tumor Biol.* 32 (2011) 129–138.  
doi:10.1007/s13277-010-0106-9.
- [37] F. Aoudjit, K. Vuori, Integrin signaling inhibits paclitaxel-induced apoptosis in breast cancer cells., *Oncogene.* 20 (2001) 4995–5004. doi:10.1038/sj.onc.1204554.
- [38] R. Korah, M. Boots, R. Wieder, Integrin alpha5beta1 promotes survival of growth-arrested breast cancer cells: an in vitro paradigm for breast cancer dormancy in bone marrow., *Cancer Res.* 64 (2004) 4514–4522. doi:10.1158/0008-5472.CAN-03-3853.
- [39] F.G. Giancotti, E. Ruoslahti, Integrin Signaling, *Science* (80-. ). 285 (1999) 1028–1032.  
doi:10.1126/science.285.5430.1028.
- [40] R. Rathinam, S.K. Alahari, Important role of integrins in the cancer biology, *Cancer Metastasis Rev.* 29 (2010) 223–237. doi:10.1007/s10555-010-9211-x.

- [41] P. Costa, T.M.E. Scales, J. Ivaska, M. Parsons, Integrin-Specific Control of Focal Adhesion Kinase and RhoA Regulates Membrane Protrusion and Invasion, *PLoS One*. 8 (2013). doi:10.1371/journal.pone.0074659.
- [42] G. Neufeld, T. Cohen, S. Gengrinovitch, Z. Poltorak, Vascular endothelial growth factor (VEGF) and its receptors., *FASEB J*. 13 (1999) 9–22. doi:Doi 10.1210/Er.2003-0027.
- [43] D. Hanahan, R.A. Weinberg, The hallmarks of cancer, *Cell*. 100 (2000) 57–70. doi:10.1007/s00262-010-0968-0.
- [44] S. De, O. Razorenova, N.P. McCabe, T. O’Toole, J. Qin, T. V Byzova, VEGF-integrin interplay controls tumor growth and vascularization., *Proc. Natl. Acad. Sci. U. S. A*. 102 (2005) 7589–7594. doi:10.1073/pnas.0502935102.
- [45] K. Wang, R.C. Andresen Eguiluz, F. Wu, B.R. Seo, C. Fischbach, D. Gourdon, Stiffening and unfolding of early deposited-fibronectin increase proangiogenic factor secretion by breast cancer-associated stromal cells, *Biomaterials*. 54 (2015) 63–71. doi:10.1016/j.biomaterials.2015.03.019.
- [46] C. Fischbach, H.J. Kong, S.X. Hsiong, M.B. Evangelista, W. Yuen, D.J. Mooney, Cancer cell angiogenic capability is regulated by 3D culture and integrin engagement., *Proc. Natl. Acad. Sci. U. S. A*. 106 (2009) 399–404. doi:10.1073/pnas.0808932106.
- [47] Y. Lin, R. Huang, L. Chen, S. Li, Q. Shi, C. Jordan, et al., Identification of interleukin-8 as estrogen receptor-regulated factor involved in breast cancer invasion and angiogenesis by protein arrays, *Int. J. Cancer*. 109 (2004) 507–515. doi:10.1002/ijc.11724.
- [48] K. Xie, Interleukin-8 and human cancer biology., *Cytokine Growth Factor Rev*. 12 (2001) 375–391. doi:10.1016/S1359-6101(01)00016-8.
- [49] J.E. De Larco, B.R. Wuertz, K.A. Rosner, S.A. Erickson, D.E. Gamache, J.C. Manivel, et al., A potential role for interleukin-8 in the metastatic phenotype of breast carcinoma cells., *Am. J. Pathol*. 158 (2001) 639–646. doi:10.1016/S0002-9440(10)64005-9.
- [50] M.K. Magnusson, D.F. Mosher, Fibronectin : Structure, Assembly, and Cardiovascular Implications, *Arterioscler. Thromb. Vasc. Biol*. 18 (1998) 1363–1370. doi:10.1161/01.ATV.18.9.1363.
- [51] R.O. Hynes, K.M. Yamada, Fibronectins: multifunctional modular glycoproteins., *J. Cell*

Biol. 95 (1982) 369–77.

<http://www.pubmedcentral.nih.gov/articlerender.fcgi?artid=2112946&tool=pmcentrez&rendertype=abstract>.

- [52] A. Prat, J.S. Parker, O. Karginova, C. Fan, C. Livasy, J.I. Herschkowitz, et al., Phenotypic and molecular characterization of the claudin-low intrinsic subtype of breast cancer., *Breast Cancer Res.* 12 (2010) R68. doi:10.1186/bcr2635.
- [53] R.M. Neve, K. Chin, J. Fridlyand, J. Yeh, F.L. Baehner, T. Fevr, et al., A collection of breast cancer cell lines for the study of functionally distinct cancer subtypes, *Cancer Cell.* 10 (2006) 515–527. doi:10.1016/j.ccr.2006.10.008.
- [54] M. Lacroix, G. Leclercq, Relevance of breast cancer cell lines as models for breast tumours: An update, *Breast Cancer Res. Treat.* 83 (2004) 249–289. doi:10.1023/B:BREA.0000014042.54925.cc.
- [55] T. Yoneda, P.J. Williams, T. Hiraga, M. Niewolna, R. Nishimura, A bone-seeking clone exhibits different biological properties from the MDA-MB-231 parental human breast cancer cells and a brain-seeking clone in vivo and in vitro., *J. Bone Miner. Res.* 16 (2001) 1486–1495. doi:10.1359/jbmr.2001.16.8.1486.
- [56] D. Wang, K. Christensen, K. Chawla, G. Xiao, P.H. Krebsbach, R.T. Franceschi, Isolation and characterization of MC3T3-E1 preosteoblast subclones with distinct in vitro and in vivo differentiation/mineralization potential., *J. Bone Miner. Res.* 14 (1999) 893–903. doi:10.1359/jbmr.1999.14.6.893.
- [57] M. Arora, *Cell Culture Media : A Review*, *Mater. Methods.* 3 (2013) 1–27. doi:10.13070/mm.en.3.175.

## **Chapter 2.**

# **Differential Fibronectin Adsorption on Synthetic Hydroxyapatite Nanoparticles: Effect of Size, Shape, and Crystallinity**

Contributors: Debra Lin, Jin Ho Chang, Lara Estroff, and Delphine Gourdon.

### **2.1 Abstract**

Hydroxyapatite (HAP,  $\text{Ca}_{10}(\text{PO}_4)_6(\text{OH})_2$ ) nanoparticles with controlled materials properties have been synthesized through a two-step hydrothermal aging method to investigate fibronectin (Fn) adsorption. Two distinct populations of HAP nanoparticles have been generated: HAP1 particles had smaller size, plate-like shape, lower crystallinity and more negative zeta potential than HAP2 particles. We then developed 2-dimensional (2D) platforms containing HAP and Fn and analyzed both the amount and the conformation of Fn via Förster resonance energy transfer (FRET) at various HAP concentrations. Our FRET analysis reveals that larger amounts of more compact Fn molecules were adsorbed onto HAP1 than onto HAP2 particles. Additionally, our data show that the amount of compact Fn adsorbed increased with increasing HAP concentration due to the formation of nanoparticle agglomerates. We propose that both the surface chemistry of single nanoparticles and the size and morphology of HAP agglomerates play significant roles in the interaction of Fn with HAP. Collectively our findings suggest that the HAP-induced conformational changes of Fn, a critical mechanotransducer protein involved in the communication of cells with their environment, will ultimately affect downstream cellular behaviors. These results have important implications for our understanding of organic-inorganic

interactions in physiological and pathological biomineralization processes, such as HAP-related inflammation.

## 2.2 Introduction

The adsorption of proteins onto surfaces is a common but complicated phenomenon in numerous biological processes and has promoted great research interest in various fields. For example, proteins adsorbed onto biomedical implants can trigger the complement cascade and cause inflammation [1]. In the biomineralization community, it is widely acknowledged that protein-crystal interactions also play important roles in controlling crystal nucleation and growth [2–4]. One biocompatible and bioactive material often used as implant coating for bone regeneration is hydroxyapatite (HAP,  $\text{Ca}_{10}(\text{PO}_4)_6(\text{OH})_2$ ), which is closely related to bone apatite. Bone apatite, as compared with geologic HAP, has lower crystallinity and carbonate ions substituting for some fraction of hydroxyl and phosphate ions. Furthermore, the size, crystallinity, and compositional heterogeneity of bone apatite change as a function of age and disease progression [5–7]. In this study, we focus on the interaction between HAP and fibronectin (Fn), a 440 kDa multimodular glycoprotein present both in soluble form (as single molecules) in the blood and in polymerized insoluble form (as macromolecular fibers) in the extracellular matrix (ECM) [8]. The HAP-Fn interface has received increasing attention due to the ubiquitous role of mineral-protein interactions both in the design of biomedical implants and in the understanding of physiological/pathological processes such as wound healing/calcification. However, the molecular mechanisms of interactions between HAP and Fn remain unclear; in particular, the effect of materials properties of HAP on the quantity and conformation of

adsorbed Fn is still not fully understood due to the intrinsic structural and chemical complexities of Fn.

The conformation and quantity of proteins adsorbed onto a surface depend on numerous factors, which include: surface chemistry, roughness and local geometric characteristics such as curvature [9,10]. Specifically, electrostatic forces play an important role in governing interactions between proteins and biominerals [11]. For example, experiments have shown that Fn adsorbs preferentially onto purely ionic crystal faces of calcite with no surface bound water molecules [12]. A previous study using Förster resonance energy transfer (FRET) and Atomic force microscopy (AFM) further demonstrates that local changes in the electrostatic environment during the growth of calcium oxalate monohydrate can induce major alterations in Fn conformation [13]. Surface charge has been shown to regulate Fn conformation and integrin binding using model self-assembled monolayer substrates, where Fn molecules adsorbed onto negatively charged surfaces functionalized with carboxyl groups interact more strongly with  $\alpha_5\beta_1$  integrins and induce efficient cellular adhesion as compared with Fn adsorbed onto neutral surfaces [14].

With the rapid growth of nanotechnology over the years, engineered nanomaterials have been increasingly suggested for biomedical applications such as drug delivery and disease diagnosis. Thus, understanding interactions at the nanomaterial-biological interface becomes very important in designing safe biomaterials [15]. Previous experimental work has shown that nanoroughness of substrates enhances protein adsorption and induces conformational changes of proteins, such as Fn [14,16]. Additionally, local surface geometry of nanomaterials, such as curvature of nanoparticles and nanopores, can also significantly affect protein conformation, especially when the characteristic sizes of the nanomaterial and the protein are comparable [17,18]. Therefore,

both surface chemistry and morphology need to be carefully investigated when studying protein adsorption on nanomaterials.

Although a lot of effort has been devoted to studying HAP interactions with mineral-modulating proteins [3], there is still limited work on HAP-Fn interactions. Previous computational studies suggest that the adsorption of Fn-type III modules (either the single Fn-III<sub>10</sub> module or the Fn-III<sub>7-10</sub> sequence) onto crystal faces of HAP is governed by electrostatic interactions and hydrogen bonds forming between the guanidine groups of arginine residues on Fn modules and the phosphate groups on HAP surface [19–21]. Experimental studies have demonstrated that Fn molecules adsorbed onto smooth HAP surfaces show higher availability of the cell binding domain (Fn-III<sub>9-10</sub>) and that cell spreading is enhanced as compared with Fn adsorbed onto smooth Au surfaces [22], possibly contributing to the biocompatibility of HAP implants [23,24]. AFM force spectroscopy has revealed that Fn molecules adsorbed onto HAP surfaces require higher total unfolding force than Fn adsorbed onto atomically smooth mica surfaces, indicating that Fn may have stronger interactions with HAP than with mica [25]. Additionally, UV/Vis spectrometry has shown that the crystallite size and specific surface area of HAP nanoparticles, together with protein bulk concentration, all affect the amount of Fn adsorbed [26]. However, the average conformation of Fn adsorbed onto HAP requires further investigation.

The HAP-Fn interface has important physiological and pathological relevance, as it resembles the apatite-ECM interface in bone microenvironments and the microcalcification-ECM interface in inflamed tissues including blood vessels and primary mammary tumors. The ECM is a fibrillar network composed mainly of collagen and Fn fibers and plays a vital role in regulating cellular responses to chemical and mechanical signals from the microenvironment

[27]. We are particularly interested in Fn, as it is the first protein deposited by cells in the ECM and as it regulates the deposition of other ECM components, such as collagen type I [28,29]. Furthermore, Fn is dramatically upregulated during inflammation [30]. As a critical mechanotransducer, the force-induced conformational changes of Fn can regulate the type of binding sites that are exposed or disrupted, in particular the integrin binding sites located on Fn-III<sub>9,10</sub> used for cell attachment. More importantly, these conformational-dependent binding events ultimately influence downstream cellular behaviors to regulate or dysregulate homeostasis *in vivo* [31–33].

In this study, we have synthesized two distinct populations of HAP nanoparticles, HAP1 and HAP2, with controlled size, shape and crystallinity. HAP1 is more physiologically-relevant than HAP2, as it more closely resembles bone apatite in terms of size, shape, and crystallinity [5]. It is worth to note that bone-derived HAP particles have been reported to show negative zeta potential, which promotes attachment and proliferation of bone cells [34]. By combining Fn and HAP nanoparticles at various HAP concentrations, we have investigated how the materials properties of HAP nanoparticles affect the amount and conformation of adsorbed Fn using FRET spectroscopy [31,35]. Our results demonstrate that both the amount and the conformation of Fn are affected by (i) the size, crystallinity, and shape of single HAP nanoparticles, as well as by (ii) the size and morphology of nanoparticle agglomerates.

## **2.3 Materials and Methods**

### **2.3.1 Hydroxyapatite nanoparticle synthesis**

HAP nanoparticles with controlled size, crystallinity, and shape were synthesized through a typical wet precipitation reaction of a calcium salt with a phosphate salt followed by hydrothermal treatment for 0 or 6 days [36]. All chemicals for these reactions were obtained from Sigma Aldrich and used as received. A solution of  $(\text{NH}_4)_2\text{HPO}_4$  (300 mL, 10 mM) was added drop-wise into a solution of  $\text{Ca}(\text{NO}_3)_2$  (500 mL, 10 mM) under rapid stirring at 4 °C in an ice-water bath for a final calcium to phosphate ratio of 1.67. The pH of the starting solution was adjusted to pH 10 with 0.1 M  $\text{NH}_4\text{OH}$ . The reaction was allowed to proceed for 1 hr at 4 °C, and then stirred at 20 °C for 3 days. After 3 days, the resulting opaque suspension was divided into 720 mL for concentration and 80 mL for further reaction. The 720 mL opaque suspension was allowed to settle until separation of white sediment from clear supernatant; after decanting the clear supernatant, the concentrated suspension (100 mL) was used to obtain HAP1 nanoparticles. The remaining 80 mL of the original opaque suspension was placed in a pressure vessel (Parr Instrument Company 4748) and heated at 180 °C in an oven for 6 days to obtain HAP2 nanoparticles. The nanoparticle suspensions were then transferred into a Regenerated Cellulose tubular membrane (Cellu-Sep T1 5030-46, Nominal MWCO 3500) and dialyzed against 1x phosphate buffered saline (PBS) at pH 7.4 for 5 days. After dialysis, the nanoparticle suspensions were further concentrated by decanting the clear supernatant as described previously and stored in glass vials as stock solutions. To determine the concentration of nanoparticles in PBS, a known volume of the stock solution was concentrated by centrifugation (Thermo Scientific Sorvall Legend RT + Centrifuge, 3600 g, 7 min), washed with 0.15 M  $\text{NH}_4\text{OH}$  twice, rinsed with acetone and dried at 20° C. The dried nanoparticles were then weighed to obtain concentration of the stock solution and used for characterization.

### 2.3.2 Hydroxyapatite nanoparticles characterization

Powder X-ray diffraction (pXRD) was used to determine particle phase. Fourier Transform Infrared Spectroscopy (FTIR) was used to assess the crystallinity of the nanoparticles. The size and shape distributions of the nanoparticles were determined by Transmission Electron Microscopy (TEM). Zeta potential of the nanoparticles was measured using Laser Doppler Electrophoresis (LDE). Dried nanoparticles were examined by pXRD (Scintag Inc. PAD-X theta-theta X-ray Diffractometer,  $\text{CuK}\alpha$  1.54 Å, accelerating voltage 40 kV, current 40 mA, continuous scan, 1.0 deg/min). Scherrer analysis was used to determine crystalline domain sizes from the peak broadening of the {002} peak of HAP ( $25.88^\circ$ ) using an  $\text{Al}_2\text{O}_3$  standard to correct for instrumental broadening (Software: JADE 9, Materials Data, Inc.). For FTIR (Mattson Instruments 2020 Galaxy Series FT-IR), dried particles were used to prepare KBr pellets and to acquire spectra (res  $4.0\text{ cm}^{-1}$ , 256 scans). Particle crystallinities were determined from the splitting factor obtained via normalizing the sum of the absorbance at  $565\text{ cm}^{-1}$  and  $603\text{ cm}^{-1}$  to the minimum between the doublet following Weiner and Bar-Yosef [37]. For TEM, a stock solution of dialyzed particles in PBS was diluted with PBS and dropped onto a carbon-coated copper TEM grid (Electron Microscopy Sciences). After 10 min, PBS was wicked away with filter paper and the sample was left to dry for another 10 min. Bright field TEM (FEI Tecnai T-12 Spirit, 120 kV) images were analyzed through ImageJ (NIH) to determine the size and shape of particles. For zeta potential measurements, HAP stock solutions were diluted to various concentrations in PBS and measured in folded capillary cells using Zetasizer Nano-ZS (Malvern Instruments Ltd. ZEN3600), with 3 to 6 measurements and a total of 20 to 30 runs per sample.

### 2.3.3 Fibronectin and FRET labeling

Fibronectin (Fn) was obtained from Life Technologies, NY. AlexaFluor 488 succinimide ester and AlexaFluor 546 maleimide (Invitrogen, CA) were used to label Fn for intramolecular

FRET as previously described by Baneyx et al [35] and Smith et al [31]. Labeling ratios and Fn concentrations were determined using a DU®730 UV/Vis spectrophotometer (Beckman, IN) at 280 nm, 495 nm, and 556 nm. Calibration of FRET labeled Fn in solutions was carried out in guanidine hydrochloride (GdnHCl) at concentrations of 0, 2 M and 4 M to obtain FRET ratios, defined as acceptor/donor intensity ratios ( $I_A/I_D$ ), as a function of protein denaturation.

#### 2.3.4 Fabrication of 2D platforms

2D platforms were fabricated using 8-well Lab-Tek chambers with borosilicate coverglass bottom (Thermo Fisher Scientific Inc.). Dialyzed nanoparticles in PBS were used to dilute stock solutions of Fn to 50 µg/mL. The diluted Fn solution contained 10% FRET labeled Fn and 90% unlabeled Fn to avoid intermolecular FRET, so that only intramolecular FRET was measured to assess conformation of single Fn molecules [31]. After mixing, the concentrations of the nanoparticles were 0.01 mg/mL, 0.05 mg/mL, and 0.1 mg/mL, while the concentration of Fn was kept to 50 µg/mL for all conditions. 130 µL of the mixture was added to each well and incubated at 4 °C for 24 hrs before imaging.

#### 2.3.5 FRET data acquisition

2D platforms containing HAP and Fn were imaged with a Zeiss 710 confocal microscope (Zeiss, Munich, Germany). 16-bit z-stack images were acquired using the C-Apochromat water-immersion 40x/1.2 objective, a pinhole of 1 AU, 488 nm laser with 30% laser power, pixel dwell time of 6.3 µs, PMT1 and PMT2 gains of 600 V, and z step size of 0.5 µm. FRET labeled Fn molecules were excited with a 488 nm laser line; emissions from donor and acceptor fluorophores were simultaneously collected in the PMT1 channel (514-526 nm) and the PMT2 channel (566-578 nm), respectively. Meanwhile transmitted light images were acquired in the T-

PMT channel (transmitted light detector). These z-stack images were analyzed with a customized Matlab code to generate FRET ratio ( $I_A/I_D$ ) images and histograms, as well as mean FRET ratios for all z-slices in a z-stack.

### 2.3.6 Statistical analysis

One-way ANOVA with Tukey's post test and Student's t-test were used to determine statistical significance between conditions in GraphPad Prism (GraphPad Software, Inc., CA). In all cases,  $p < 0.05$  is indicated by a single star,  $p < 0.01$  by two stars and  $p < 0.001$  by three stars.

## 2.4 Results

### 2.4.1 Hydroxyapatite nanoparticles characterization

HAP nanoparticles were synthesized through a wet precipitation reaction of  $\text{Ca}(\text{NO}_3)_2$  with  $(\text{NH}_4)_2\text{HPO}_4$  at low temperature. HAP1 particles were isolated directly and then dialyzed against PBS. HAP2 particles were formed by further hydrothermal treatment of the precipitate for 6 days followed by dialysis. Both HAP1 and HAP2 were confirmed to be pure HAP by pXRD (**Figure 2.1A**). Domain sizes along the c-axis of the nanoparticles were determined from Scherrer analysis of the {002} peak of HAP ( $25.88^\circ$ ) to be  $24 \pm 2$  nm for HAP1 and  $65 \pm 7$  nm for HAP2 (**Table 2.1**). The pXRD pattern of HAP2 showed more clearly resolvable peaks at higher angles as compared with HAP1 particles suggesting an increase in crystallinity after hydrothermal treatment.

FTIR spectra were acquired to confirm the increase in crystallinity of HAP2 particles after hydrothermal treatment (**Figure 2.1B**). The absorbance at  $635 \text{ cm}^{-1}$  is attributed to structural hydroxides in HAP and is known to increase with enhanced crystallinity [38]. This absorbance

was undetectable for HAP1, and increased in intensity for HAP2, confirming an increase in crystallinity of particles after hydrothermal treatment. Finally, the splitting factor quantifies the degree of splitting of the PO<sub>4</sub> bond bending peaks (565 cm<sup>-1</sup> and 603 cm<sup>-1</sup>) and is known to increase with increasing crystallinity [37]. HAP2 had a larger splitting factor than HAP1, as further confirmation of higher crystallinity (**Table 2.1**).

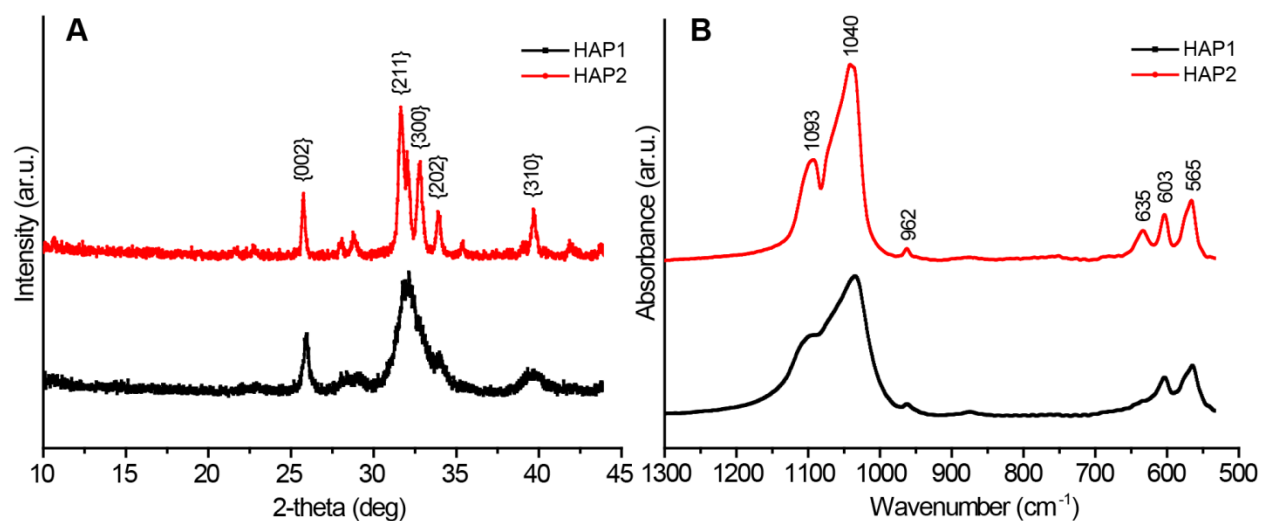


**Figure 2.1.** (A) pXRD pattern of nanoparticles. The phase of both HAP1 and HAP2 was confirmed to be pure HAP, major peaks labeled with Miller indices. (B) FTIR spectra of HAP nanoparticles. Major HAP peaks are labeled.

**Table 2.1.** Summary of hydrothermal treatment times, sizes and splitting factors of the nanoparticles.

ID	Hydrothermal treatment time [d]	Domain size along c-axis [nm] (pXRD) <sup>1</sup>	Particle size along c-axis [nm] (TEM) <sup>2</sup>	Splitting factor (FTIR) <sup>3</sup>
HAP1	0	24 ± 2	32 ± 8	3.95
HAP2	6	65 ± 7	67 ± 25	6.97

---

<sup>1</sup> Domain sizes of the particles along c-axis were determined from pXRD by Scherrer analysis of the {002} peak.

<sup>2</sup> Particle sizes along c-axis obtained from TEM were presented as means with standard deviations.

<sup>3</sup> Splitting factors were obtained from FTIR spectra by normalizing the sum of the absorbance at 565 cm<sup>-1</sup> and 603 cm<sup>-1</sup> from PO<sub>4</sub> bond bending to the minima between the two peaks.

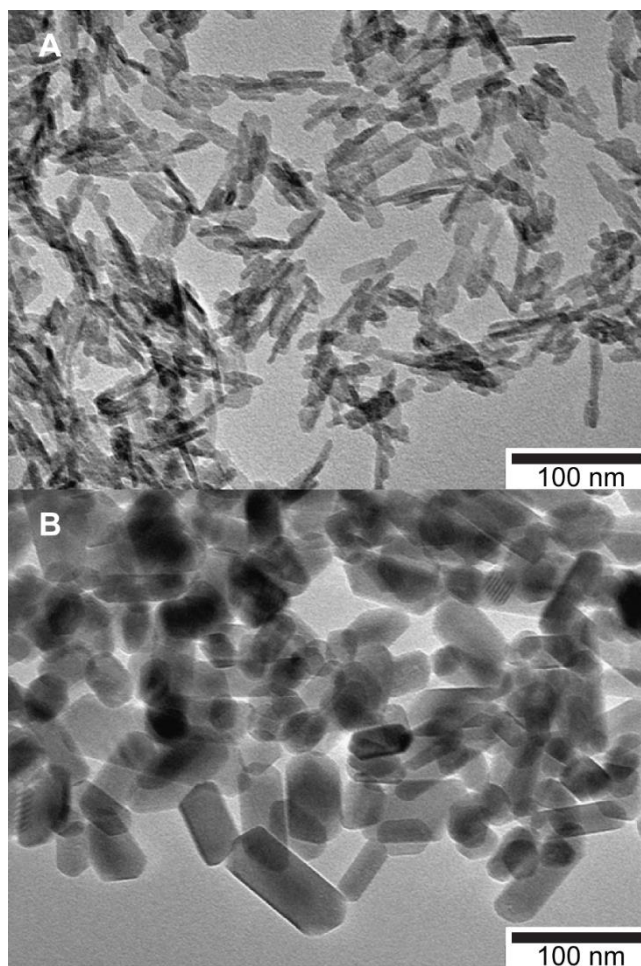


**Figure 2.2.** TEM images of HAP nanoparticles synthesized through a wet precipitation method after dialysis: (A) HAP1 (B) HAP2 (hydrothermal treatment for 6 days).

The shape and size distributions of particles were determined by TEM (**Figure 2.2**). Both HAP1 and HAP2 were elongated along the c-axis. HAP1 (**Figure 2.2A**) had a plate-like shape with an average length of  $32 \pm 8$  nm (N=213) along the c-axis; HAP2 (**Figure 2.2B**) had the shape of a hexagonal prism with an average length of  $67 \pm 25$  nm (N=688) along the c-axis (**Table 2.1**). Both HAP1 and HAP2 had narrow size distributions (**Figure 2.3**).

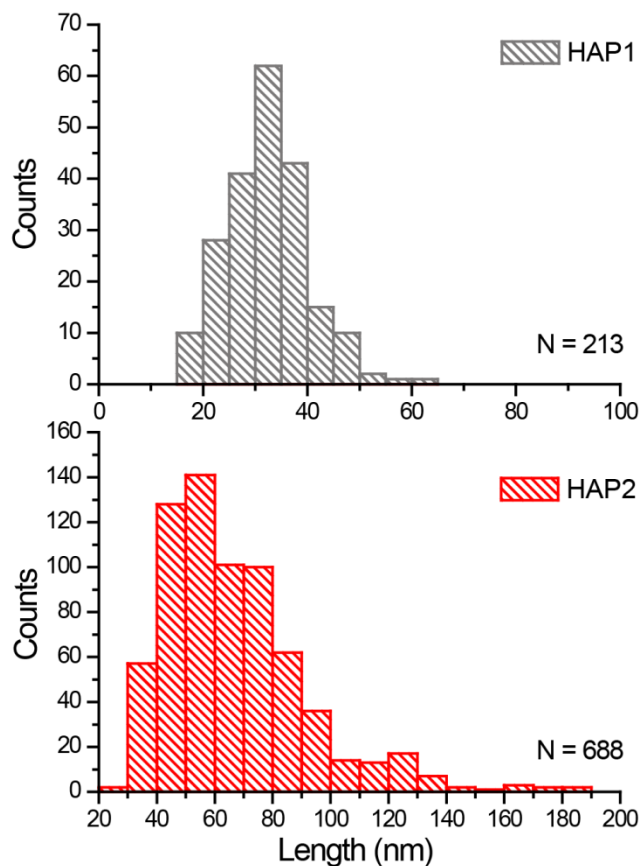


**Figure 2.3.** Size distributions along c-axis of HAP1 (top) and HAP2 (bottom) nanoparticles (TEM).

In addition to physical and structural properties, we also characterized the surface chemical properties of the nanoparticles by measuring zeta potential. Zeta potential of the particles at various concentrations was measured in PBS at pH 7.4 (**Figure 2.4**). Both HAP1 and HAP2 had negative zeta potential. At all concentrations, HAP1 had more negative zeta potential than HAP2. Moreover, the magnitude of the zeta potential decreased with increasing HAP concentration for both HAP1 and HAP2.

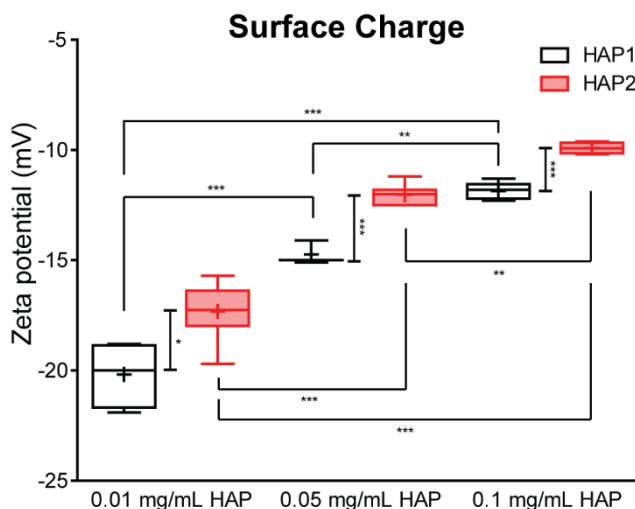


**Figure 2.4.** Zeta potential of HAP nanoparticles at various concentrations in PBS. Data collected from 3 to 6 measurements and a total of 20 to 30 runs per sample. In all cases,  $p < 0.05$  is indicated by a single star,  $p < 0.01$  by two stars and  $p < 0.001$  by three stars.

Collectively, our characterization data indicate that we have two distinct populations of HAP particles, HAP1 and HAP2. Moreover, our zeta potential results suggest that the size and morphology of HAP agglomerates evolve with increasing HAP concentration. As surface charge of each individual nanoparticle should not vary with concentration, the changes measured in zeta potential suggest that nanoparticles form agglomerates, and that the zeta potential we measured reflect surface charge of agglomerates. The changes in surface charge of agglomerates further suggest they might have different sizes and/or morphologies. For example, particles might pack differently resulting in changes in surface charge density. We next assessed the effects of the materials properties of these nanoparticles on their interaction with Fn by investigating Fn adsorption at various HAP concentrations.

#### 2.4.2 Fibronectin deposition and conformation at various hydroxyapatite concentrations

To investigate whether HAP materials properties affect their interaction with Fn, confocal images of 2D platforms containing HAP nanoparticles and Fn were acquired to quantify both the amount and the conformation of Fn adsorbed onto HAP at various HAP concentrations. A diluted Fn solution (50  $\mu\text{g/mL}$ , 10% FRET labeled) was used for incubation to ensure that only intramolecular FRET was measured to assess conformation of single Fn molecules [31]. Donor and acceptor fluorophores were imaged simultaneously (**Figures 2.5A and 2.5B**), along with a bright field image recorded in the transmission light channel (**Figure 2.5C**) for each field of view. FRET ratio was defined as acceptor/donor intensity ratio ( $I_A/I_D$ ). The color-coded FRET ratio map and FRET ratio histogram were used to calculate mean FRET ratio for each field of view (**Figures 2.5D and 2.5E**). As determined in our FRET calibration (**Figure 2.6**), together with previously published circular dichroism data [31], FRET ratio is high when Fn has a compact conformation (0M GdnHCl), decreases as Fn opens up and becomes extended (0M ~ 2M GdnHCl), and further decreases when Fn starts losing tertiary structure (2M ~ 4M GdnHCl), *i.e.* when Fn type-III modules (magenta ovals/lines in **Figure 3E** schematics) start unfolding.

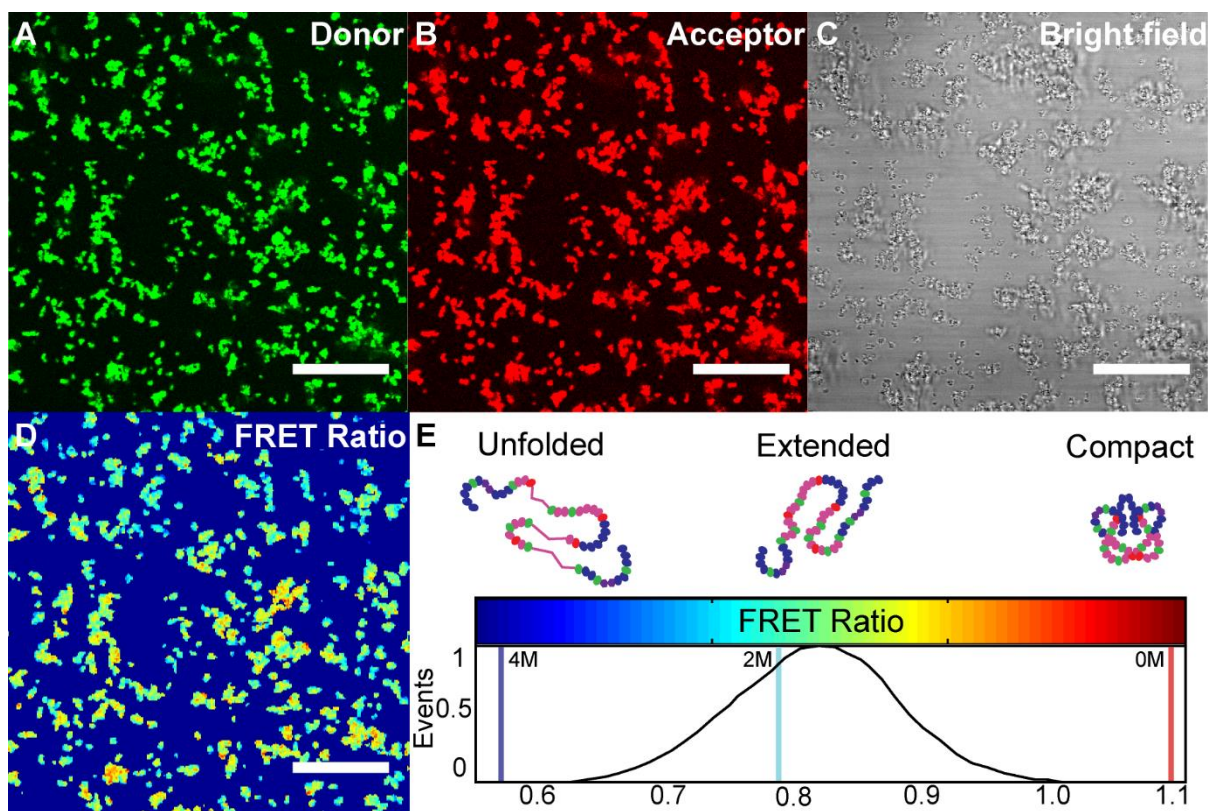


**Figure 2.5.** Confocal images for 0.05 mg/mL HAP1 nanoparticles incubated with Fn: (A) Donor channel, (B) acceptor channel, and (C) transmission light channel. (D) Color-coded FRET ratio map, with high FRET ratio color coded in red (compact Fn) and low FRET ratio in blue (unfolded Fn). (E) FRET ratio histogram for the same field of view, with schematics of Fn conformation correlated to the FRET calibration values reported in **Figure 2.6** (compact, loss of quaternary structure when extended, and loss of tertiary structure when type-III modules represented by magenta ovals/lines start unfolding) [31]. Scale bars 50  $\mu\text{m}$ .

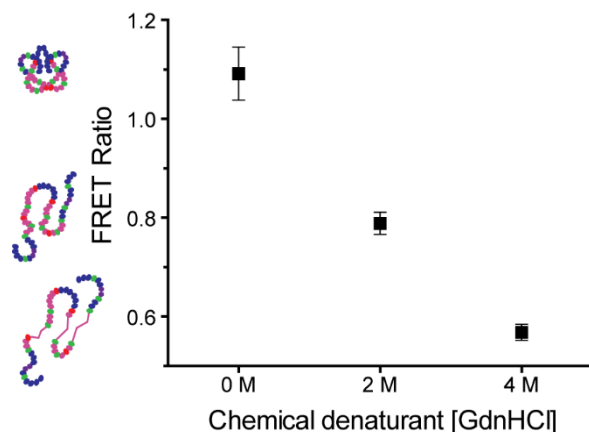


**Figure 2.6.** Soluble calibration of FRET ratio (*i.e.*, acceptor intensity/donor intensity) as a function of chemical denaturant (guanidine hydrochloride, GdnHCl) concentration. The schematics at left illustrate Fn conformations at various FRET ratios obtained via circular dichroism measurements [30]. Data shown as means and standard deviations, with 8 to 10 measurements per sample.

We first used FRET to determine the conformation of Fn adsorbed onto HAP nanoparticles at various concentrations (**Figure 2.7A**). Fn adsorbed onto HAP1 particles had systematically higher FRET ratios than Fn adsorbed onto HAP2 particles at all HAP concentrations. These data suggest that, on average, Fn molecules were more compact when adsorbed onto HAP1 than onto HAP2. Additionally, FRET ratios increased with increasing HAP concentration for both HAP1 and HAP2 particles, indicating that Fn molecules overall adopted more compact conformations as HAP concentration increased. Borosilicate coverglass and freshly cleaved mica were used as control surfaces: FRET ratios of Fn adsorbed onto coverglass and mica were  $0.642 \pm 0.008$  and  $0.494 \pm 0.007$ , respectively (data reported as mean  $\pm$  standard deviation,  $n=8$ , same Fn concentration and volume of solution per ‘apparent’ surface area were used for all experiments, but Fn surface density after adsorption varied), suggesting that Fn unfolding increased slightly

upon adsorption onto coverglass and drastically upon adsorption onto atomically smooth mica, as compared with HAP.

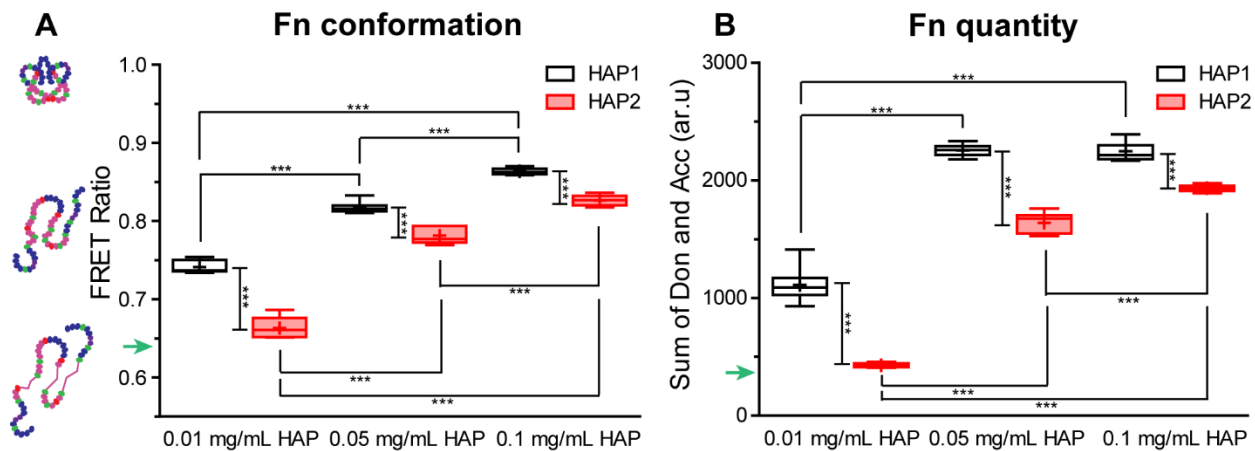


**Figure 2.7.** (A) FRET ratio and (B) amount of Fn adsorbed onto HAP1 and HAP2 at various HAP concentrations, after incubation at 4 °C for 24 hrs. All data shown were obtained from the z slice 2  $\mu$ m above the bottom coverglass, with 5 to 8 fields of view analyzed per sample. As a comparison, FRET ratio and quantity of Fn adsorbed onto coverglass (in absence of HAP) are indicated by green arrows in (A) and (B), respectively. All sample conditions were repeated three times. In all cases,  $p < 0.05$  is indicated by a single star,  $p < 0.01$  by two stars and  $p < 0.001$  by three stars.

We next quantified the amount of Fn adsorbed per unit volume onto HAP particles by monitoring the sum of donor and acceptor fluorescence intensities (**Figure 2.7B**). The sum of donor and acceptor fluorescence intensities was larger for HAP1 particles at all concentrations, suggesting that there were systematically more Fn adsorbed onto HAP1 than onto HAP2

particles. Furthermore, the amount of Fn adsorbed onto HAP2 particles increased with increasing HAP concentration, whereas the amount of Fn adsorbed onto HAP1 particles reached a plateau at high (0.1 mg/mL) HAP concentration. The sums of donor and acceptor fluorescence intensities of Fn adsorbed onto coverglass and mica were  $358 \pm 8$  and  $221 \pm 12$ , respectively (data reported as mean  $\pm$  standard deviation,  $n=8$ ), suggesting that more Fn was adsorbed onto coverglass than onto mica. In addition, the sums for both coverglass and mica were lower than those for HAP nanoparticles at all concentrations, suggesting that Fn adsorption was enhanced on HAP nanoparticles. Collectively, our data show that (i) larger amounts of more compact Fn molecules adsorbed onto HAP1 as compared with HAP2 particles, and (ii) more compact Fn tended to adsorb with increasing HAP concentration until the total amount of molecules adsorbed onto HAP reached a plateau.

#### 2.4.3 Size and Morphology of hydroxyapatite nanoparticle agglomerates

The acceptor channels of z-stack confocal images of Fn adsorbed onto HAP nanoparticles were used to generate 3-dimensional (3D) reconstruction of nanoparticle agglomerates to analyze the size, number, and morphology of the agglomerates (**Figures 2.8 and 2.9**). Both HAP1 and HAP2 particles formed microscale agglomerates in PBS. At low HAP concentration (0.01 mg/mL), the sizes of agglomerates were typically below 10  $\mu\text{m}$  (**Figures 2.8A and 2.9A**). The fluorescence intensity is proportional to the amount of Fn adsorbed per unit volume; hence the low fluorescence intensity detected at low HAP concentration suggests that only a small amount of Fn molecules was adsorbed onto the surface of nanoparticles that were assembled in a few small agglomerates. At higher HAP concentration (0.05 mg/mL), both the number and size of agglomerates increased, reaching up to 35  $\mu\text{m}$  in height (**Figures 2.8B and 2.9B**). The higher fluorescence intensity also suggests that more Fn molecules were adsorbed. Finally at 0.1

mg/mL, the size of agglomerates displayed a wide distribution, ranging from several microns to 50  $\mu\text{m}$  in height (**Figures 2.8C and 2.9C**). To exclude FRET signal from Fn adsorbed onto the bottom coverglass, we discarded the slice  $z=0$  and used the slice  $z=2 \mu\text{m}$  (above the coverglass) to quantify Fn conformation and quantity adsorbed at various HAP concentrations (**Figure 2.7**).

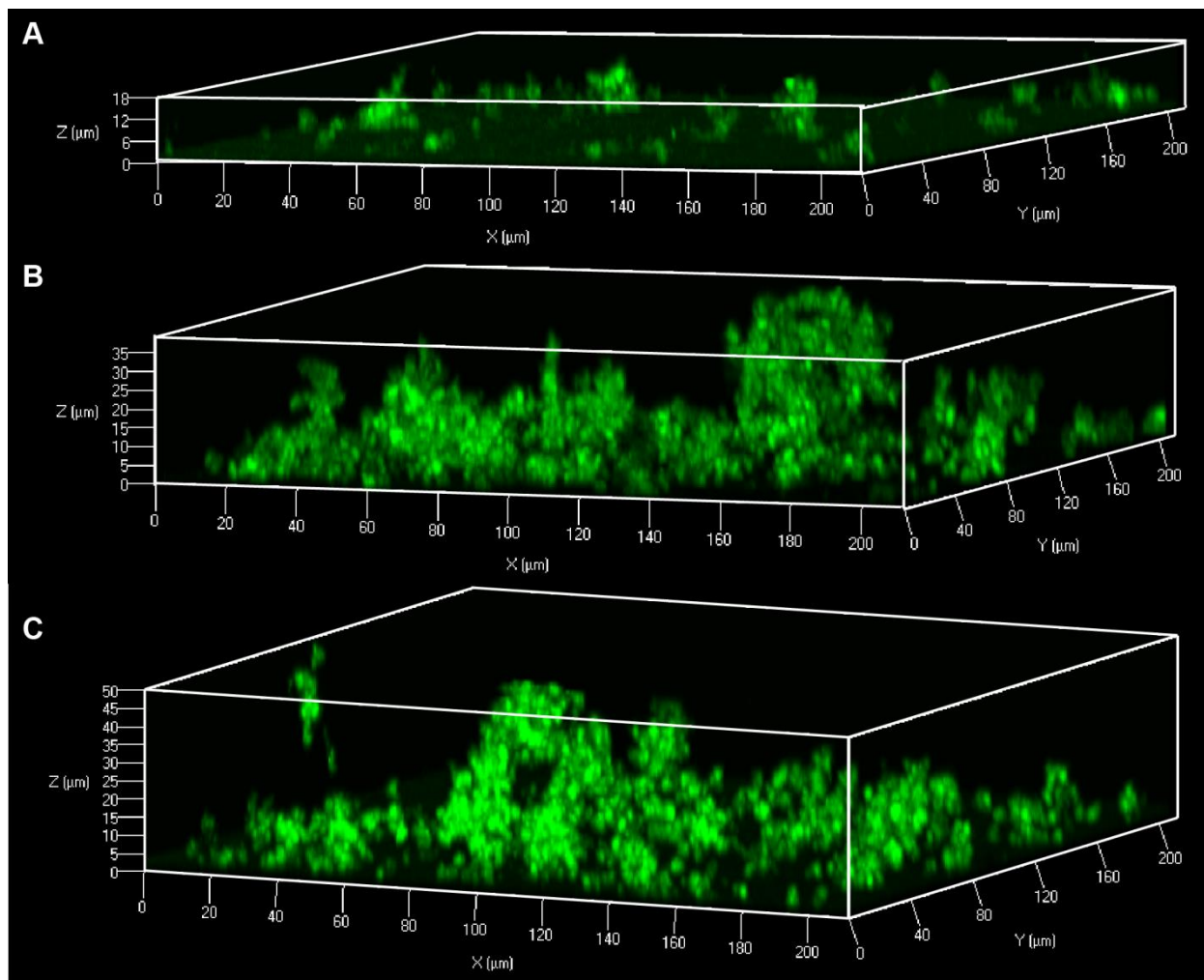


**Figure 2.8.** Confocal z-stack 3D reconstruction: size and morphology of HAP1 nanoparticle agglomerates at (A) 0.01 mg/mL, (B) 0.05 mg/mL, and (C) 0.1 mg/mL incubated with Fn in PBS.

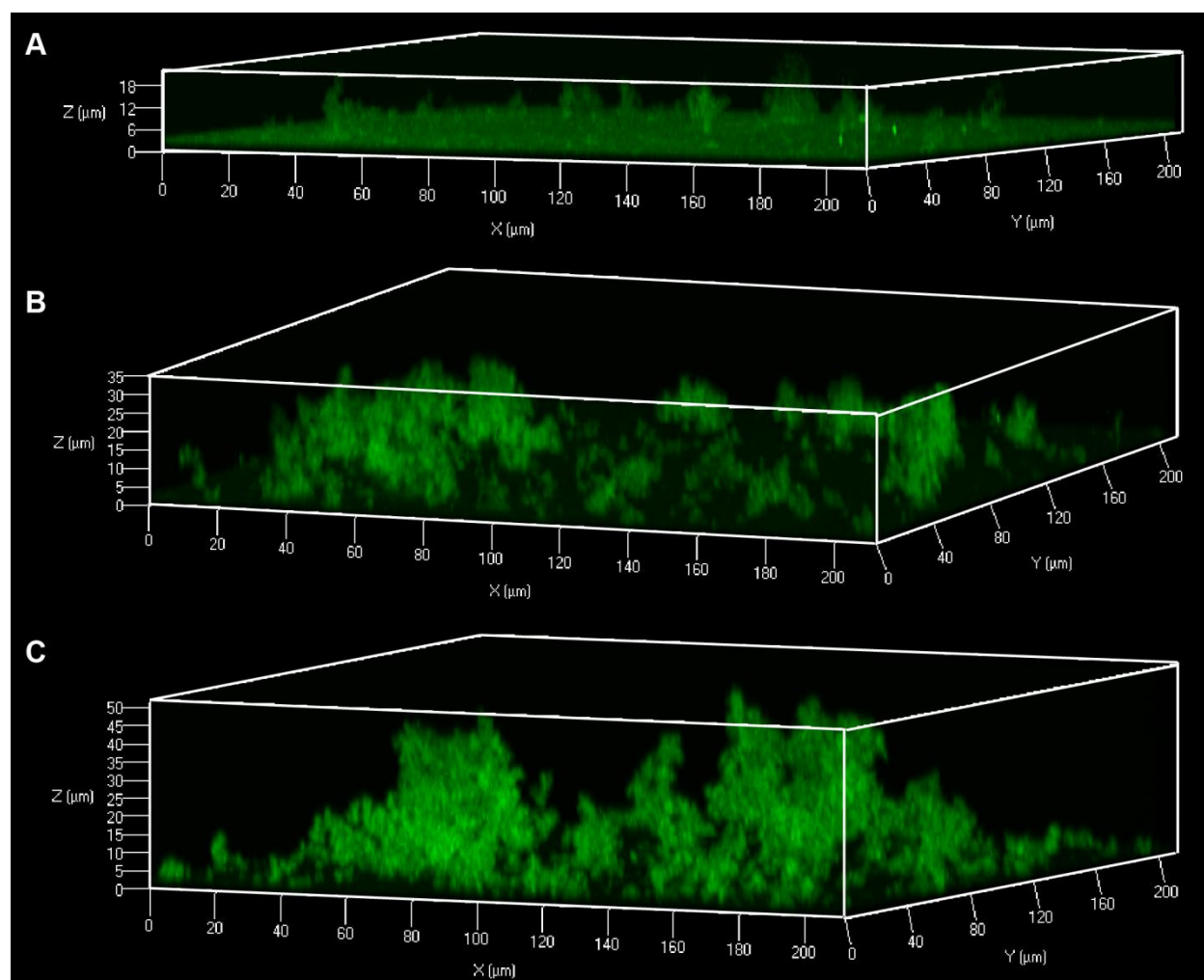


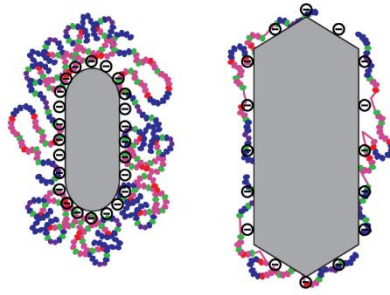
**Figure 2.9.** Confocal z-stack 3D reconstruction: size and morphology of HAP2 nanoparticle agglomerates at (A) 0.01 mg/mL, (B) 0.05 mg/mL, and (C) 0.1 mg/mL incubated with Fn in PBS.

When comparing the size and morphology of HAP1 and HAP2 agglomerates, they appeared to be similar at the same concentration (**Figures 2.8 and 2.9**). However, the fluorescence intensity of Fn was lower on HAP2 particles, confirming that less Fn molecules were adsorbed onto HAP2 than onto HAP1 particles (at equal HAP concentration), which is in agreement with results presented in **Figure 2.7**.

## 2.5 Discussion

This study demonstrates that the size, shape, and crystallinity of single HAP nanoparticles as well as particle agglomeration collectively affect both the amount and the conformation of Fn adsorbed onto HAP. Two distinctive populations of HAP nanoparticles have been used, with HAP1 particles having smaller size, plate-like shape, lower crystallinity, and more negative zeta potential than HAP2 particles. Our results show that larger amounts of more compact Fn were adsorbed onto HAP1, while smaller amounts of more extended/unfolded Fn were found on HAP2. Additionally, increased adsorption of more compact Fn was observed at higher HAP concentration, when large agglomerates were more prone to form. We thus propose that both the surface chemistry of single HAP nanoparticles and the size and morphology of HAP agglomerates contribute significantly to Fn-HAP interactions in PBS.

### A Effect of HAP surface chemistry



### B Effect of HAP agglomerate size and morphology

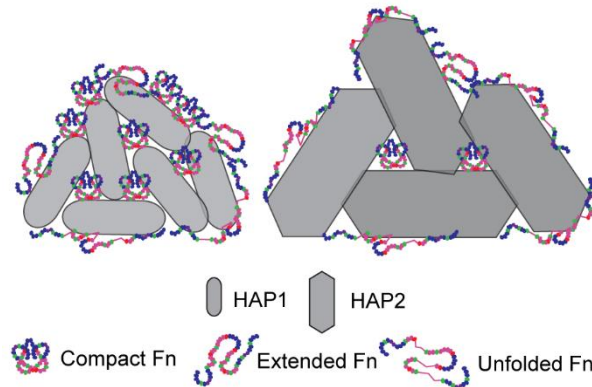


**Figure 2.10.** Effect of HAP materials properties on Fn adsorption. (A) At low HAP concentration, denser surface charge of HAP1 (more negative zeta potential than HAP2) resulted in larger amounts of more compact Fn adsorbed onto the HAP1 surface. (B) At high HAP concentration, *i.e.* in presence of large HAP agglomerates, numerous Fn molecules were trapped (in compact conformation) within the interstitial sites between nanoparticles, which outweighed the number of molecules adsorbed onto the surface of the agglomerates (in extended/unfolded conformation). The ratio of surface-Fn to interstitial-Fn decreased with increasing agglomerate size, resulting in overall larger amounts of compact Fn adsorbed at higher HAP concentration.

#### 2.5.1 Effect of hydroxyapatite nanoparticle surface chemistry on fibronectin adsorption

The more compact conformation of Fn adsorbed onto HAP1 compared with HAP2 particles is attributed to HAP surface chemistry, which directly controls electrostatic interactions between single HAP particles and Fn in PBS (**Figure 2.10A**). In support of this proposal, there have been computational studies suggesting that the adsorption of acidic proteins such as osteopontin to the (100) face and Fn-III<sub>10</sub> peptides to the (001) face of HAP is governed by electrostatics [19,20]. Given that our HAP nanoparticles are elongated along the c-axis, and that the (100) face has been shown to be the most favorable energetically in water [39], we speculate that the largest surface of our HAP nanoparticles is probably the (100) face. Between the two types of HAP nanoparticles, HAP1 particles with smaller size, plate-like shape and lower crystallinity show more negative zeta potential at all concentrations (**Figure 2.4**). The more negative zeta potential of HAP1 particles likely implies denser surface charge and thus stronger electrostatic interactions with Fn. Although Fn has an acidic isoelectric point [40], hence a net negative charge at pH 7.4, its numerous positively charged residues can readily interact with HAP surfaces through electrostatic interactions or hydrogen bonding.

The larger amount of Fn adsorbed onto HAP1 particles as compared with HAP2 particles is in agreement with previous work showing a decrease in Fn adsorption with increasing size of HAP nanoparticles [26]. Adsorption of serum proteins has also been found to increase on polymer scaffolds containing smaller and less crystalline HAP nanoparticles [36]. It should be noted that our results in **Figure 4B** indicate the amount of Fn adsorbed per unit volume, and may not be relevant to Fn adsorbed per unit surface area onto the nanoparticles. Each voxel ( $0.4 \times 0.4 \times 1.0 \mu\text{m}^3$ ) can accommodate approximately 10K of HAP1 or 1K of HAP2 nanoparticles (assuming reasonable thickness). Additionally, single HAP1 particles have higher surface area to volume ratios than single HAP2 particles. Thus, the higher level of fluorescence measured for

HAP1 compared to HAP2 could result from both the larger quantity and larger surface area of HAP1 particles per voxel, even if the same amount of Fn adsorbed per unit surface area onto HAP1 and HAP2 particles. However, our FRET results in **Figure 2.7A** indicate that Fn adopts a more compact conformation and hence takes less space when adsorbed onto HAP1, suggesting that there is also likely more Fn adsorbed per unit surface area on HAP1 than on HAP2.

Moreover, we observe a correlation between the quantity and the conformation of Fn adsorbed, with larger Fn amounts correlating systematically to more compact Fn conformations. This correlation can be attributed either to a reduced space available for each Fn molecule adsorbed, or to stronger protein-protein interactions that stabilize compact Fn conformation at high surface coverage (in particular on HAP1 surface). Our data are in agreement with previous work reporting a similar relationship between the interfacial concentration and conformation of Fn adsorbed onto hydrophobic polystyrene, in which the authors suggested that molecular packing and protein-protein interactions at high Fn bulk concentration reduced Fn molecular unfolding [41], even when the underlying hydrophobic surface would tend to induce Fn unfolding by exposure of the hydrophobic protein core. On hydrophilic surfaces, such as mica, the orientation and conformation of Fn have been shown to depend on surface coverage as well, where increasing specific interactions with collagen-related peptides is observed at higher surface coverage [42]. In fact, our FRET results show that Fn molecules adsorbed onto atomically smooth mica at very low bulk concentration (50  $\mu\text{g}/\text{mL}$ ) are mostly unfolded.

### 2.5.2 Evolving size and morphology of hydroxyapatite agglomerates with increasing particle concentration

The stability of a colloidal system can be indicated by the magnitude of the zeta potential. Previous work has shown that a smaller magnitude of zeta potential indicates weaker electrostatic repulsion between nanoparticles and hence promotes the formation of agglomerates [43]. Our zeta potential results suggest that the size and morphology of HAP agglomerates evolve with increasing HAP concentration (**Figure 2.4**), as further confirmed by our 3D reconstruction of z-stack confocal images (**Figures 2.8 and 2.9**). According to Figures 2.8 and 2.9, the morphology of HAP agglomerates is fractal-like and heterogeneous in both size and shape, as observed for other colloidal systems [44,45]. Although the size of agglomerates is widely distributed, larger agglomerates are more likely to form at higher HAP concentration, as suggested by the decrease in the magnitude of the zeta potential.

### 2.5.3 Effect of hydroxyapatite agglomerate size and morphology on fibronectin adsorption

We attribute the more compact conformation of Fn detected at higher HAP concentration to the varying size and morphology of HAP agglomerates (**Figure 2.10B**). At higher HAP concentration, the magnitude of the zeta potential of agglomerates decreases, implying that surface chemistry and electrostatic interactions might play less central roles in the overall Fn adsorption onto and within HAP agglomerates. Instead, the size and morphology of HAP agglomerates could be the dominant factors. Given that larger amounts of more compact Fn were measured at higher HAP concentration, *i.e.*, when large agglomerates are more prone to form, we speculate that the enhanced Fn adsorption and stabilization of compact conformation correlate to the formation of large HAP agglomerates.

We further suggest that the numerous interstitial sites between HAP nanoparticles in large agglomerates are responsible for trapping most Fn molecules in compact conformation within the

interstices of bulk agglomerates (**Figure 2.10B**). In support of this proposal, a previous study has demonstrated the stabilization of protein conformation within nanopores having an optimal size due to favorable confinement [17]. As the surface to volume ratio is proportional to  $1/R$  (assuming spherical agglomerates,  $R$  being the radius), the ratio of surface-Fn to interstitial-Fn decreases with increasing agglomerate size. Therefore, the FRET signal detected at high HAP concentration comes mostly from interstitial-Fn (more compact) trapped within the volume of large agglomerates rather than from surface-Fn (more extended/unfolded). Although the exact size and shape of the interstitial sites between HAP nanoparticles are not known, increasing HAP concentration might result in smaller interstitial sites with dimensions comparable to the characteristic size of compact Fn, which is around 20 nm [40]. Alternatively, the local electrostatic environment within the interstitial sites, such as ionic strength, might also induce conformational changes of Fn.

The mechanism proposed above can also explain the increase in FRET ratio as a function of  $z$  height at high HAP concentrations (**Figure 2.11**). At low HAP concentration (0.01 mg/mL), when the size and morphology of HAP agglomerates were similar at various  $z$  height (**Figures 2.8A and 2.9A**), FRET ratios were independent of  $z$  height for both HAP1 and HAP2 particles. At higher HAP concentrations (0.05 mg/mL and 0.1 mg/mL), FRET ratio steadily increased with  $z$  height, suggesting that Fn conformation became more compact at higher  $z$  slices. Larger  $z$  height is associated with the presence of a larger fraction of big agglomerates, and the favorable stabilization due to interstitial sites contributes to the more compact Fn conformation on average. This effect is most evident at 0.1 mg/mL HAP nanoparticles. In addition, the lower FRET measured for Fn adsorbed onto coverglass at the bottom also contributes to this effect.

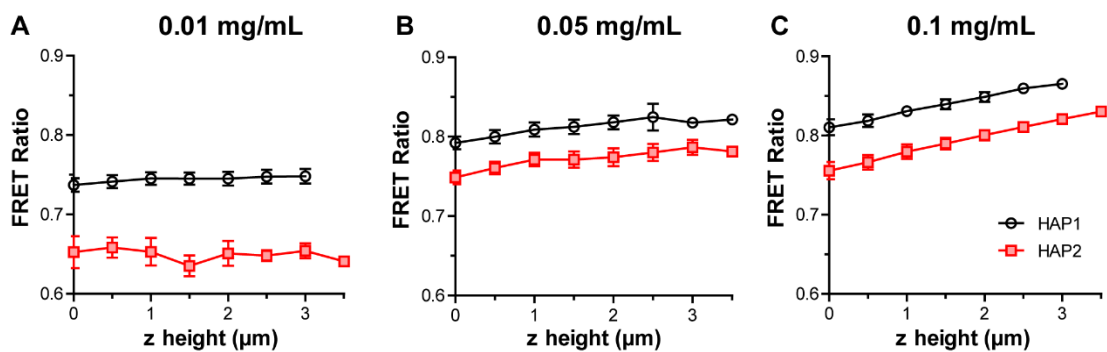


**Figure 2.11.** FRET ratios of Fn adsorbed as a function of z height at (A) 0.01 mg/mL, (B) 0.05 mg/mL, and (C) 0.1 mg/mL HAP nanoparticles. Results were obtained from 3 to 4 fields of view per sample. All data shown as means and standard deviations.

Consistently, the more compact conformation of Fn detected at higher HAP concentration again correlates to higher amounts of Fn adsorbed, as previously discussed (**Figure 2.7**). However, in the case of HAP1, the quantity of Fn measured per unit volume reached a plateau at high HAP concentration (0.1 mg/mL). The plateau does not necessarily indicate monolayer coverage, as Fn molecules could also be trapped between nanoparticles within agglomerates even if the HAP surface is saturated with a monolayer of Fn. One possible explanation is that at 0.1 mg/mL of HAP1, there was a lack of available Fn molecules in the initial solution because of the very low bulk concentration (50  $\mu\text{g/mL}$ ). Such effect is not visible on HAP2 because, as previously discussed, there are circa 10 times more HAP1 than HAP2 particles per unit volume.

Our 2D platforms containing Fn adsorbed onto HAP nanoparticles provide a reliable tool to control the conformation of proteins by tuning the materials properties of nanoparticles onto which they are adsorbed. The materials properties of HAP nanoparticles, including size, shape, crystallinity, zeta potential, together with the conformation and amount of Fn adsorbed have

been well characterized. Thus these platforms are ready to be exploited for investigating cellular behaviors such as cell adhesion, secretion and migration as a function of Fn conformation and mineral materials properties. For example, our HAP1 particles closely resemble bone apatite in terms of size, shape, crystallinity and surface chemistry (negative zeta potential), and hence can be used for studying bone remodeling and cancer metastasis to bone [5,34]. In fact, the nanoscale materials properties of HAP have been shown to affect breast tumor cell adhesion, growth, secretion and migration [36,46]. In addition, HAP has been found in inflammation-associated calcifications whereby the materials properties of HAP change as a function of disease progression [47,48]. However, one major problem with using bare nanoparticles in cell culture platforms is potential cellular uptake, which may cause cytotoxicity [45,49]. This issue is addressed by using macroscale geologic crystals instead, as described in Chapter 3.

We anticipate that the HAP-induced conformational changes of Fn will regulate several cell functions by modulating the type of binding sites that will be exposed or disrupted on Fn, in particular the integrin binding sites located on Fn-III<sub>9-10</sub> used for cell attachment. Work by Boettiger *et al.* has shown that cell adhesion strength increases with surface density of Fn [50]; moreover, conformational changes of surface-bound Fn modulate integrin binding and control cell signaling, such as proliferation and differentiation [51,52]. Additionally, our recent studies also indicate that unfolding of Fn decreases cell adhesion while enhancing secretion of vascular endothelial growth factor by pre-adipocytes in both 2D [53] and 3D [54] environments, due to the favored use of  $\alpha_v\beta_3$  (strain-insensitive) over  $\alpha_5\beta_1$  (strain-sensitive) integrins when cells interact with Fn. In the current study, the lower surface density and more unfolded conformations of Fn adsorbed onto HAP2 are expected to lead to similar cell behaviors, *i.e.*, decreased cell adhesion and enhanced secretion of pro-angiogenic growth factors. In such a context, our

platforms can help us elucidate how HAP materials properties affect not only the biological function of Fn but also subsequent cell behaviors, providing insights into biological processes such as bone healing, osteoporosis, cancer metastasis to bone, and HAP-related inflammation [47,48,55,56].

## **2.6 Conclusions**

We have combined nanoparticle synthesis with FRET spectroscopy to quantify the deposition and conformation of Fn adsorbed onto HAP nanoparticles with various materials properties. Our data reveal that larger amounts of more compact Fn molecules adsorbed onto HAP nanoparticles with smaller size, lower crystallinity, and more negative zeta potential, i.e., onto HAP that resembled bone apatite. Additionally, we report a systematic increase in the adsorption of compact Fn molecules with increasing HAP concentration, which was attributed to the formation of larger HAP agglomerates. Collectively, our findings suggest that both the surface chemistry of single HAP nanoparticles and the size and morphology of HAP agglomerates contribute to Fn adsorption [57]. Using our 2D HAP-Fn platforms, further studies of the role of Fn conformation in regulating subsequent cellular behavior, such as cell adhesion and growth factors secretion, will provide important insights into a wide range of physiological and pathological processes involving HAP-cell interactions. The major limitation of this platform is that cellular uptake of nanoparticles will affect cell viability and behaviors. Common strategies to address this problem include surface modification of nanoparticles [49] and embedding nanoparticles in polymer scaffolds [36]. In Chapter 3, large geologic apatite single crystals were used to bypass this issue and also to enable the deconvolution of surface chemistry and topography effects.

## REFERENCES

- [1] A.P. Kaplan, K. Joseph, M. Silverberg, Pathways for bradykinin formation and inflammatory disease, *J. Allergy Clin. Immunol.* 109 (2002) 195–209. doi:10.1067/mai.2002.121316.
- [2] J.J. De Yoreo, P.M. Dove, Shaping crystals with biomolecules, *Science.* 306 (2004) 1301–1302. doi:10.1126/science.1100889.
- [3] A. George, A. Veis, Phosphorylated proteins and control over apatite nucleation, crystal growth, and inhibition., *Chem. Rev.* 108 (2008) 4670–93. doi:10.1021/cr0782729.
- [4] G. Hunter, H. Goldberg, Modulation of crystal formation by bone phosphoproteins: role of glutamic acid-rich sequences in the nucleation of hydroxyapatite by bone sialoprotein., *Biochem. J.* 302 (1994) 175–179. <http://www.biochemj.org/bj/302/bj3020175.htm> (accessed February 15, 2015).
- [5] R.G. Hanschin, W.B. Stern, X-ray diffraction studies on the lattice perfection of human bone apatite (*Crista iliaca*)., *Bone.* 16 (1995) 355S–363S. <http://www.ncbi.nlm.nih.gov/pubmed/7626325>.
- [6] A. Boskey, Bone mineral crystal size., *Osteoporos. Int.* 14 (2003) S16–20. doi:10.1007/s00198-003-1468-2.
- [7] J.S. Yerramshetty, C. Lind, O. Akkus, The compositional and physicochemical homogeneity of male femoral cortex increases after the sixth decade., *Bone.* 39 (2006) 1236–43. doi:10.1016/j.bone.2006.06.002.
- [8] M.J. Bradshaw, M.L. Smith, Multiscale relationships between fibronectin structure and functional properties., *Acta Biomater.* 10 (2014) 1524–31. doi:10.1016/j.actbio.2013.08.027.
- [9] M. Rabe, D. Verdes, S. Seeger, Understanding protein adsorption phenomena at solid surfaces., *Adv. Colloid Interface Sci.* 162 (2011) 87–106. doi:10.1016/j.cis.2010.12.007.
- [10] E.A. Vogler, Protein adsorption in three dimensions., *Biomaterials.* 33 (2012) 1201–37. doi:10.1016/j.biomaterials.2011.10.059.

- [11] G.K. Hunter, J. O'Young, B. Grohe, M. Karttunen, H. Goldberg, The flexible polyelectrolyte hypothesis of protein-biomineral interaction, *Langmuir*. 26 (2010) 18639–46. doi:10.1021/la100401r.
- [12] D. Hanein, B. Geiger, L. Addadi, Fibronectin Adsorption to Surfaces of Hydrated Crystals. An Analysis of the Importance of Bound Water in Protein-substrate Interactions, *Langmuir*. 9 (1993) 1058–1065.
- [13] L.A. Touryan, G. Baneyx, V. Vogel, Exploiting fluorescence resonance energy transfer to probe structural changes in a macromolecule during adsorption and incorporation into a growing biomineral crystal., *Colloids Surf. B. Biointerfaces*. 74 (2009) 401–9. doi:10.1016/j.colsurfb.2009.07.004.
- [14] M.H. Lee, P. Ducheyne, L. Lynch, D. Boettiger, R.J. Composto, Effect of biomaterial surface properties on fibronectin- $\alpha 5\beta 1$  integrin interaction and cellular attachment., *Biomaterials*. 27 (2006) 1907–16. doi:10.1016/j.biomaterials.2005.11.003.
- [15] A.E. Nel, L. Mädler, D. Velegol, T. Xia, E.M. V Hoek, P. Somasundaran, et al., Understanding biophysicochemical interactions at the nano-bio interface., *Nat. Mater*. 8 (2009) 543–57. doi:10.1038/nmat2442.
- [16] M.B. Hovgaard, K. Rechendorff, J. Chevallier, M. Foss, F. Besenbacher, Fibronectin adsorption on tantalum: the influence of nanoroughness., *J. Phys. Chem. B*. 112 (2008) 8241–9. doi:10.1021/jp801103n.
- [17] L.-C. Sang, M.-O. Coppens, Effects of surface curvature and surface chemistry on the structure and activity of proteins adsorbed in nanopores., *Phys. Chem. Chem. Phys*. 13 (2011) 6689–98. doi:10.1039/c0cp02273j.
- [18] P. Elter, R. Lange, U. Beck, Atomic force microscopy studies of the influence of convex and concave nanostructures on the adsorption of fibronectin., *Colloids Surf. B. Biointerfaces*. 40 (2012) 139–46. doi:10.1016/j.colsurfb.2011.09.021.
- [19] P. V Azzopardi, J. O'Young, G. Lajoie, M. Karttunen, H.A. Goldberg, G.K. Hunter, Roles of electrostatics and conformation in protein-crystal interactions., *PLoS One*. 5 (2010) e9330. doi:10.1371/journal.pone.0009330.
- [20] J.W. Shen, T. Wu, Q. Wang, H.H. Pan, Molecular simulation of protein adsorption and desorption on hydroxyapatite surfaces., *Biomaterials*. 29 (2008) 513–32. doi:10.1016/j.biomaterials.2007.10.016.

- [21] C. Liao, Y. Xie, J. Zhou, Computer simulations of fibronectin adsorption on hydroxyapatite surfaces, *RSC Adv.* 4 (2014) 15759. doi:10.1039/c3ra47381c.
- [22] S. Goy-López, J. Juárez, M. Alatorre-Meda, E. Casals, V.F. Puentes, P. Taboada, et al., Physicochemical characteristics of protein-NP bioconjugates: the role of particle curvature and solution conditions on human serum albumin conformation and fibrillogenesis inhibition., *Langmuir.* 28 (2012) 9113–26. doi:10.1021/la300402w.
- [23] A. Dolatshahi-Pirouz, T. Jensen, M. Foss, J. Chevallier, F. Besenbacher, Enhanced surface activation of fibronectin upon adsorption on hydroxyapatite, *Langmuir.* 25 (2009) 2971–8. doi:10.1021/la803142u.
- [24] A. Dolatshahi-Pirouz, T.H.L.H.L. Jensen, K. Kolind, C. Bünger, M. Kassem, M. Foss, et al., Cell shape and spreading of stromal (mesenchymal) stem cells cultured on fibronectin coated gold and hydroxyapatite surfaces, *Colloids Surf. B. Biointerfaces.* 84 (2011) 18–25. doi:10.1016/j.colsurfb.2010.12.004.
- [25] L. Donlon, D. Nordin, D. Frankel, Complete unfolding of fibronectin reveals surface interactions, *Soft Matter.* 8 (2012) 9933. doi:10.1039/c2sm26315g.
- [26] B. Fernández-Montes Moraleda, J. San Román, L.M. Rodríguez-Lorenzo, Influence of surface features of hydroxyapatite on the adsorption of proteins relevant to bone regeneration., *J. Biomed. Mater. Res. A.* 101 (2013) 2332–9. doi:10.1002/jbm.a.34528.
- [27] K.C. Clause, T.H. Barker, Extracellular matrix signaling in morphogenesis and repair., *Curr. Opin. Biotechnol.* 24 (2013) 830–3. doi:10.1016/j.copbio.2013.04.011.
- [28] P. Singh, C. Carraher, J.E. Schwarzbauer, Assembly of fibronectin extracellular matrix, *Annu. Rev. Cell Dev. Biol.* 26 (2010) 397–419. doi:10.1146/annurev-cellbio-100109-104020.
- [29] S.L. Dallas, Q. Chen, P. Sivakumar, Dynamics of assembly and reorganization of extracellular matrix proteins., *Curr. Top. Dev. Biol.* 75 (2006) 1–24. doi:10.1016/S0070-2153(06)75001-3.
- [30] K.S. Midwood, L.V. Williams, J.E. Schwarzbauer, Tissue repair and the dynamics of the extracellular matrix., *Int. J. Biochem. Cell Biol.* 36 (2004) 1031–7. doi:10.1016/j.biocel.2003.12.003.

- [31] M.L. Smith, D. Gourdon, W.C. Little, K.E. Kubow, R.A. Eguiluz, S. Luna-Morris, et al., Force-induced unfolding of fibronectin in the extracellular matrix of living cells., *PLoS Biol.* 5 (2007) e268. doi:10.1371/journal.pbio.0050268.
- [32] A.M.D. Wan, E.M. Chandler, M. Madhavan, D.W. Infanger, C.K. Ober, D. Gourdon, et al., Fibronectin conformation regulates the proangiogenic capability of tumor-associated adipogenic stromal cells., *Biochim. Biophys. Acta.* 1830 (2013) 4314–20. doi:10.1016/j.bbagen.2013.03.033.
- [33] S.K. Akiyama, K. Olden, K.M. Yamada, Fibronectin and integrins in invasion and metastasis., *Cancer Metastasis Rev.* 14 (1995) 173–89. <http://www.ncbi.nlm.nih.gov/pubmed/8548867>.
- [34] A. Doostmohammadi, A. Monshi, R. Salehi, M.H. Fathi, S. Karbasi, U. Pieves, et al., Preparation, chemistry and physical properties of bone-derived hydroxyapatite particles having a negative zeta potential, *Mater. Chem. Phys.* 132 (2012) 446–452. doi:10.1016/j.matchemphys.2011.11.051.
- [35] G. Baneyx, L. Baugh, V. Vogel, Coexisting conformations of fibronectin in cell culture imaged using fluorescence resonance energy transfer., *Proc. Natl. Acad. Sci. U. S. A.* 98 (2001) 14464–8. doi:10.1073/pnas.251422998.
- [36] S.P. Pathi, D.D.W. Lin, J.R. Dorvee, L.A. Estroff, C. Fischbach, Hydroxyapatite nanoparticle-containing scaffolds for the study of breast cancer bone metastasis., *Biomaterials.* 32 (2011) 5112–22. doi:10.1016/j.biomaterials.2011.03.055.
- [37] S. Weiner, O. Bar-Yosef, States of preservation of bones from prehistoric sites in the Near East: A survey, *J. Archaeol. Sci.* 17 (1990) 187–196. doi:10.1016/0305-4403(90)90058-D.
- [38] H. el Feki, C. Rey, M. Vignoles, Carbonate ions in apatites: infrared investigations in the  $\nu_4$  CO<sub>3</sub> domain., *Calcif. Tissue Int.* 49 (1991) 269–74. <http://www.ncbi.nlm.nih.gov/pubmed/1760771>.
- [39] W. Zhao, Z. Xu, Y. Yang, N. Sahai, Surface Energetics of the Hydroxyapatite Nanocrystal–Water Interface: A Molecular Dynamics Study, *Langmuir.* 30 (2014) 13283–13292. <http://pubs.acs.org/doi/abs/10.1021/la503158p> (accessed February 15, 2015).
- [40] N.M. Tooney, M.W. Mosesson, D.L. Amrani, J.F. Hainfeld, J.S. Wall, Solution and surface effects on plasma fibronectin structure., *J. Cell Biol.* 97 (1983) 1686–92.

- [41] L. Baujard-Lamotte, S. Noinville, F. Goubard, P. Marque, E. Pauthe, Kinetics of conformational changes of fibronectin adsorbed onto model surfaces., *Colloids Surf. B. Biointerfaces*. 63 (2008) 129–37. doi:10.1016/j.colsurfb.2007.11.015.
- [42] J.R. Hull, G.S. Tamura, D.G. Castner, Structure and reactivity of adsorbed fibronectin films on mica., *Biophys. J.* 93 (2007) 2852–60. doi:10.1529/biophysj.107.109819.
- [43] J.M. Berg, A. Romoser, N. Banerjee, R. Zebda, C.M. Sayes, The relationship between pH and zeta potential of ~ 30 nm metal oxide nanoparticle suspensions relevant to in vitro toxicological evaluations, *Nanotoxicology*. 3 (2009) 276–283. doi:10.3109/17435390903276941.
- [44] P. Meakin, Universality in colloid aggregation, *Nature*. 339 (1989) 360–362.
- [45] A. Albanese, W. Chan, Effect of gold nanoparticle aggregation on cell uptake and toxicity, *ACS Nano*. 5 (2011) 5478–5489. <http://pubs.acs.org/doi/abs/10.1021/nn2007496> (accessed July 3, 2014).
- [46] R.F. Cox, A. Hernandez-Santana, S. Ramdass, G. McMahon, J.H. Harmey, M.P. Morgan, Microcalcifications in breast cancer: novel insights into the molecular mechanism and functional consequence of mammary mineralisation., *Br. J. Cancer*. 106 (2012) 525–37. doi:10.1038/bjc.2011.583.
- [47] L.M. Pachman, A. Veis, S. Stock, K. Abbott, F. Vicari, P. Patel, et al., Composition of calcifications in children with juvenile dermatomyositis: association with chronic cutaneous inflammation., *Arthritis Rheum*. 54 (2006) 3345–50. doi:10.1002/art.22158.
- [48] N. Eidelman, A. Boyde, A.J. Bushby, P.G.T. Howell, J. Sun, D.E. Newbury, et al., Microstructure and mineral composition of dystrophic calcification associated with the idiopathic inflammatory myopathies., *Arthritis Res. Ther*. 11 (2009) R159. doi:10.1186/ar2841.
- [49] L. Chen, J.M. Mccrate, J.C.-M. Lee, H. Li, The role of surface charge on the uptake and biocompatibility of hydroxyapatite nanoparticles with osteoblast cells., *Nanotechnology*. 22 (2011) 105708. doi:10.1088/0957-4484/22/10/105708.
- [50] D. Boettiger, D. Ph, Cell Adhesion Strength Increases Linearly with Adsorbed Fibronectin Surface Density, *Tissue Eng*. 3 (1997) 197–206.

- [51] T. Miller, D. Boettiger, Control of Intracellular Signaling by Modulation of Fibronectin Conformation at the Cell - Materials Interface, *Langmuir*. 19 (2003) 1723–1729.
- [52] D. Vega, D. Boettiger, Modulation of Cell Proliferation and Differentiation through Substrate-dependent Changes in Fibronectin, *Mol. Biol. Cell*. 10 (1999) 785–798.
- [53] K. Wang, R.C. Andresen Eguiluz, F. Wu, B.R. Seo, C. Fischbach, D. Gourdon, Stiffening and unfolding of early deposited-fibronectin increase proangiogenic factor secretion by breast cancer-associated stromal cells, *Biomaterials*. 54 (2015) 63–71. doi:10.1016/j.biomaterials.2015.03.019.
- [54] A.M.D. Wan, S. Inal, T. Williams, K. Wang, P. Leleux, L. Estevez, et al., 3D conducting polymer platforms for electrical control of protein conformation and cellular functions, *J. Mater. Chem. B*. (2015). doi:10.1039/C5TB00390C.
- [55] Y. Takamatsu, P. Simmons, R. Moore, H. Morris, L. To, J.-P. Le´vesque, Osteoclast-mediated bone resorption is stimulated during short-term administration of granulocyte colony-stimulating factor but is not responsible for hematopoietic, *Blood*. 92 (1998) 3465–3474. <http://www.bloodjournal.org/content/92/9/3465?cited-by=yes&legid=bloodjournal;92/9/3465&sso-checked=1> (accessed February 15, 2015).
- [56] G.R. Mundy, Metastasis to bone: causes, consequences and therapeutic opportunities., *Nat. Rev. Cancer*. 2 (2002) 584–93. doi:10.1038/nrc867.
- [57] F. Wu, D.D.W. Lin, J.H. Chang, C. Fischbach, L.A. Estroff, D. Gourdon, Effect of the Materials Properties of Hydroxyapatite Nanoparticles on Fibronectin Deposition and Conformation, *Cryst. Growth Des*. 15 (2015) 2452–2460. doi:10.1021/acs.cgd.5b00231.

## **Chapter 3.**

### **Differential Fibronectin Adsorption on Geologic Apatite Crystal**

#### **Facets: Effect of Surface Chemistry and Topography**

Contributors: Brian Gillis, Michael Rutzke, Lara Estroff, and Delphine Gourdon.

#### **3.1 Abstract**

Breast cancer preferentially metastasizes to bone and induces pathological tissue remodeling. The nanoscale materials properties of bone mineral are likely implicated in this (still unclear) process. In Chapter 2, we have demonstrated that several materials properties of hydroxyapatite (HAP,  $\text{Ca}_{10}(\text{PO}_4)_6(\text{OH})_2$ ) nanoparticles had significant effects on fibronectin (Fn) adsorption. However, it remains a challenge to deconvolute the roles of surface chemistry and surface topography of HAP in such phenomena. To tackle this problem, we used geologic apatite single crystals and investigated whether HAP surface chemistry and/or topography had individual effects on the mineral/extracellular matrix (ECM) interface in bone. First we cut and polished the geologic crystals to generate four types of HAP facets with two different crystallographic orientations (or surface chemistries), (100) and (001), each of them at two levels of surface roughness, 200 nm (rough) and 1 nm (smooth). Then we investigated the deposition and conformation of Fn adsorbed onto these HAP facets via Förster resonance energy transfer (FRET). Our FRET analysis reveals that, regardless of roughness, more compact Fn adsorbed onto (100) than onto (001) oriented facets, which was attributed to lower HAP/water interfacial

energy (more hydrophilic) and more negative zeta potential (denser surface charge) of (100) as compared with (001) facets in aqueous environment. Furthermore, higher HAP roughness resulted in increased Fn adsorption and more compact Fn conformations regardless of surface chemistry, which was attributed to stronger protein-protein interactions at high surface coverage and to confinement effects of Fn into the polishing grooves of rougher surfaces. Collectively, these results prove that both surface chemistry and roughness of HAP play individual roles in Fn adsorption, which likely contributes to pathological ECM remodeling and subsequent breast cancer cell behavior at the bone interface.

### **3.2 Introduction**

Bone metastasis frequently occurs in patients at advanced stage of breast cancer and remains a major source of mortality in these patients [1,2]. Bone can be viewed as a nanocomposite material composed of inorganic bone mineral deposited within an organic extracellular matrix (ECM, predominantly collagen I). Due to bone remodeling, the crystal size, chemical composition, and distribution of bone apatite vary as a function of age and disease progression [3–6]. There has been increasing evidence that the materials properties of bone apatite likely modulate the pathogenesis of breast cancer bone metastasis [7–9]. Synthetic hydroxyapatite (HAP,  $\text{Ca}_{10}(\text{PO}_4)_6(\text{OH})_2$ ) has been widely used in previous studies to mimic bone apatite with various materials properties, such as size, crystallinity, and carbonate substitution. The presence of HAP increases tumor cell adhesion, proliferation, and secretion of both proangiogenic and proinflammatory factors (such as vascular endothelial growth factor (VEGF) and interleukin-8 (IL-8), respectively) as compared with non-mineralized tumor models [8]. Furthermore, HAP

materials properties including size, crystallinity, carbonate incorporation, and morphology, all have combined and individual effects on breast cancer cell growth and secretion [9,10]. However, it remains a challenge to deconvolute the roles of HAP surface chemistry and topography in regulating tumor cell functions.

Based on our previous work (Chapter 2) indicating differential fibronectin (Fn) adsorption as a function of HAP nanoparticle materials properties, we hypothesized that HAP surface properties would consequently influence breast cancer cell fate via Fn-mediated pathways. As a critical mechanotransducer, Fn undergoes conformational changes that may activate or disrupt its binding sites, such as those for cell surface receptors notably integrins, and ultimately regulate cellular responses to chemical, physical, and mechanical signals from the microenvironment [11–15]. Although skeletal ECM is primarily composed of collagen I, Fn is the first bone matrix protein synthesized by osteoblasts and is required for subsequent deposition of collagen I [16–19]. Moreover, the continuous presence of Fn is essential for maintaining the integrity of the collagen matrix [20,21]. In terms of bone metabolism, it has been demonstrated that osteogenesis, induction of osteoblast differentiation, and survival of osteoblasts, all depend on integrin-mediated interactions between osteoblasts and Fn [22,23]. In addition to cellular Fn originating from osteoblasts, circulating plasma Fn produced by the liver is also incorporated in the bone matrix. Interestingly, it is the circulating plasma Fn that represents the predominant source of Fn affecting bone mineralization and matrix properties, while osteoblast-derived Fn isoform seems to modulate osteoblast differentiation locally without appreciably changing matrix properties [24]. Interestingly, a high staining intensity for Fn in tumors has been associated with increased mortality among patients with breast and prostate cancers; moreover, circulating plasma Fn enhances blood vessel formation and facilitates tumor growth by increasing VEGF

secretion levels and VEGF-mediated signaling. [25]. Nevertheless, further studies are required to elucidate the complex function of Fn in bone, especially in the context of cancer bone metastasis.

Biological bone apatite has a platelet-like shape with (100) being the primary face, and it interacts strongly with water [26]. Synthetic HAP also develops other faces, such as the (001) and (101) faces, although (100) is still the prevalent face. Similarly, geologic HAP usually develops the largest area of (100), and smaller area of (001) or (101). It has been demonstrated that a hydration layer is present on HAP surface in aqueous environment, and that water molecules interact differentially with (100) and (001) faces. This hydration layer can significantly affect the adsorption of biomolecules, such as Fn, onto the crystal facets. Specifically, Fn adsorbs preferentially onto ionic facets as compared with those decorated with lattice water molecules [27]. Work by Ugliengo et al. shows that the first solvation layer of water molecules adsorbs as disassociated hydroxyl groups onto (100) whereas it adsorbs as lattice water molecules onto (001) [28]. Other work by Sahai et al. reports that the hydrogen bonds network in the first hydration layer is less disturbed, and that lateral water diffusion is less impeded on (100) face as compared with the (001) face [29]. These computational studies implicate preferential Fn adsorption onto (100) as compared with onto (001) facets.

Both surface chemistry (electrostatic interactions) and surface topography have been widely shown to play important roles in protein adsorption, as discussed previously in Chapter 2. However, synthetic HAP nanoparticles usually present multiple faces and tend to form agglomerates, which renders difficult to deconvolution of the effects of face-specific surface chemistry and surface topography. This problem is tackled in this chapter by utilizing large geologic HAP crystals to generate surfaces with defined surface chemistry (by controlling crystal

orientation) and topography (by controlling surface roughness). This strategy allows us to understand how surface chemistry and topography individually modulate Fn adsorption.

### **3.3 Materials and Methods**

#### **3.3.1 Geologic HAP crystals**

Geologic apatite crystals with natural crystal termination faces were from Madagascar (Etsy, Inc). To determine the phases and elemental compositions of apatite crystals, a small portion was cut out of each crystal and ground into powders for powder X-ray diffraction (pXRD) and inductively coupled plasma atomic emission spectrometry (ICP-AES) analysis, respectively. The major phase of each crystal was determined to be HAP by pXRD (Scintag Inc. PAD-X theta–theta X-ray diffractometer, Cu K $\alpha$  1.54 Å, accelerating voltage 40 kV, current 40 mA, continuous scan, 1.0 deg/ min). For elemental composition analysis, 3 mg of powders were dissolved in 25 mL 5% HNO<sub>3</sub> at 80 °C overnight. The solutions were then diluted 1:5 and analyzed using an ICP-AES spectrometer (Spectro, Ametek Material Analysis Division).

#### **3.3.2 HAP facets preparation**

HAP crystals were cut along natural faces to generate two types of facets, (100) and (001), using a wafer cutting diamond saw. The crystallographic orientations of the facets were determined via XRD. These facets were then polished with a precision polisher (Allied High Tech, MultiPrep™ System) to obtain two types of morphology/roughness. Rough HAP facets 100R and 001R were polished using 30 μm diamond lapping films, resulting in a uniform array

of grooves on the crystal surface. Smooth HAP facets 100S and 001S were polished using 30  $\mu\text{m}$ , 9  $\mu\text{m}$ , 1  $\mu\text{m}$  diamond lapping films in sequence, and finished with 20 nm colloidal silica nanoparticles to smoothen any groove created by the lapping films. Lastly the smooth facets were polished against a polishing cloth in water for 5 min to remove the remaining silica nanoparticles. All lapping films, polishing cloths, and colloidal silica nanoparticles were obtained from Allied High Tech, Inc.

### 3.3.3 HAP surface chemistry and roughness characterization

The surface chemistry of HAP facets was characterized by measuring their surface zeta potential using phase analysis light scattering with Zetasizer Nano-ZS (Malvern Instruments Ltd. ZEN3600) [30]. The facets were mounted on a dip cell, immersed in aqueous buffer containing polystyrene latex standard at pH 9 (Malvern, DTS1235 ZP Transfer Standard,  $-42 \pm 4.2$  mV), and placed between the electrodes of the cell. The mobility of tracer particles in the vicinity of the charged surface was measured at 5 positions (surface displacements from 125  $\mu\text{m}$  to 625  $\mu\text{m}$ ), with 3 measurements per position, and fitted with linear regression to extrapolate the surface zeta potential at the HAP facet surface. The roughness of rough HAP facets 100R and 001R were measured with an optical profiler (ADE phase shift microXAM optical interferometric profiler), using a 50x objective. The roughness of smooth HAP facets 100S and 001S were measured via atomic force microscopy (AFM, Veeco Dimension 3100), using silicon cantilevers holding tetrahedral silicon tips of radius 7 nm (Olympus, spring constant 26 N/m), in tapping mode, by scanning areas of 10  $\mu\text{m}$  by 10  $\mu\text{m}$  (512 samples/line).

### 3.3.4. Fibronectin FRET labeling and adsorption

Fibronectin (Fn) was obtained from Life Technologies, NY. AlexaFluor 488 succinimydyl ester and AlexaFluor 546 maleimide (Invitrogen, CA) were used to label Fn for intramolecular FRET as previously described by Baneyx et al. [31] and Smith et al [11]. Labeling ratios and Fn concentrations were determined using a DU®730 UV/Vis spectrophotometer (Beckman, IN) at 280 nm, 495 nm, and 556 nm. Calibration of FRET labeled Fn in solution was carried out in guanidine hydrochloride (GdnHCl) solution at concentrations of 0, 2 M and 4 M to obtain FRET ratios, defined as acceptor/donor intensity ratios ( $I_A/I_D$ ), as a function of protein denaturation.

Stock solutions of Fn were diluted to 50 µg/mL using phosphate buffered saline (PBS) and then used for coating HAP facets. For FRET experiments, the diluted Fn solution contains 10% FRET labeled Fn and 90% unlabeled Fn to avoid intermolecular FRET, so that only intramolecular FRET was measured to assess conformation of single Fn molecules. A droplet of 50 µL diluted Fn solution was incubated on each HAP facet (surface area approximately 0.4 cm<sup>2</sup>) for 24 h at 4 °C. Lab-Tek 8-well chambered coverglass (Thermo Scientific, IL) was used as control, where 130 µL diluted Fn solution was added per well, for 24 h at 4 °C. After incubation, the facets and control coverglass were washed 3 times with PBS and kept immersed in PBS.

### 3.3.5. FRET data acquisition

Samples were imaged with a Zeiss 710 confocal microscope (Zeiss, Munich, Germany). 16-bit z-stack images were acquired using the C-Apochromat water-immersion 40x/1.2 objective, a pinhole of 2.4 AU (2 µm section), 488 nm laser with 5% laser power, pixel dwell time of 6.3 µs, PMT1 and PMT2 gains of 700 V, and z step size of 1 µm. FRET labeled Fn molecules were excited with a 488 nm laser line, emissions from donor and acceptor fluorophores were simultaneously collected in the PMT1 channel (514-526 nm) and the PMT2 channel (566-578

nm), respectively, while brightfield images were acquired in the T-PMT channel (transmitted light detector). These z-stack images were analyzed with a customized Matlab code to generate FRET ratio ( $I_A/I_D$ ) images and histograms, as well as mean FRET ratios for all z-slices in a z-stack. Only Fn regions in focus were analyzed in each z slice (our Matlab code allowed us to exclude out of focus regions in each image) to calculate mean FRET ratio for each field of view.

### 3.3.6 Statistical analysis

One-way ANOVA with Tukey's post test and Student's t-test were used to determine statistical significance between conditions in GraphPad Prism (GraphPad Software, Inc., CA). In all cases,  $p < 0.05$  is indicated by a single star,  $p < 0.01$  by two stars and  $p < 0.001$  by three stars.

## 3.4 Results

### 3.4.1 Apatite crystal bulk properties

The elemental compositions of apatite crystals were characterized by ICP-AES (**Figure 3.1A**). Major elements in all apatite crystals were found to be Ca and P. The Ca/P ratios were determined as 1.74, 1.70, and 1.64 for G1, G2, and G3, respectively, which were comparable to Ca/P ratio of stoichiometric HAP (1.67). Less abundant elements such as Si, S, and Mg were also present. Elements with concentrations lower than 0.01 mg/L are not shown in graph. All apatite crystals contained rare earth elements (Ce, La, Yb, and Y) that could result in laser-induced luminescence (data not shown) [32]. The intensity of laser-induced fluorescence from all three apatite crystals used was found to be negligible compared with signal from FRET labeled Fn later in our FRET study.

The phases of these apatite crystals were determined by pXRD (**Figure 3.1B**). The major phase of each crystal was identified to match the best with HAP, as compared with other apatite phases, such as chlorapatite and fluorapatite, although chloride and fluoride substitutions were also likely present. The peak at 29.4 degree suggested the presence of a minor phase, probably calcite, whose strongest peak is located at 29.6 degree. Further analysis is required to confirm the presence of calcite inclusion, which is out of the scope of this study.

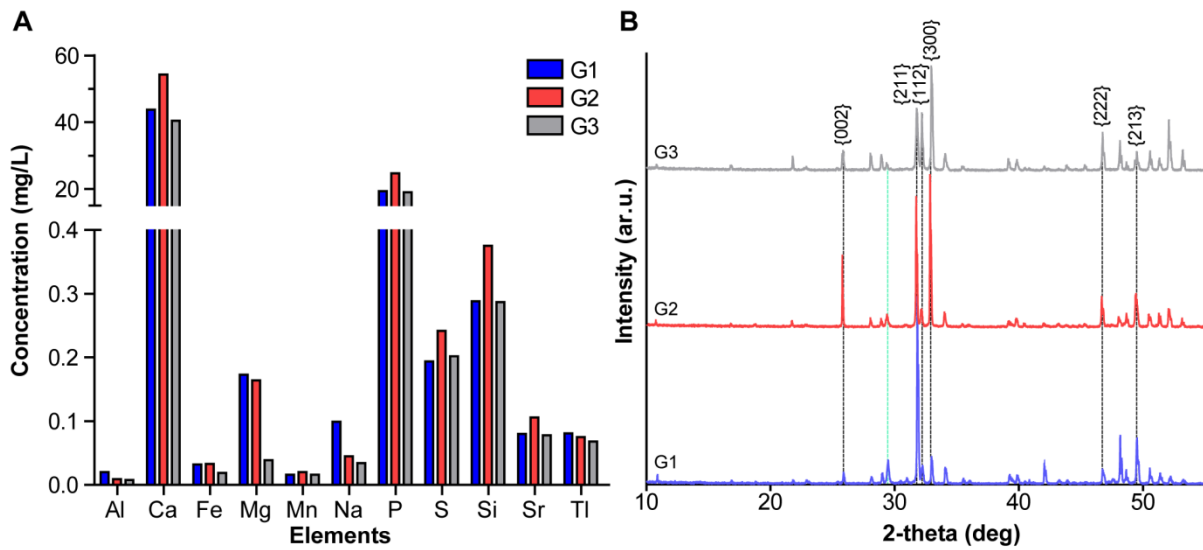


**Figure 3.1** (A) Elemental compositions of geologic apatite crystals G1, G2, and G3 were determined by ICP-AES analysis. Only elements with concentrations larger than 0.01 mg/L are shown. (B) pXRD patterns of G1, G2, and G3. Strong peaks of hydroxyapatite (HAP) are marked with black dash lines and labeled with crystal indices (ICDD PDF no. 09-0432). The peak at 29.4 degree marked with a green dash line probably originates from small amount of calcite inclusion.

### 3.4.2. HAP facets with controlled surface chemistry and roughness

HAP facets were cut along natural faces of HAP crystals and two crystallographic orientations, (100) and (001), were identified by XRD (data not shown). These facets were polished to generate two types of topography/roughness. Smooth facets 100S and 001S were characterized by AFM (**Figure 3.2A**), while rough facets 100R and 001R were analyzed with an optical profiler (**Figure 3.2B**). The surface chemistry of HAP facets was characterized by measuring their surface zeta potential in aqueous buffer. Average roughness and surface zeta potential results are summarized in **Table 3.1**.

Smooth facets 100S and 001S both had average roughness levels lower than 1 nm, with sparse cracks present on large ultra-smooth areas. This sub-nanometric roughness was chosen for smooth facets, as it compares with the size of individual modules comprising the Fn molecules (2 to 3 nm). Rough facets 100R and 001R both had average roughness levels around 200 nm, with parallel arrays of polishing grooves covering the entire surface. Such roughness was picked as it is on the order of the contour length of an extended Fn molecule. In terms of surface chemistry, (100) facets had more negative surface zeta potential than (001) facets, regardless of roughness. Moreover, smooth facets showed more negative surface zeta potential than rough facets, for both (100) and (001) orientations.

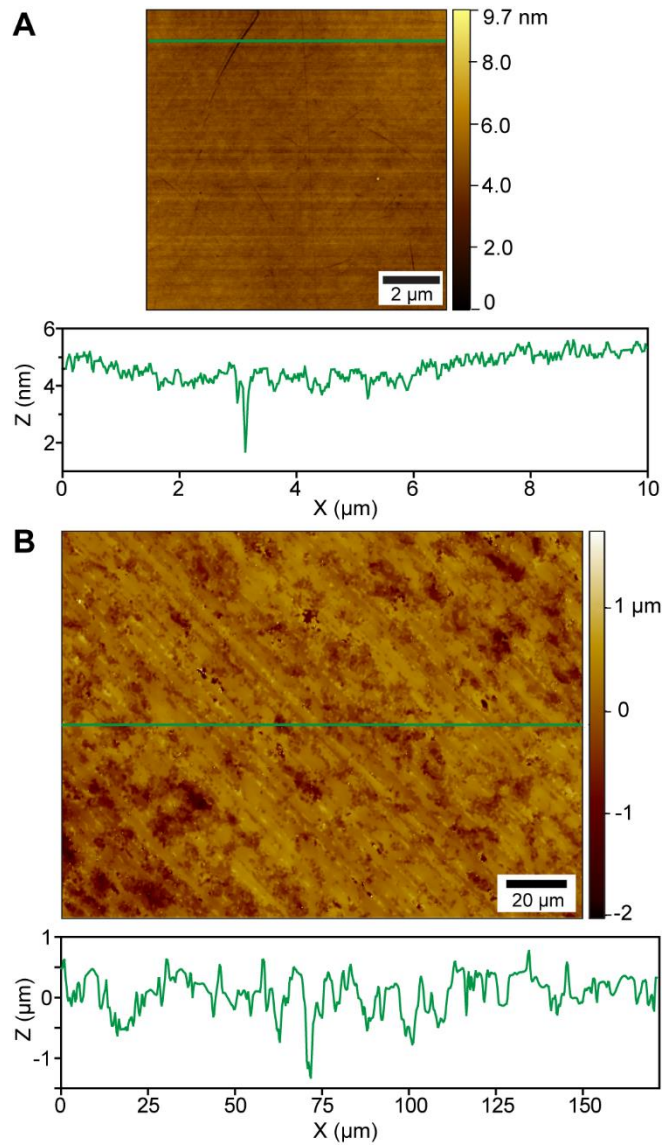


**Figure 3.2** Representative (A) AFM image of a smooth HAP facet and (B) optical profiler image of a rough HAP facet, with the line profile of a cross section marked in green shown at the bottom of each image.

**Table 3.1** Summary of surface roughness and surface zeta potential of HAP facets.

Sample ID	Average Roughness $R_a$ [nm]*	Surface zeta potential [mV]**
100S	$0.71 \pm 0.38$	$-42.4 \pm 3.0$
001S	$0.54 \pm 0.26$	$-32.1 \pm 3.5$
100R	$198.3 \pm 35.4$	$-28.1 \pm 2.8$
001R	$233.7 \pm 34.4$	$-21.8 \pm 1.7$

\*All data represented as means and standard deviations,  $N = 7$  for smooth facets 100S and 001S,  $N = 14$  for rough facets 100R and 001R.

\*\* Surface zeta potential uncertainty was defined as the 95% confidence interval of the Y-intercept (apparent zeta potential) in each linear regression fit (**Figure 3.3**). Experiments were repeated three times showing consistent trends, and only results from one experiment were shown here.

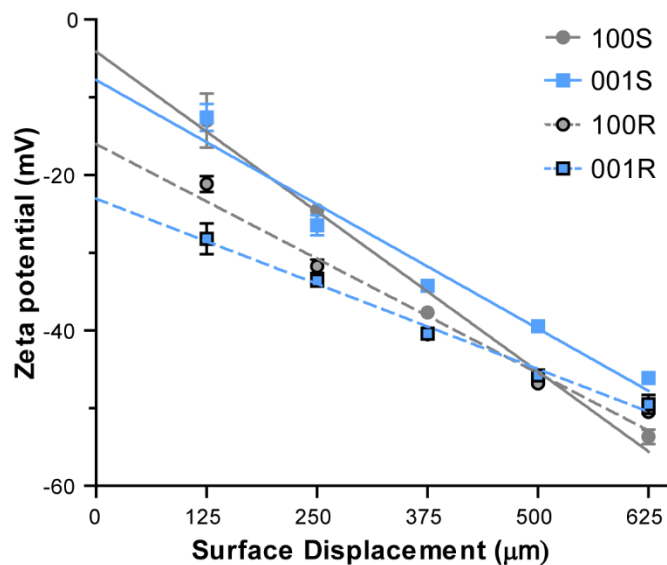


**Figure 3.3** Linear regression fit for zeta potentials measured as a function of surface displacement. Y intercept at zero displacement of each linear regression fit was subtracted from zeta potential of tracer particles to extrapolate the surface zeta potential for each HAP facet. Experiments were repeated three times showing the same trend.

### 3.4.3 Fn deposition and conformation on HAP facets

To investigate the effect of HAP surface roughness and chemistry on Fn adsorption, FRET confocal imaging was performed to quantify both the conformation and the amount of Fn adsorbed onto four types of HAP facets, 100S, 001S, 100R, and 001R. A diluted Fn solution (50  $\mu\text{g}/\text{mL}$ , 10% FRET labeled) was used for incubation to ensure that only intramolecular FRET was measured to assess conformation of single Fn molecules [11]. Donor and acceptor fluorophores were imaged (z-stacks) simultaneously (**Figures 3.4A and B**), while associated bright field images were recorded in the transmission light channel (**Figure 3.4C**). FRET ratio was defined as acceptor/donor intensity ratio ( $I_A/I_D$ ), and mean FRET ratios were calculated for

each image using the color-coded FRET ratio map and FRET ratio histograms (**Figures 3.4D and E**). As determined in our FRET calibration (**Figure 3.5**) and correlated with previously published Fn circular dichroism data [11], FRET ratio is high when Fn has a compact conformation (0M GdnHCl), decreases as Fn becomes extended (0M ~ 2M GdnHCl), and decreases further when Fn starts losing tertiary structure (2M ~ 4M GdnHCl), *i.e.* when Fn type-III modules (magenta ovals/lines in **Figure 3.4E** schematics) start unfolding.

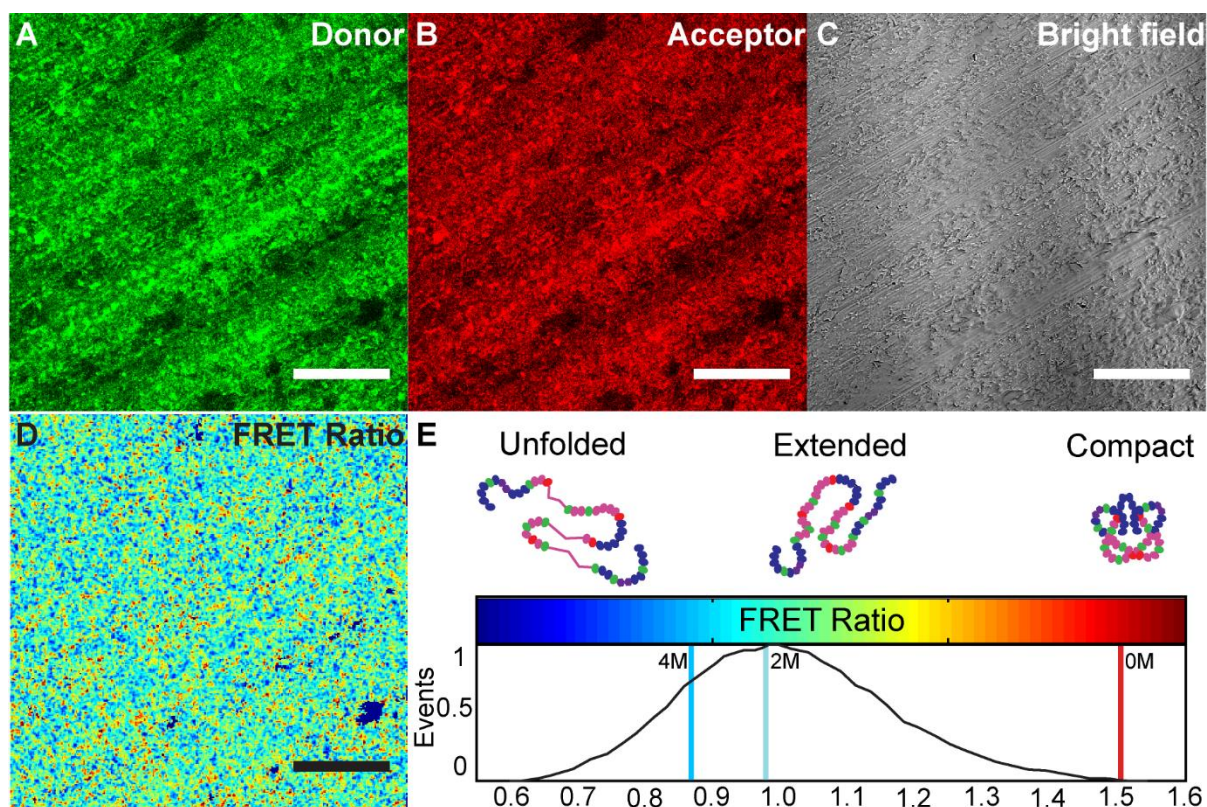


**Figure 3.4** Confocal images for a rough HAP facet coated with FRET labeled Fn: (A) donor channel, (B) acceptor channel, and (C) transmission light channel. (D) Color-coded FRET ratio map, with high FRET ratio color coded in red (compact Fn) and low FRET ratio in blue (unfolded Fn). (E) FRET ratio histogram with schematics of Fn conformation correlated to the FRET calibration values reported in **Figure 3.5** (compact, loss of quaternary structure when

extended, and loss of tertiary structure when type-III modules represented by magenta ovals/lines start unfolding). Scale bars 50  $\mu\text{m}$ . Confocal images and FRET analysis of a smooth HAP facet coated with FRET labeled Fn are shown in **Figure 3.6**.

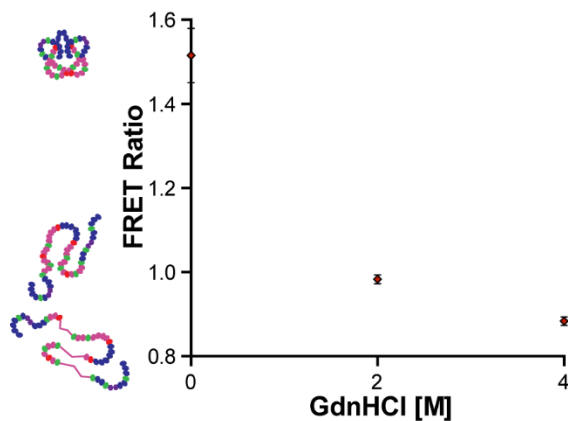


**Figure 3.5** Soluble calibration of FRET ratio (*i.e.*, acceptor intensity/donor intensity) as a function of chemical denaturant (guanidine hydrochloride, GdnHCl) concentration. The schematics at left illustrate Fn conformations at various FRET ratios obtained via circular dichroism measurements [11]. Data shown as means and standard deviations, with 10 to 12 measurements per sample.

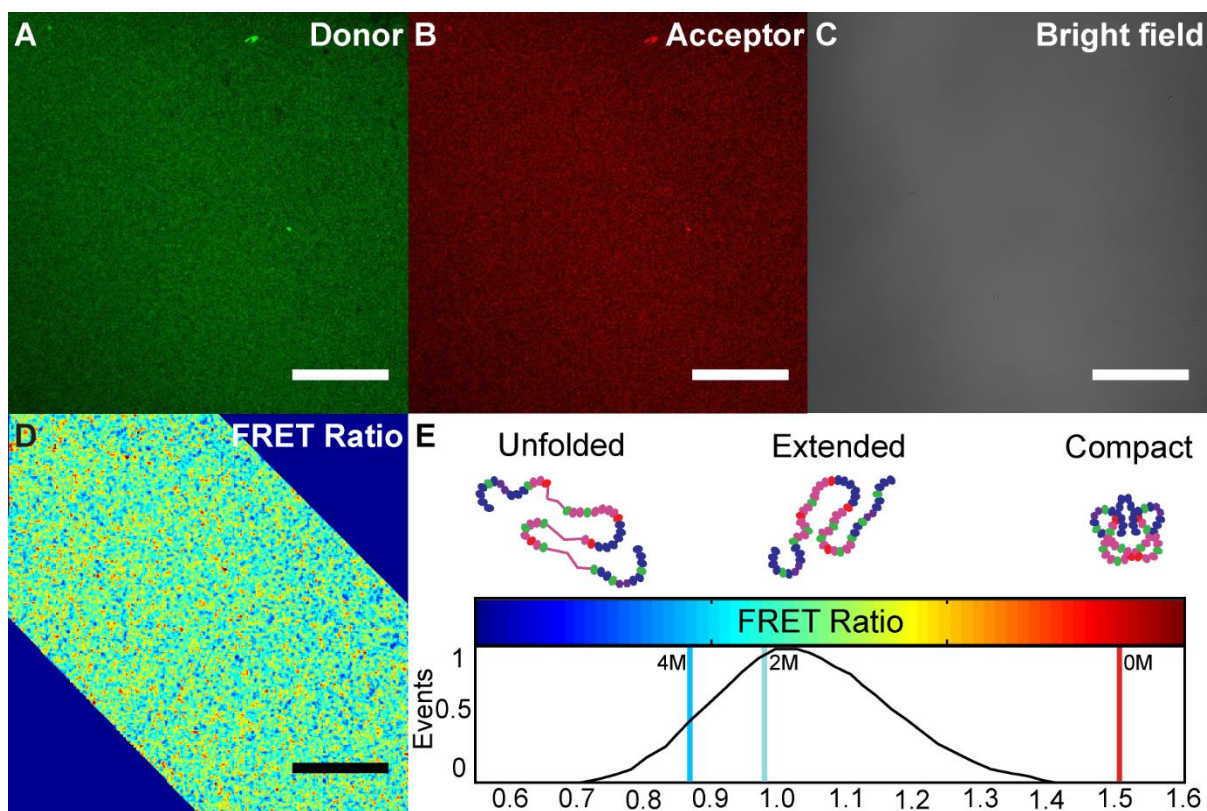


**Figure 3.6** Confocal images for a smooth HAP facet coated with FRET labeled Fn: (A) donor channel, (B) acceptor channel, and (C) transmission light channel. (D) Color-coded FRET ratio map for region of analysis (region in focus), with high FRET ratio color coded in red (compact Fn) and low FRET ratio in blue (unfolded Fn). (E) FRET ratio histogram for region of analysis, with schematics of Fn conformation correlated to the FRET calibration values reported in **Figure 3.5** (compact, loss of quaternary structure when extended, and loss of tertiary structure when type-III modules represented by magenta ovals/lines start unfolding). Scale bars 50  $\mu\text{m}$ .

First we quantified the conformation of Fn adsorbed onto HAP facets via FRET analysis (**Figure 3.7A**). FRET ratios of Fn adsorbed onto (100) facets were higher than those onto (001) facets regardless of roughness, suggesting that Fn adsorbed in more compact conformations onto

(100) oriented HAP surfaces. Additionally, FRET ratios increased with increasing roughness regardless of crystal orientation, suggesting that Fn conformation became more compact when adsorbed onto rougher HAP surfaces. 8-well Lab-Tek™ chambered coverglass (Thermo Scientific) with sub-nanometer surface roughness was used as control in all experiments.

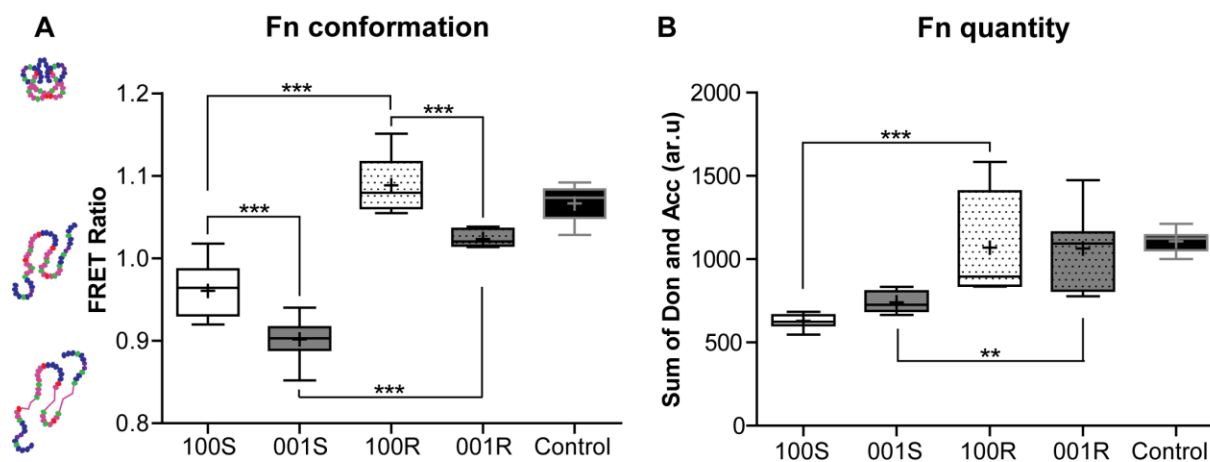


**Figure 3.7** (A) FRET ratios and (B) amount of Fn adsorbed onto HAP facets with varied surface chemistry and roughness, after incubation at 4 °C for 24 h. Data shown were obtained from 9–10 fields of view per sample. Coverglasses coated with FRET labeled Fn were used as control surfaces in all experiments. In all cases,  $p < 0.05$  is indicated by a single asterisk,  $p < 0.01$  by two asterisks, and  $p < 0.001$  by three asterisks.

Next we quantified the amount of Fn adsorbed per unit volume onto HAP facets by assessing the sum of donor and acceptor fluorescence intensities (**Figure 3.7B**). The sums of donor and acceptor fluorescence intensities were larger for rough facets than smooth facets, regardless of surface chemistry, suggesting that there were more Fn adsorbed onto rougher HAP facets.

Additionally, the amount of Fn adsorbed seemed to be independent of surface chemistry (no significant difference was noted). It should be noted that our results in **Figure 3.7B** indicate the amount of Fn adsorbed per unit volume, and may not be relevant to Fn adsorbed per unit surface area when comparing rough and smooth facets. The higher level of fluorescence measured for rougher facets could result from the larger surface area of HAP per voxel ( $0.4 \times 0.4 \times 1.0 \mu\text{m}^3$ ), instead of the larger quantity of Fn adsorbed per unit surface area. Nevertheless, Fn conformation results in **Figure 3.7A** suggested that Fn adopted more compact conformations and hence took less space when adsorbed onto rougher facets, implying that there could be more Fn adsorbed per unit surface area onto rougher facets. Collectively, our FRET data show that (i) more compact Fn molecules adsorbed onto (100) than onto (001) facets, and (ii) larger amount of more compact Fn adsorbed onto rougher HAP facets.

### 3.5 Discussion

In this chapter we utilized geologic apatite crystal facets to independently vary surface chemistry and topography for investigating protein adsorption, which we believe mediate various breast cancer cell functions. Previously, cell culture platforms utilizing synthetic HAP, including 2D HAP coatings and 3D polymeric scaffolds containing HAP nanoparticles, have demonstrated effects of HAP materials properties on serum protein adsorption and cellular behaviors [7–10]. However, the use of synthetic HAP does not allow to independently vary chemical and physical materials properties and the observed effects usually result from a combination of several materials properties. For example, increasing carbonate substitution also leads to changes in surface roughness of HAP coatings [10]. To obtain surfaces with homogeneous structural and

chemical properties, Geiger et al. synthesized calcium-(R,S)-tartrate single crystals substrates that were tens of microns large for the study of epithelial cells adhesion [33,34]. Later, geologic calcite single crystals with identical surface chemistry but different surface roughness were used as model substrates for studying nano-topography sensing by osteoclasts [35]. Herein, using geologic apatite crystals we were able to independently vary surface chemistry and topography. Specifically, we have shown that both HAP surface chemistry and roughness could independently alter the mineral/ECM interface (Fn conformation and deposition).

Four types of facets with two types of surface chemistry, (100) and (001) crystal orientations, at two levels of surface roughness, smooth and rough, were generated from geologic apatite crystals. Geologic apatite is ubiquitous in various rocks because of its overall stability in geological processes. All green apatite crystals used in this study were from Madagascar, with similar Ca/P ratios (Section 3.4.1). Many minor and trace elements can substitute in the apatite lattice (**Figure 3.1**), and the degree of substitution affects the color and stability of the lattice [36,37]. The primary natural termination faces of these crystals were identified by XRD to be (100) and (001). Computational studies have shown that in aqueous environment at pH 5 to 10, the (100) face is the most favorable energetically (lowest interfacial energy), as compared with less hydrophilic (001) face [29,38]. The hydrogen bond network in the first hydration layer is less disturbed, and lateral water diffusion is relatively free on (100) face [29]. This agrees with experimental observation of the preferred growth in the [001] direction resulting in a larger surface area of (100) compared to other faces in synthetic HAP [39].

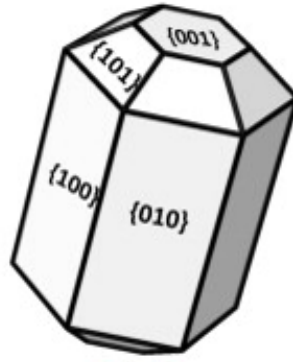


**Figure 3.8** Common facets observed in hexagonal hydroxyapatite crystal.  $\{100\}$  and  $\{001\}$  facets are equivalent in the hexagonal lattice.

The face-specific HAP surface chemistry contributes to differential Fn conformation and deposition onto (100) and (001) facets. Fn adsorbed in more compact conformation onto (100) than onto (001) facets (**Figure 3.7A**). This can be partially attributed to the lower energy barrier for water to diffuse away and for charged side chains of Fn molecules to penetrate the hydration layer and interact with surface ions of (100), as compared with (001) facets [29]. The favored kinetics of Fn adsorption on (100) suggests that more Fn molecules could adsorb per unit area in a given time, so that Fn conformation would be constrained by the surface area available per molecule. Whereas on (001), slower adsorption kinetics leads to less Fn molecules per unit area, and therefore they may have enough space to lay down and adopt a more extended conformation. From a thermodynamic perspective, the exposure of more hydrophobic core of Fn modules may also serve as driving force for Fn to extend and/or unfold on the more hydrophobic (001) facets. Additionally, the more negative zeta potential suggests denser surface charge for (100), and therefore stronger electrostatic and polar interactions with Fn. As Fn carries negative net charge in PBS at pH 7.4 [40], the macroscopic electrostatic interaction discourages Fn adsorption onto negatively charged surfaces. However, microscopic polarization of proteins, Debye force, and/or

other short-range interactions such as hydrogen bonding, can facilitate Fn adsorption (via its numerous positively charged lysines and various polar residues) onto negatively charged surfaces with high surface charge density [41]. Therefore, denser surface charge of (100) may present more binding sites for interacting with charged/polar residues on Fn, leading to enhanced adsorption and more compact Fn conformation. On the other hand, local electrostatic interactions may also affect the availability of binding sites on Fn. For example, the Fn-III<sub>9</sub> and III<sub>10</sub> modules (essential for cell adhesion, as described in Chapter 4) carry more negative charge than the surrounding sequences, and thus could be more accessible when adsorbed onto densely negatively charged surfaces due to electrostatic repulsion [42].

As surface roughness increases, both surface structure and chemistry become heterogeneous, which could result in smaller differences in interfacial energy and surface charge density between facets, yet the mechanisms proposed above could still help explain the differential Fn adsorption between 100R and 001R. Additionally, nanoscale roughness has been observed to enhance protein adsorption on substrates [43], which may explain the larger amount of more compact Fn molecules adsorbed onto rough than onto smooth facets (**Figure 3.7B**). On one hand, when larger amounts of Fn are present, stronger protein-protein interactions can help stabilizing the compact Fn conformation observed at high surface coverage [44]. On the other hand, the spatial confinement/trapping of Fn molecules within the polishing grooves of rough facets may also contribute to their compact conformation. Although Fn adopted more extended/unfolded conformations on (001) than on (100) facets, which means a larger surface area occupied per Fn molecule, no significant difference was noted between Fn amounts adsorbed on (001) and (100) facets.

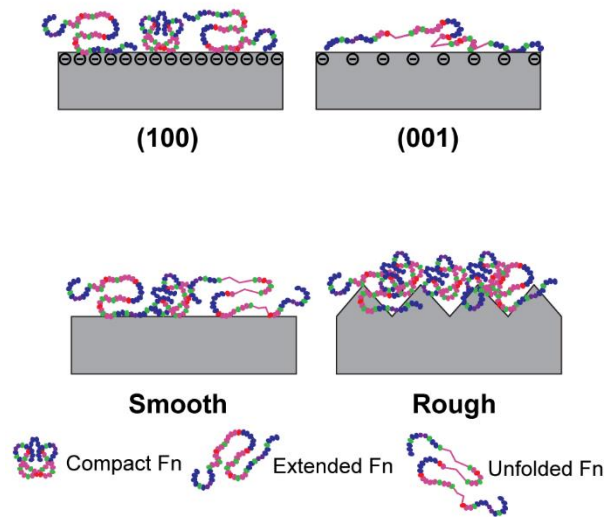


**Figure 3.8** Schematic of how surface chemistry or topography affect Fn conformation and deposition.

### 3.6 Conclusions

Using geologic HAP single crystals, we were able to deconvolute the effects of surface chemistry and topography on Fn adsorption. Our results indicate that lower interfacial energy and more negative surface charge of (100) oriented facets favored more compact Fn conformations. Adsorption kinetics, thermodynamics, local electrostatic, and/or polar interactions played important roles in this process. Our data also suggest that increasing surface roughness enhanced Fn adsorption and promoted more compact Fn conformation due to protein-protein stabilization and/or confinement effect of surface features (polishing grooves). The mechanisms proposed above are in agreement with our previous results in Chapter 2 where denser surface charge (HAP 1) and topographic confinement effects (presence of agglomerates) led to enhanced Fn adsorption and more compact Fn conformation. The differential Fn

conformation and deposition is expected to have major effects on cellular behaviors via integrin-Fn mediated pathways, which is now discussed in Chapter 4 and Chapter 5. Importantly, it needs to be noted that surface chemistry properties such as surface ion species and hydration layer are likely different between our geologic HAP crystals and biologic HAP nanoparticles [45]. Therefore the results we present with geologic HAP might not fully recapture the cell response in the bone microenvironment.

## REFERENCES

- [1] N. Sathiakumar, E. Delzell, M.A. Morrissey, C. Falkson, M. Yong, V. Chia, et al., Mortality following bone metastasis and skeletal-related events among women with breast cancer: a population-based analysis of U.S. Medicare beneficiaries, 1999-2006., *Breast Cancer Res. Treat.* 131 (2012) 231–8. doi:10.1007/s10549-011-1721-x.
- [2] M. Harries, A. Taylor, L. Holmberg, O. Agbaje, H. Garmo, S. Kabilan, et al., Incidence of bone metastases and survival after a diagnosis of bone metastases in breast cancer patients, *Cancer Epidemiol.* 38 (2014) 427–434. doi:10.1016/j.canep.2014.05.005.
- [3] R.G. Hanschin, W.B. Stern, X-ray diffraction studies on the lattice perfection of human bone apatite (Crista iliaca)., *Bone.* 16 (1995) 355S–363S.  
<http://www.ncbi.nlm.nih.gov/pubmed/7626325>.
- [4] A. Boskey, Bone mineral crystal size., *Osteoporos. Int.* 14 (2003) S16–20.  
doi:10.1007/s00198-003-1468-2.
- [5] J.S. Yerramshetty, C. Lind, O. Akkus, The compositional and physicochemical homogeneity of male femoral cortex increases after the sixth decade., *Bone.* 39 (2006) 1236–43. doi:10.1016/j.bone.2006.06.002.
- [6] A.L. Boskey, Mineralization of bones and teeth, *Elements.* 3 (2007) 385–391.  
doi:10.2113/GSELEMENTS.3.6.385.
- [7] M.S. Bendre, D.C. Montague, T. Peery, N.S. Akel, D. Gaddy, L.J. Suva, Interleukin-8 stimulation of osteoclastogenesis and bone resorption is a mechanism for the increased osteolysis of metastatic bone disease, *Bone.* 33 (2003) 28–37. doi:10.1016/S8756-3282(03)00086-3.
- [8] S.P. Pathi, C. Kowalczewski, R. Tadipatri, C. Fischbach, A novel 3-D mineralized tumor model to study breast cancer bone metastasis., *PLoS One.* 5 (2010) e8849.  
doi:10.1371/journal.pone.0008849.
- [9] S.P. Pathi, D.D.W. Lin, J.R. Dorvee, L.A. Estroff, C. Fischbach, Hydroxyapatite nanoparticle-containing scaffolds for the study of breast cancer bone metastasis., *Biomaterials.* 32 (2011) 5112–22. doi:10.1016/j.biomaterials.2011.03.055.

- [10] S. Choi, S. Coonrod, L. Estroff, C. Fischbach, Chemical and physical properties of carbonated hydroxyapatite affect breast cancer cell behavior, *Acta Biomater.* 24 (2015) 333–342. doi:10.1016/j.actbio.2015.06.001.
- [11] M.L. Smith, D. Gourdon, W.C. Little, K.E. Kubow, R.A. Eguiluz, S. Luna-Morris, et al., Force-induced unfolding of fibronectin in the extracellular matrix of living cells., *PLoS Biol.* 5 (2007) e268. doi:10.1371/journal.pbio.0050268.
- [12] A.M.D. Wan, E.M. Chandler, M. Madhavan, D.W. Infanger, C.K. Ober, D. Gourdon, et al., Fibronectin conformation regulates the proangiogenic capability of tumor-associated adipogenic stromal cells., *Biochim. Biophys. Acta.* 1830 (2013) 4314–20. doi:10.1016/j.bbagen.2013.03.033.
- [13] S.K. Akiyama, K. Olden, K.M. Yamada, Fibronectin and integrins in invasion and metastasis., *Cancer Metastasis Rev.* 14 (1995) 173–89. <http://www.ncbi.nlm.nih.gov/pubmed/8548867>.
- [14] K.C. Clause, T.H. Barker, Extracellular matrix signaling in morphogenesis and repair., *Curr. Opin. Biotechnol.* 24 (2013) 830–3. doi:10.1016/j.copbio.2013.04.011.
- [15] M.J. Bradshaw, M.L. Smith, Multiscale relationships between fibronectin structure and functional properties., *Acta Biomater.* 10 (2014) 1524–31. doi:10.1016/j.actbio.2013.08.027.
- [16] R.E. Weiss, A.H. Reddi, Appearance of fibronectin during the differentiation of cartilage, bone, and bone marrow., *J. Cell Biol.* 88 (1981) 630–6. doi:10.1083/jcb.88.3.630.
- [17] E.A. Cowles, M.E. DeRome, G. Pastizzo, L.L. Brailey, G.A. Gronowicz, Mineralization and the expression of matrix proteins during in vivo bone development, *Calcif Tissue Int.* 62 (1998) 74–82.
- [18] P. Singh, C. Carraher, J.E. Schwarzbauer, Assembly of fibronectin extracellular matrix, *Annu. Rev. Cell Dev. Biol.* 26 (2010) 397–419. doi:10.1146/annurev-cellbio-100109-104020.
- [19] S.L. Dallas, Q. Chen, P. Sivakumar, Dynamics of assembly and reorganization of extracellular matrix proteins., *Curr. Top. Dev. Biol.* 75 (2006) 1–24. doi:10.1016/S0070-2153(06)75001-3.

- [20] J. Sottile, D.C. Hocking, Fibronectin polymerization regulates the composition and stability of extracellular matrix fibrils and cell-matrix adhesions, *Mol. Biol. Cell.* 13 (2002) 3546–3559. doi:10.1091/mbc.E02-01-0048.
- [21] P.G. Grzesik, Wojciech J, Robey, Bone Matrix RGD Glycoproteins: Immunolocalization Bone Cells In Vitro, *J. Bone Miner. Res.* 9 (1994) 487–496.
- [22] A.M. Moursi, R.K. Globus, C.H. Damsky, Interactions between integrin receptors and fibronectin are required for calvarial osteoblast differentiation in vitro., *J. Cell Sci.* 110 ( Pt 1 (1997) 2187–2196.
- [23] R.K. Globus, S.B. Doty, J.C. Lull, E. Holmuhamedov, M.J. Humphries, C.H. Damsky, Fibronectin is a survival factor for differentiated osteoblasts., *J. Cell Sci.* 111 (1998) 1385–1393.
- [24] A. Bentmann, N. Kawelke, D. Moss, H. Zentgraf, Y. Bala, I. Berger, et al., Circulating fibronectin affects bone matrix, whereas osteoblast fibronectin modulates osteoblast function., *J. Bone Miner. Res.* 25 (2010) 706–715. doi:10.1359/jbmr.091011.
- [25] A. von Au, M. Vasel, S. Kraft, C. Sens, N. Hackl, A. Marx, et al., Circulating Fibronectin Controls Tumor Growth, *Neoplasia.* 15 (2013) 925–IN24. doi:10.1593/neo.13762.
- [26] M. Corno, A. Rimola, V. Bolis, P. Ugliengo, Hydroxyapatite as a key biomaterial: quantum-mechanical simulation of its surfaces in interaction with biomolecules., *Phys. Chem. Chem. Phys.* 12 (2010) 6309–29. doi:10.1039/c002146f.
- [27] D. Hanein, B. Geiger, L. Addadi, Fibronectin Adsorption to Surfaces of Hydrated Crystals. An Analysis of the Importance of Bound Water in Protein-substrate Interactions, *Langmuir.* 9 (1993) 1058–1065.
- [28] M. Corno, C. Busco, V. Bolis, S. Tosoni, P. Ugliengo, Water adsorption on the stoichiometric (001) and (010) surfaces of hydroxyapatite: a periodic B3LYP study., *Langmuir.* 25 (2009) 2188–98. doi:10.1021/la803253k.
- [29] W. Zhao, Z. Xu, Y. Yang, N. Sahai, Surface Energetics of the Hydroxyapatite Nanocrystal–Water Interface: A Molecular Dynamics Study, *Langmuir.* 30 (2014) 13283–13292. <http://pubs.acs.org/doi/abs/10.1021/la503158p> (accessed February 15, 2015).
- [30] J.C.W. Corbett, F. McNeil-Watson, R.O. Jack, M. Howarth, Measuring surface zeta

- potential using phase analysis light scattering in a simple dip cell arrangement, *Colloids Surfaces A Physicochem. Eng. Asp.* 396 (2012) 169–176.  
doi:10.1016/j.colsurfa.2011.12.065.
- [31] G. Baneyx, L. Baugh, V. Vogel, Coexisting conformations of fibronectin in cell culture imaged using fluorescence resonance energy transfer., *Proc. Natl. Acad. Sci. U. S. A.* 98 (2001) 14464–8. doi:10.1073/pnas.251422998.
- [32] M. Gaft, G. Panczer, R. Reisfeld, I. Shinno, Laser-induced luminescence of rare-earth elements in natural zircon, *J. Alloys Compd.* 300 (2000) 267–274. doi:10.1016/S0925-8388(99)00781-1.
- [33] D. Hanein, B. Geiger, L. Addadi, Differential adhesion of cells to enantiomorphous crystal surfaces., *Science* (80-. ). 263 (1994) 1413–1416. doi:10.1126/science.8128221.
- [34] E. Zimmerman, L. Addadi, B. Geiger, Effects of surface-bound water and surface stereochemistry on cell adhesion to crystal surfaces., *J. Struct. Biol.* 125 (1999) 25–38. doi:10.1006/jsbi.1998.4061.
- [35] D. Geblinger, L. Addadi, B. Geiger, Nano-topography sensing by osteoclasts., *J. Cell Sci.* 123 (2010) 1503–1510. doi:10.1242/jcs.060954.
- [36] D.A. Grisafe, F.A. Hummel, Crystal Chemistry and Color in Apatites Containing Cobalt, Nickel, and Rare-earth Ions, *Am. Mineral.* 55 (1970) 1131.
- [37] D.R. Wier, C.A. Black, S.H. Chien, Transformation of Hydroxyapatite to Fluorapatite, *Soil Sci. Soc. Am. Proc.* 36 (1972) 285. <Go to ISI>://A1972M304900013.
- [38] Tzu-Jen, H. Heinz, Accurate Force Field Parameters and pH Resolved Surface Models for Hydroxyapatite to Understand Structure, Mechanics, Hydration, and Biological Interfaces, *J. Phys. Chem. C.* 120 (2016) 4975–4992. doi:10.1021/acs.jpcc.5b12504.
- [39] I.S. Neira, Y. V. Kolen'ko, O.I. Lebedev, G. Van Tendeloo, H.S. Gupta, F. Guitián, et al., An Effective Morphology Control of Hydroxyapatite Crystals via Hydrothermal Synthesis, *Cryst. Growth Des.* 9 (2009) 466–474.
- [40] N.M. Tooney, M.W. Mosesson, D.L. Amrani, J.F. Hainfeld, J.S. Wall, Solution and surface effects on plasma fibronectin structure., *J. Cell Biol.* 97 (1983) 1686–92.

- [41] J. Lin, H. Chang, W. Kao, K. Lin, H. Liao, Y. You, et al., Effect of Surface Potential on Extracellular Matrix Protein Adsorption, *Langmuir*. (2014) 10328–10335.
- [42] T. Miller, D. Boettiger, Control of Intracellular Signaling by Modulation of Fibronectin Conformation at the Cell - Materials Interface, *Langmuir*. 19 (2003) 1723–1729.
- [43] M.H. Lee, P. Ducheyne, L. Lynch, D. Boettiger, R.J. Composto, Effect of biomaterial surface properties on fibronectin- $\alpha 5\beta 1$  integrin interaction and cellular attachment., *Biomaterials*. 27 (2006) 1907–16. doi:10.1016/j.biomaterials.2005.11.003.
- [44] L. Baujard-Lamotte, S. Noinville, F. Goubard, P. Marque, E. Pauthe, Kinetics of conformational changes of fibronectin adsorbed onto model surfaces., *Colloids Surf. B. Biointerfaces*. 63 (2008) 129–37. doi:10.1016/j.colsurfb.2007.11.015.
- [45] D. Grossin, S. Rollin-Martinet, C. Estournès, F. Rossignol, E. Champion, C. Combes, et al., Biomimetic apatite sintered at very low temperature by spark plasma sintering: Physico-chemistry and microstructure aspects, *Acta Biomater*. 6 (2010) 577–585. doi:10.1016/j.actbio.2009.08.021.

## **Chapter 4.**

# **Fibronectin-Mediated Breast Cancer Cells Interactions with Geologic Apatite Crystal Facets**

Contributors: Weisi Chen, Nicole Marroquin, Claudia Fischbach, Lara Estroff, and Delphine Gourdon.

### **4.1 Abstract**

Geologic hydroxyapatite (HAP) facets with controlled surface chemistry and topography were functionalized with (physisorbed) fibronectin (Fn) and seeded with MDA-MB-231 breast cancer cells for studying cellular functions, including cell viability, cell adhesion, focal adhesion (FA) assembly, and secretion of proangiogenic and proinflammatory factors. Our results show that breast cancer cell viability and adhesion after either 6 h or 24 h were similar on all four types of facets tested: smooth 100S and 001S, and rough 100R and 001R. However, FA formation, in particular number of FAs per cell and FA size, were strongly dependent on underlying Fn layer and HAP surface properties. Cells seeded on 001S developed higher numbers of larger FAs (per cell) than FAs assembled by cells on 100S. Moreover, cell secretions of both vascular endothelial growth factor (VEGF) and interleukin-8 (IL-8) were significantly higher on smooth facets than on rough facets after 24 h. These cellular behaviors' variations are likely associated with the engagement of different integrins (cell surface receptors) with Fn, which affects the recruitment of FA accessory proteins and triggers modified intracellular signaling cascades. Collectively, our

data suggest that Fn could play a critical role in breast cancer cells' sensing of bone mineral (closely related to HAP) materials properties. These results have important implications for our understanding of the mechanisms driving breast cancer bone metastasis.

## 4.2 Introduction

In this chapter, we investigated whether the HAP-induced differential adsorption of fibronectin (Fn) (characterized in Chapter 3) would impact breast cancer cell functions, in particular their integrin-mediated adhesion and proangiogenic/proinflammatory secretions.

Cancer cell adhesion to the surrounding extracellular matrix (ECM) is an essential step required for cell migration and particularly tissue invasion, a hallmark of the metastatic cascade. Transmembrane receptors notably integrins, a family of 24 ubiquitous  $\alpha/\beta$  heterodimers, have been identified as key regulators of this process. Each integrin binds specifically to a defined set of extracellular ligands, transducing biochemical, physical, and mechanical signals for cells to sense and respond to their microenvironment [1]. During cell attachment to ECM ligands, integrins cluster at the cell surface and act as a platform for recruiting numerous intracellular accessory proteins to form structures called focal adhesions (FAs) that link the ECM to the actin cytoskeleton. FAs contain hundreds of different proteins with conserved nanoscale protein organization and spatially segregated protein-protein interactions [2]. Among these proteins vinculin is often used as a marker for FA because it is ubiquitous in FA complexes, and it is an essential accessory protein for promoting the formation of FAs [3], facilitating ECM mechanosensing [4], and regulating actin cytoskeletal dynamics [5]. Cell-ECM interactions via integrins have been widely indicated to mediate cell adhesion, migration, and invasion through

remodeling of the ECM [3]. For example, the  $\beta_1$  integrins family was shown to play a specific role in regulating breast cancer cell adhesion and spreading, formation of FAs, and cell invasion through complex ECM environments [4]. As a major ECM protein possessing binding sites for various types of integrins and as a critical mechanosensor, Fn has been implicated in integrin-mediated pathways that may modulate tumor cell migration, invasion, and apoptotic responses of breast cancer cells [5–7]. However, whether and how Fn-HAP interactions could mediate integrin binding and subsequent cell functions during breast cancer metastasis remain unclear.

During tumor progression, the formation of new blood vessels, a process called angiogenesis, is critical for primary tumor growth and metastasis [8]. Tumor cells promote angiogenesis by up-regulating proangiogenic factors [9]. Dysregulated cell-ECM interactions and integrin signaling have been indicated in the altered signaling of a major proangiogenic factor, vascular endothelial growth factor (VEGF) [10–12]. A proinflammatory factor, interleukin-8 (IL-8), can also promote angiogenic responses in endothelial cells, increase tumor cell survival and proliferation, and potentiate tumor cell migration and invasion. [13–15]. Moreover, IL-8 acts as a mediator of osteolysis due to bone metastasis, and is dramatically up-regulated in breast cancer cells that preferentially metastasize to bone [13,16]. In fact, a strong correlation has been established between IL-8 expression and the metastatic potential of breast cancer cells [17]. Interestingly, a high staining intensity for Fn in tumors has been associated with increased mortality among patients with breast and prostate cancers; moreover, circulating plasma Fn enhances blood vessel formation and facilitates tumor growth by increasing soluble VEGF contents and VEGF-mediated signaling [18]. Thus HAP-mediated alterations of Fn mechanobiology (both mechanosensing and mechanotransduction) may regulate proangiogenic signaling pathways that promote tumor progression and metastasis to bone.

We hypothesized that Fn might act as a functional link for breast cancer cells to sense and respond to materials properties of bone mineral. To test our hypothesis, we utilized the geologic HAP crystal facets described in Chapter 3 instead of HAP nanoparticles so that we could (i) independently control HAP surface chemistry and topography, and (ii) avoid cytotoxicity linked with cell capability of uptaking nanoparticles. Specifically, we sought to understand whether differential Fn adsorption controlled by HAP surface chemistry and topography impacted breast cancer cell functions, in particular cell adhesion, FA assembly, and secretion of VEGF and IL-8. In Chapter 3, our FRET analysis revealed that HAP surface chemistry and topography had individual effects on Fn adsorption: for example, 001S surfaces characterized by low surface charge density and low roughness level would favor unfolded Fn conformations. Here we present cell culture studies that correlate these findings with subsequent altered FA formation and increased proangiogenic and proinflammatory secretion by breast cancer cells when they interact with the unfolded Fn adsorbed onto 001S HAP facets.

## **4.3 Materials and Methods**

### **4.3.1 Cell culture and seeding**

We developed a HAP/Polydimethylsiloxane (HAP/PDMS) system for cell culture studies (**Figure 4.1**). First, HAP facets were embedded inside PDMS slabs and inserted in PDMS sample holders. Next, PDMS wells containing HAP/PDMS slabs were incubated with SuperBlock (Thermo Scientific, IL) for 1 h at room temperature to block nonspecific binding, washed 3 times with DI water, and dried in air. Then, each HAP surface (approximately 5 mm by 7 mm in size, 2 mm in thickness) was exposed by removing the PDMS thin layer that covered

the HAP crystal in the PDMS slab. After sterilizing the HAP/PDMS system with UV lamp for 1 h, HAP surfaces were washed with sterile PBS three times, and a droplet of 50  $\mu$ L of Fn solution (50  $\mu$ g/mL, unlabeled Fn) was incubated on each HAP surface for 24 h at 4  $^{\circ}$ C. For control sample (8-well Lab-Tek chambered borosilicate coverglass, Thermo Fisher Scientific), 130  $\mu$ L Fn solution (50  $\mu$ g/mL, unlabeled Fn) was added per well. After washing 3 times with PBS, these Fn coated surfaces were used for cell culture experiments.

MDA-MB-231 breast cancer cells (ATCC<sup>®</sup> HTB26<sup>™</sup>) were cultured in  $\alpha$ -MEM media supplemented with 10% FBS and 1% P/S at 37  $^{\circ}$ C in 5% CO<sub>2</sub>, with media refreshed every 48 h. At approximately 80% confluency, cells were detached with trypsin-EDTA and used for cell seeding. A droplet of 50  $\mu$ L cell solution containing 12,000 MDA-MB-231 cells was added onto each Fn coated HAP facet (seeding density  $3 \times 10^4$  /cm<sup>2</sup>). After 30 min of cell adhesion, additional 650  $\mu$ L  $\alpha$ -MEM media supplemented with 1% FBS and 1% P/S was added into each well, resulting in a total volume of 700  $\mu$ L media per well. For control sample, 114  $\mu$ L cell solution containing 27, 000 MDA-MB-231 cells were added per well (seeding density  $3 \times 10^4$  /cm<sup>2</sup>); after 30 min, additional 286  $\mu$ L media was added leading to a total volume of 400  $\mu$ L media per well. After culturing at 37  $^{\circ}$ C in 5% CO<sub>2</sub> for either 6 h or 24 h, cell viability and adhesion were analyzed, and culture media were collected for secretion quantification.

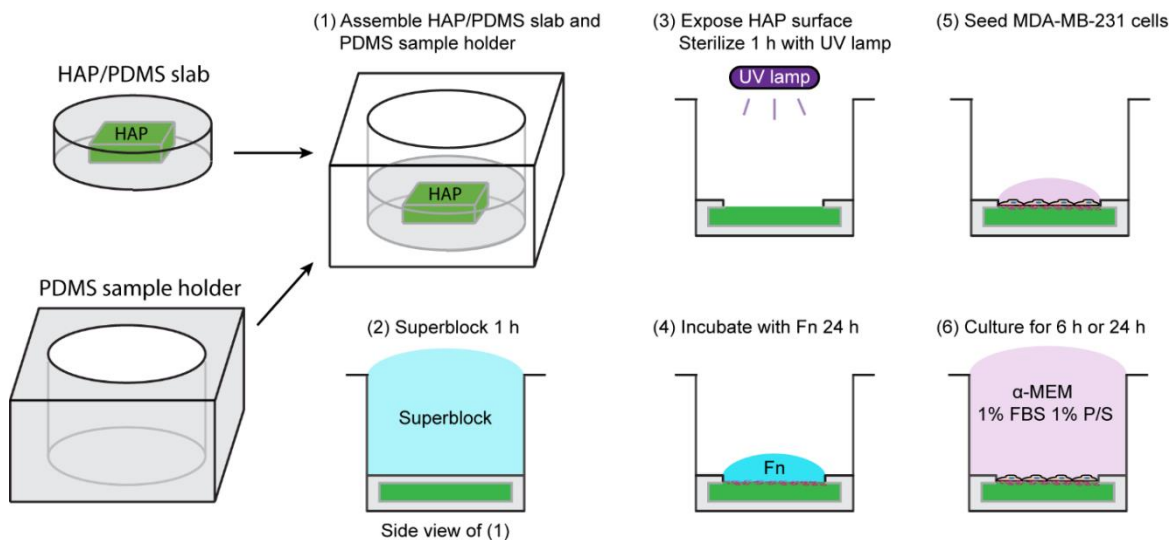


**Figure 4.1** Preparation of HAP/PDMS system for cell culture studies.

#### 4.3.2 Cell viability and adhesion

Cell viability was examined with a LIVE/DEAD® Viability/Cytotoxicity Kit (Molecular Probes, OR) based on the simultaneous determination of live and dead cells with calcein AM and ethidium homodimer (EthD-1), respectively. Nonfluorescent cell-permeant calcein AM converts to intensely green fluorescent calcein, which is membrane impermeable, after cleaved by intracellular esterase in live cells. EthD-1 can only enter damaged membranes of dead cells and produces a bright red fluorescence upon binding to nucleic acids. After collecting culture media, samples were washed once gently with warm PBS, and incubated in Live/Dead working solutions (PBS containing 2  $\mu$ M calcein-AM and 4  $\mu$ M EthD-1) for 30 minutes at 37 °C in 5% CO<sub>2</sub>. Then images were acquired in phenol red free DMEM/F12 media with an epifluorescence microscope (Zeiss, Munich, Germany), using a 2.5x objective. The entire surface area of each HAP facet was imaged and the number of live cells was used to quantify cell adhesion. For

larger control samples, 5 fields of view were acquired to estimate the total number of cells adhered per well.

#### 4.3.3 Immunostaining and confocal imaging

For immunostaining, cells seeded on each HAP facet (embedded in PDMS slabs) were cultured in 800  $\mu\text{L}$   $\alpha$ -MEM with 1% FBS and 1% P/S at 37 °C in 5% CO<sub>2</sub> in 24-well plates. After 24 h, samples were washed three times with 800  $\mu\text{L}$  (200  $\mu\text{L}$  for control) warm PBS and fixed in 50  $\mu\text{L}$  (200  $\mu\text{L}$  for control) 3.7% formalin for 1 hour at 4 °C. To permeabilize cell membranes, samples were washed twice with 50  $\mu\text{L}$  0.05% Triton-X in PBS (PBS-X, Thermo Scientific, 200  $\mu\text{L}$  for control) for 5 min each time, and then blocked for 30 min at room temperature with 50  $\mu\text{L}$  (200  $\mu\text{L}$  for control) PBS-X/1% SuperBlock (Thermo Scientific). To immunostain for vinculin, samples were incubated with 50  $\mu\text{L}$  primary mouse anti-vinculin antibodies (1:1000, clone VIN115, Sigma-Aldrich) in PBS/1%SuperBlock (125  $\mu\text{L}$  for control) at 4 °C overnight. Samples were then washed twice with 50  $\mu\text{L}$  PBS-X (200  $\mu\text{L}$  for control) for 5 min each time, and incubated with 50  $\mu\text{L}$  (200  $\mu\text{L}$  for control) goat anti-mouse IgG1 ( $\gamma$ 1), CF<sup>TM</sup>555 secondary antibodies (1:1000, Sigma-Aldrich) and DAPI (1:1000, Life Technologies) in PBS/1%SuperBlock at room temperature for 1 hr. Finally samples were washed twice with 50  $\mu\text{L}$  PBS (200  $\mu\text{L}$  for control) for 5 min each time and kept in PBS at 4 °C until imaging.

Z-stack images were acquired with a Zeiss LSM880 inverted confocal microscope (Zeiss, Munich, Germany) using a C-Achroplan water-immersion 32x/0.85 objective, zoom-in 1.3x, a pinhole of 2AU (2  $\mu\text{m}$  section), and a z step size of 1  $\mu\text{m}$ . DAPI was excited with a 405 nm laser set at 5% laser power, and CF<sup>TM</sup>555 was excited with a 561 nm laser set at 5% laser power. For nuclei counting, a Fluar 5x/0.25 M27 objective was used, and tiling images were acquired with

10% overlap between adjacent images. All immunofluorescence images were analyzed in ImageJ (NIH).

#### 4.3.4 VEGF and IL-8 secretion

The media collected after culturing for 6 h or 24 h were centrifuged for 15 min at 13500 rpm and supernatants free of cell debris were utilized to quantify VEGF and IL-8 contents with commercial VEGF and IL-8 ELISA kits (Life Technologies). The media collected at 6 h time point were concentrated 6 fold with 10K centrifugal filter devices (Amicon® Ultra, 10,000 NMWL) for measuring VEGF, or 3 fold with 3K centrifugal filter devices (Amicon® Ultra, 3,000 NMWL) for measuring IL-8. The media collected at 24 h time point were used without further concentrating for measurement. VEGF and IL-8 amounts were normalized by the number of live cells for each corresponding sample.

#### 4.3.5 HAP facets cleaning

After each experiment, cells were removed from HAP facets by washing three times with PBS and then incubating in 0.5% trypsin in PBS at 37 °C for 30 min. After washing three times with PBS, remaining cell residues were cleaned by cell scrapers. HAP facets were then immersed in PBS containing 5% sodium dodecyl sulfate (SDS) overnight, sonicated in 0.1 M NaOH, and rinsed with DI water and ethanol.

#### 4.3.6 Statistical analysis

One-way ANOVA with Tukey's post test and Student's t-test were used to determine statistical significance between conditions in GraphPad Prism (GraphPad Software, Inc., CA). In all cases,  $p < 0.05$  is indicated by a single star,  $p < 0.01$  by two stars and  $p < 0.001$  by three stars.

## 4.4 Results

### 4.4.1 Breast cancer cell viability

To determine whether HAP surface chemistry and topography affect breast cancer cell functions via Fn mediated interactions, we seeded MDA-MB-231 human breast cancer cells onto Fn coated HAP facets with controlled chemistry and topography. MDA-MB-231 cells were chosen because these cells are known to be highly invasive both *in vitro* and relatively poorly invasive *in vivo* [19]. First we examined the viability and adhesion of breast cancer cells via Live/Dead assay. The entire HAP surface was imaged to count the number of live (green) and dead (red) cells for each sample (**Figure 4.2**). Results show that on average 95% cells were alive on all five samples including control up to 24 h after initial cell seeding (**Figure 4.3**). Average cell viability decreased to circa 75% after 48 h on smooth facets, but remained circa 95% on rough facets (data not shown), suggesting that tumor cell viability is dependent on underlying Fn conformation and deposition. We chose the 6 h and 24 h time points for subsequent adhesion and secretion experiments to avoid the complexity of interpreting results due to cell apoptosis.

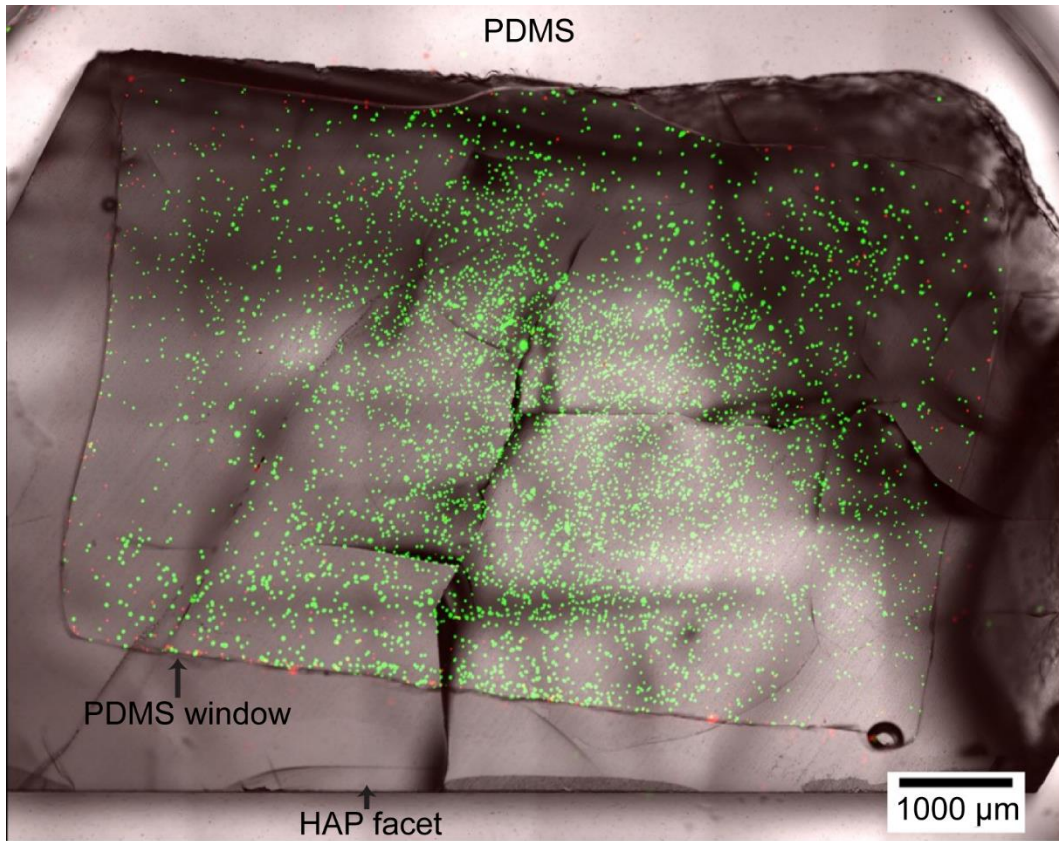


**Figure 4.2** Merged fluorescence image acquired for Live/Dead assay. Live cells were stained in green and dead cells were stained in red.

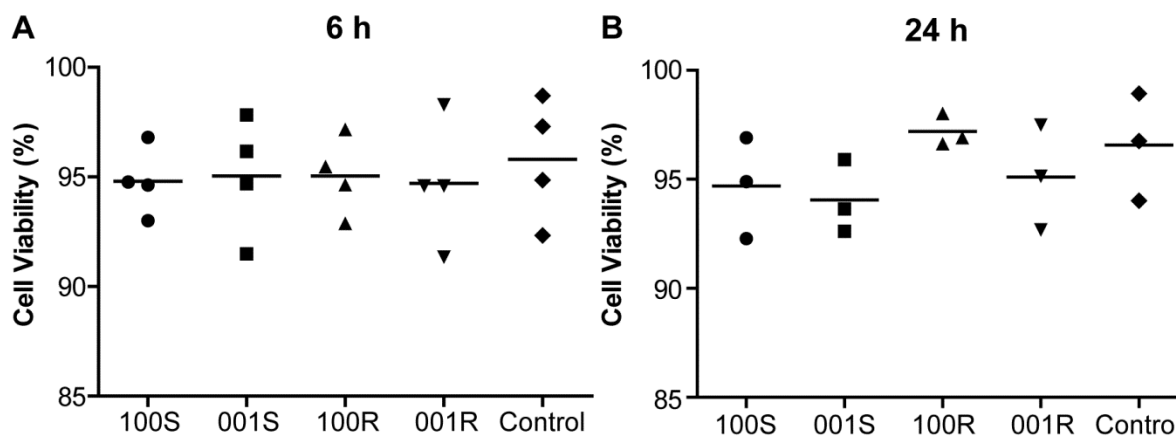


**Figure 4.3** MDA-MB-231 breast cancer cell viability after seeding for either (A) 6 h or (B) 24 h on Fn coated HAP facets and control coverglass, as quantified via Live/Dead assay. N = 4 for 6 h, N = 3 for 24 h.

#### 4.4.2 Breast cancer cell adhesion

The number of live cells were also used to quantify cell adhesion as a function of HAP surface properties. More cells tended to adhere on rougher facets, although no statistical significance was detected between (100) vs. (001) facets or between smooth vs. rough facets (**Figure 4.4**). Overall fewer cells adhered onto HAP facets after 24 h than after 6 h. However, it should be noted that cells used for the 6 h experiments were at passage 36 ~ 40, while those used for the 24 h experiments were at passage 4 ~ 8, which may cause variability in cell adhesion when comparing 6 h with 24 h results.

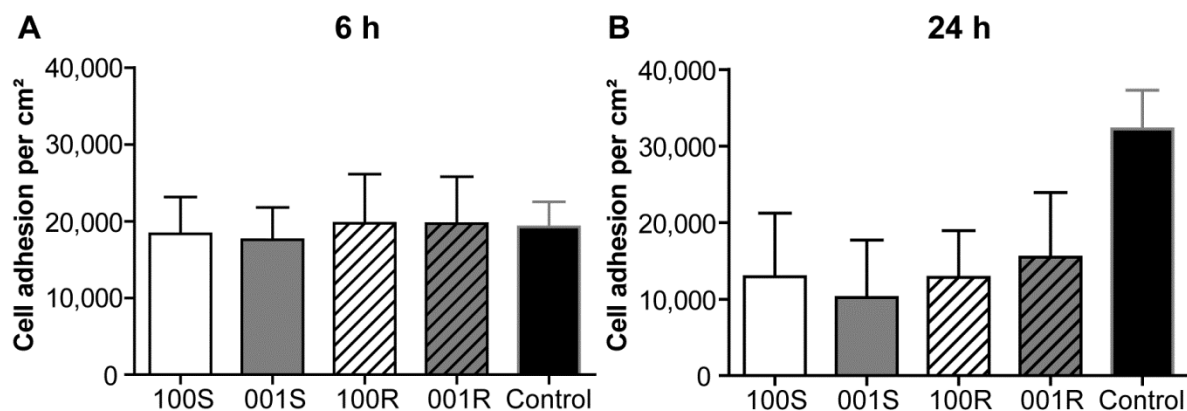


**Figure 4.4** MDA-MB-231 breast cancer cell adhesion after initial seeding for either (A) 6 h or (B) 24 h on Fn coated HAP facets and control coverglass, as quantified by the number of live cells via Live/Dead assay. Mean  $\pm$  SD. N = 5 for 6 h, and N = 4 for 24 h.

#### 4.4.3 Focal adhesion formation

To investigate whether the assembly of FAs depends on underlying Fn layer and HAP surface properties, cells were stained for nuclei and FAs were identified by immunofluorescence staining of vinculin. Confocal fluorescence images were analyzed to determine FA features. Representative immunofluorescence images show that, in addition to vinculin localized in well-defined FA plaques at the cell membrane-ECM interface, considerable amounts of vinculin were also present within the central regions of cell cytoplasm, i.e., not associated with FAs (**Figure 4.5**). These cytoplasm vinculin signals were excluded in our FA feature analysis.

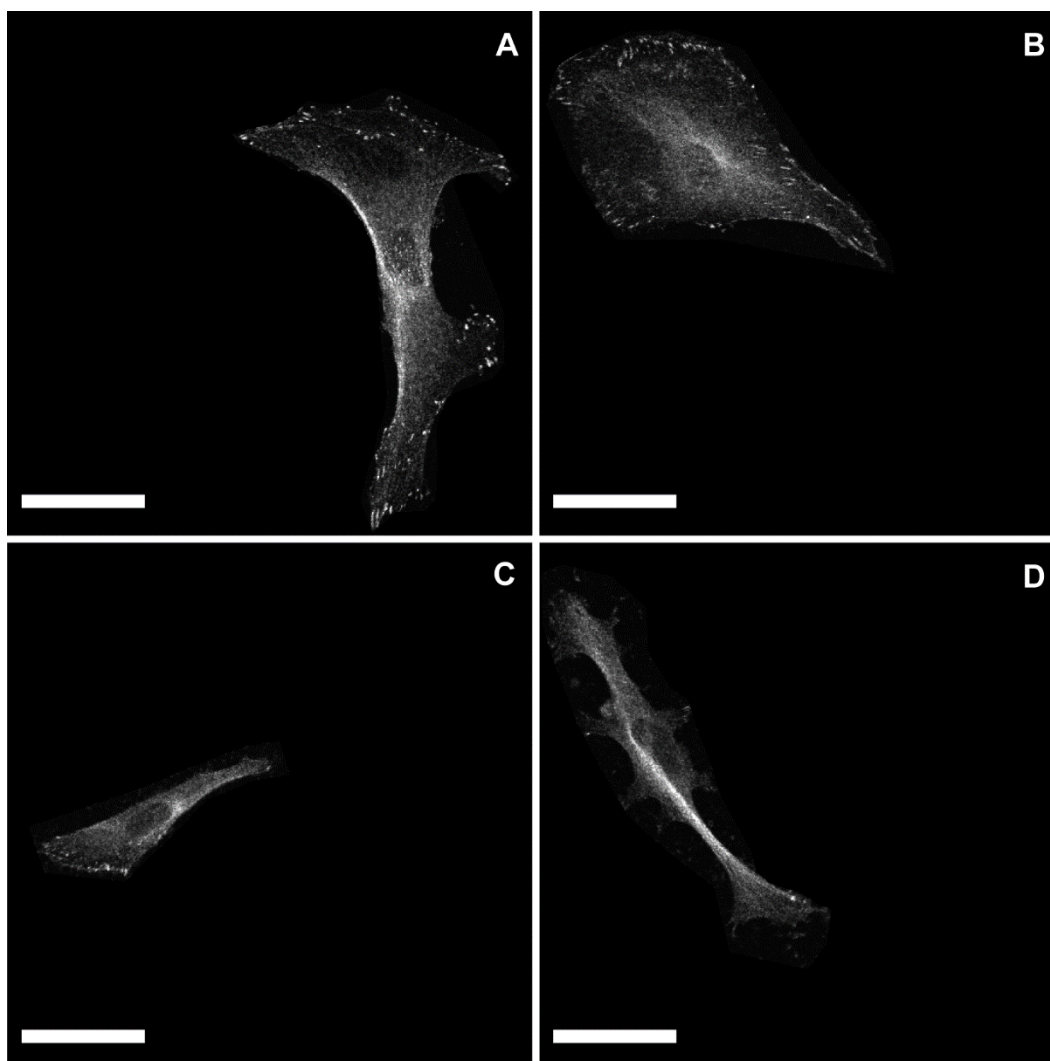


**Figure 4.5** Representative confocal images of immunostained vinculin in MDA-MB-231 cells seeded on Fn coated (A) (100)S, (B) (001)S, (C) (100)R, and (D) (001)R HAP facets, after 24 h in culture. Scale bars 50  $\mu\text{m}$ .

Our FA feature analysis results are summarized in **Figure 4.6**. Both the number (per cell) and the size of FAs depended on HAP surface chemistry and topography. According to the distribution histograms shown in **Figure 4.7**, HAP surface chemistry influenced the area of FAs by increasing the length of FAs (larger fraction of longer FAs on (001)), while HAP surface roughness seemed to affect the area of FAs by increasing the width of FA plaques (larger

fraction of wider FAs on rough facets). Both the number of FAs per cell (although not significantly different) and their area were larger on 001S than on 100S. When comparing 100-oriented smooth and rough facets, we observed similar numbers of FAs that were significantly larger on 100R than on 100S, which could be associated with higher levels of compact Fn molecules adsorbed onto 100R. (Chapter 3, **Figure 3.7**). However, although higher levels of compact Fn molecules were also detected on 001R than on 001S, FAs number per cell was smaller on 001R than on 001S, while FA area was similar on both facets.

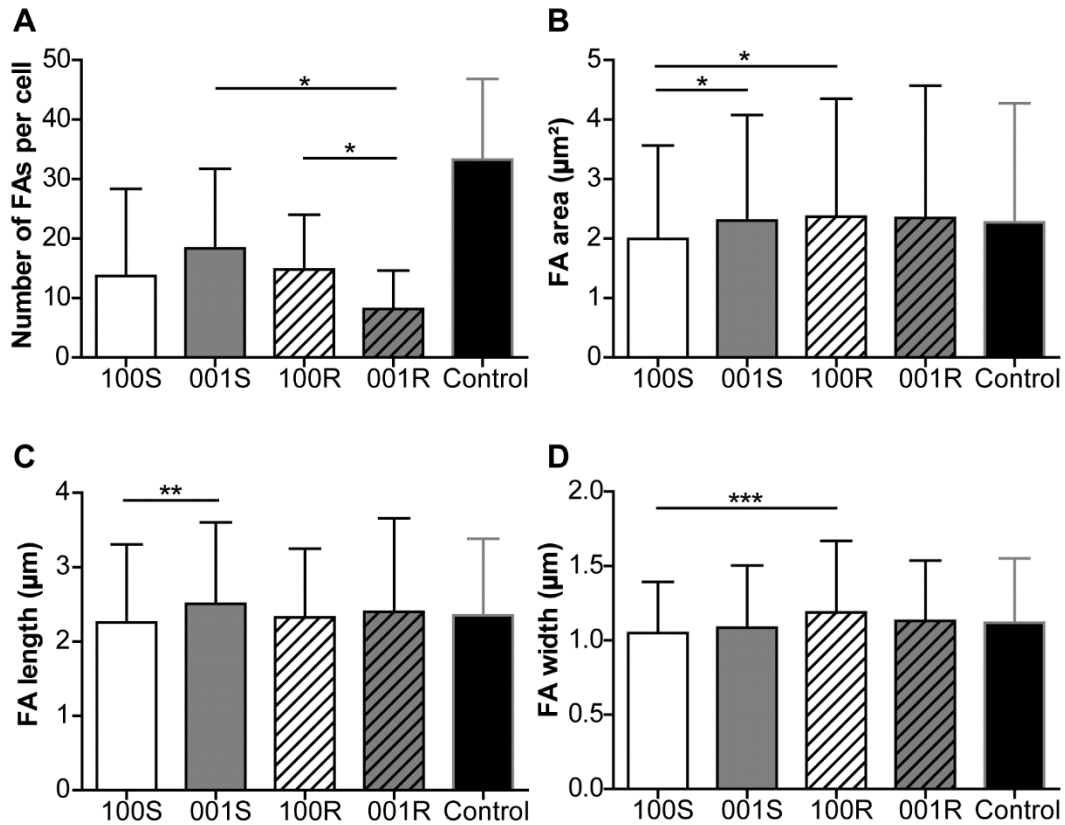


**Figure 4.6** Focal adhesion (FA) analysis of MDA-MB-231 cells on Fn coated HAP facets after culturing for 24 h: (A) the number of FAs formed per cell, (B) FA area, (C) FA length, and (D) FA width. FA area, length, and width were obtained by fitting ellipse for each FA (ImageJ).

Vinculin was immunostained for visualizing FAs. Number of cells analyzed: N = 20, 17, 18, 14 and 14 for 100S, 001S, 100R, 001R, and control, respectively. Number of FAs analyzed: n = 274, 312, 267, 114, and 466, for 100S, 001S, 100R, 001R, and control, respectively. In all cases,  $p < 0.05$  is indicated by a single asterisk,  $p < 0.01$  by two asterisks, and  $p < 0.001$  by three asterisks. Mean  $\pm$  SD.

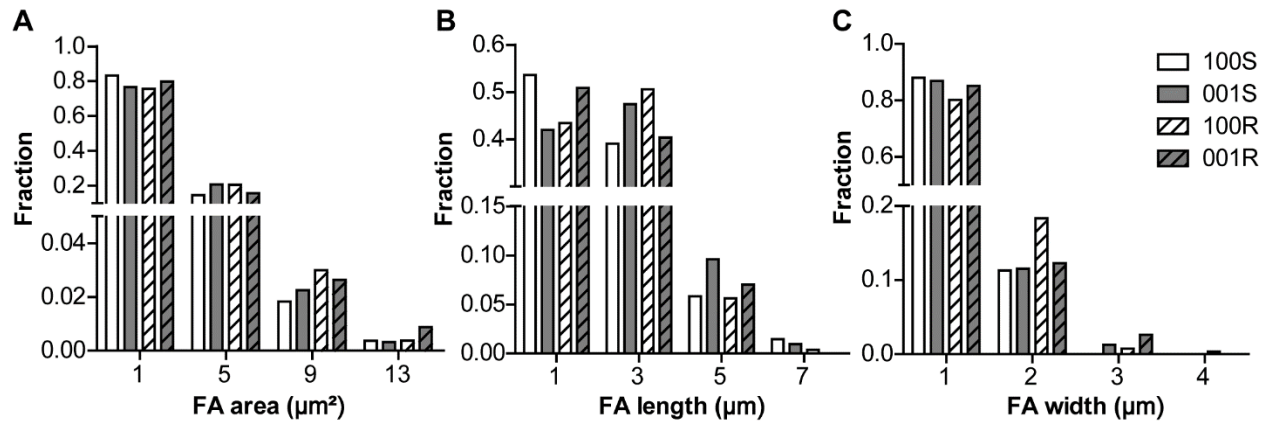


**Figure 4.7** Frequency distributions of (A) FA area, (B) FA length, and (C) FA width in MDA-MB-231 cells seeded on Fn coated HAP facets, after 24 h in culture.

#### 4.4.4 VEGF secretion

We then evaluated the proangiogenic capability of MDA-MB-231 cells via quantification of VEGF secretion. To assess secretion per cell, all our data (VEGF and IL-8 levels) were normalized by the number of live cells for each sample. After 6 h, VEGF secretion by tumor cells tended to be higher on smooth than on rough facets, independently of crystal orientation (**Figure 4.8A**). After 24 h, VEGF levels were not only significantly higher on smooth than on rough 001-oriented surfaces but they also tended to be higher on 001S than 100S, indicating a

likely dependence on surface chemistry too (**Figure 4.8B**). In addition, the quantity of secreted VEGF drastically increased from 6 h to 24 h for all samples, especially for HAP surfaces. After 6 h, VEGF level on HAP surfaces was similar to that of control; whereas after 24 h, it was equivalent to 4 ~ 6 times that of control. Together with our cell adhesion results, these data indicate that tumor cells seeded on HAP surfaces exhibit slower proliferation but much more active proangiogenic capability than those seeded on control coverglass, although both Fn conformation and quantity adsorbed were similar for control and rough HAP surfaces (Chapter 3, **Figure 3.7**).

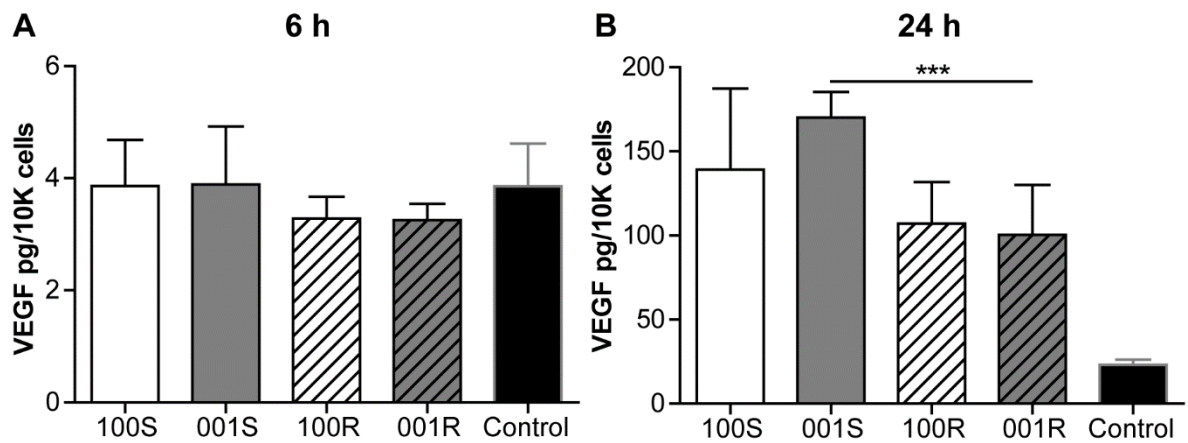


**Figure 4.8** VEGF secretion by MDA-MB-231 breast cancer cells as analyzed via ELISA assay of media collected either (A) 6 h or (B) 24 h after initial seeding on Fn coated HAP facets and control coverglass. Values were normalized by the number of live cells adhered. In all cases,  $p < 0.05$  is indicated by a single asterisk,  $p < 0.01$  by two asterisks, and  $p < 0.001$  by three asterisks. Mean  $\pm$  SD.

#### 4.4.5 IL-8 secretion

We also evaluated the proinflammatory and osteolytic capability of MDA-MB-231 cells via quantification of IL-8 secretion. IL-8 secretion followed a similar trend as VEGF secretion, with lower IL-8 levels secreted by tumor cells on rougher facets (**Figure 4.9**). Moreover, after 24 h, significantly higher levels of IL-8 were measured on 001S than on 100S, suggesting that surface chemistry plays an important role in differential IL-8 secretion by tumor cells when HAP surfaces are smooth. This surface chemistry effect was not observed when comparing 100R with 001R, probably due to the chemical heterogeneity of rough facets. Additionally, IL-8 secretion increased drastically from 6 h to 24 h for all samples, especially for HAP surfaces. Moreover, the overall quantity of IL-8 secreted by tumor cells was much higher than that of VEGF (circa four times that of VEGF at 24 h).

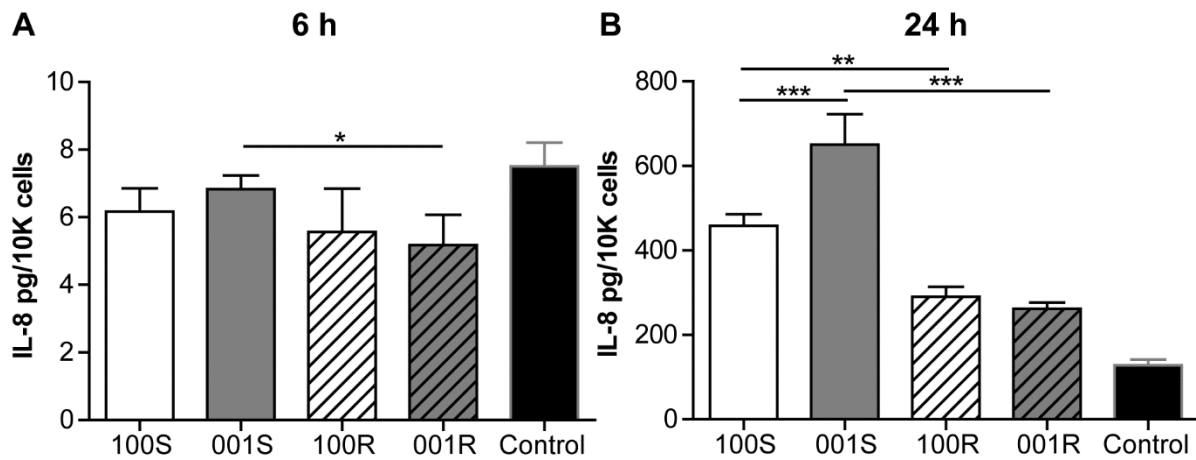


**Figure 4.9** IL-8 secretion by MDA-MB-231 breast cancer cells as analyzed via ELISA assay of media collected (A) 6 h and (B) 24 h after initial seeding on Fn coated HAP facets and control coverglass. Values were normalized by the number of live cells adhered. In all cases,  $p < 0.05$  is indicated by a single asterisk,  $p < 0.01$  by two asterisks, and  $p < 0.001$  by three asterisks. Mean  $\pm$  SD.

Collectively, our results reveal that, although the number of live cells was similar on all HAP samples, the number and size of FAs developed by cells varied as a function of HAP surface properties (mediating adsorbed Fn amounts and conformations). Additionally, tumor cells appeared to be (i) sensitive to HAP roughness to regulate both their VEGF and IL-8 secretion levels and (ii) reactive to HAP surface chemistry to control their IL-8 secretion, in particular when interacting with smooth HAP surfaces.

## 4.5 Discussion

First we investigated whether cell adhesion is regulated by Fn conformation and deposition onto HAP surfaces. Surprisingly, the number of breast cancer cells adhered was independent on underlying Fn conformation, although there were slightly more cells present on rougher HAP facets, probably due to larger amounts of Fn adsorbed associated with increased ligand density (**Figure 4.4**) [20]. Cells typically express multiple types of integrin receptors and some receptors share the same ligand with different affinities. Fn conformational changes can significantly affect the spatial arrangement and accessibility of its binding sites for integrins. In the case of two predominant receptors involved in binding ECM molecules with RGD domains:  $\alpha_5\beta_1$  integrins require the close vicinity of the RGD domain on Fn-III<sub>10</sub> and the synergy PHSRN site on Fn-III<sub>9</sub> for engagement and activation, while  $\alpha_v\beta_3$  integrin only requires the RGD loop [21]. In addition, activation state of  $\alpha_5\beta_1$  also affect its binding affinity for Fn [22,23]. Therefore, cells can utilize  $\alpha_v\beta_3$  integrins but not  $\alpha_5\beta_1$  integrins to bind to extended/unfolded Fn when the spatial arrangement (relative angles and distance) between RGD loop and synergy site is disrupted [24].

Nevertheless, previous work has demonstrated that MDA-MB-231 cell adhesion onto Fn coated 2D surfaces actually increased modestly after depletion of either  $\beta_1$  or  $\beta_3$  integrins, suggesting that each integrin can compensate for the loss of the other in ligand-binding [4]. Thus, our observation that MDA-MB-231 cell adhesion (or rather live cells number per sample) is not sensitive to Fn conformation may be explained by the high level of expression of either  $\beta_1$  or  $\beta_3$  integrins in these cells that can compensate for each other when binding to Fn in a variety of conformations. This differential engagement of integrins with Fn likely propagates downstream and triggers altered intracellular signaling cascades that subsequently regulate secretion among other cell functions.

Although live cell numbers were similar on all four types of HAP facets, both the number of FAs per cell and FA size were affected by HAP surface chemistry and roughness. On smooth facets with homogeneous surface chemistry, cancer cells formed a higher number of larger FAs when seeded on 001S with respect to 100S. The 001S facet is coated by small amounts of mostly unfolded Fn (Chapter 3, **Figure 3.7**), which seems to be the best substrate to promote FA formation. This effect may be attributed to both loss of active binding sites and exposure of cryptic binding sites when Fn unfolds. The exposure of the Fn synergy site has been shown to trigger different FA assemblies in fibroblasts [25]. Moreover, surface charge of a substrate may also affect the availability of Fn binding sites, such as the RGD/synergy site for  $\alpha_5\beta_1$  integrin, and phosphorylation of focal adhesion kinase via electrostatic interactions [26]. The availability of Fn binding sites probably affects FA formation through differential integrin engagement. Previous work shows that loss of  $\beta_1$  but not  $\beta_3$  integrins in MDA-MB-231 cells leads to increased spread cell area and FA number in cells as well as decreased cell migration on Fn functionalized

2D substrates [4]. Thus the integrin switch from  $\beta_1$  to  $\beta_3$  integrin may explain the enhanced FA formation in cells adhered on extended/unfolded Fn adsorbed onto (001)S.

However, on rough facets with heterogeneous surface chemistry, the number of FAs per cell was larger on 100R than on 001R. Additionally, increasing roughness led to larger FA area formed on (100) facets, but not on (001) facets. Moreover, the number of FAs per cell decreased on 001R as compared with on 001S. Thus surface roughness introduced additional complexity in regulating FA assembly. These results suggest that effects of surface chemistry and roughness may cooperatively regulate both availability (Fn conformation) and surface density (Fn quantity) of ligands, leading to differential FA formation on these surfaces. It is likely that the total FA area per cell is the key parameter that indicates cell adhesion strength. On 001S, where Fn was unfolded and the synergy site might not be accessible, cells upregulated both the number of FAs per cell and FA area to engage efficiently with the underlying surface.

The differential engagement of integrins with Fn may also explain the higher level of VEGF secretion by breast cancer cells when interacting with smooth rather than rough HAP facets (**Figure 4.8**). We propose that the more extended/unfolded Fn adsorbed on smooth facets could enhance VEGF secretion as cells utilize  $\alpha_v\beta_3$  integrin to compensate for  $\alpha_5\beta_1$ . On rough facets coated with compact Fn, cells may predominantly engage with Fn via  $\alpha_5\beta_1$  integrin; while on smooth facets coated with unfolded Fn, the disrupted RGD/synergy binding site disables  $\alpha_5\beta_1$  binding and favors  $\alpha_v\beta_3$  binding. In fact, higher engagement of  $\alpha_v\beta_3$  has been shown to increase VEGF secretion in many types of cells [10,11,27]. Although a clear trend is visible, this functional difference is not significant when comparing (100) with (001) smooth HAP, possibly due to the differential sequestration of VEGF within the Fn layer. Additionally, the heterogeneity of the integrin expressing level in MDA-MB-231 population should be noted, with 25~50% of

the population expressing  $\alpha_v\beta_3$  integrins [28]. These results suggest that VEGF secretion by MDA-MB-231 cells is more sensitive to differential Fn adsorption induced by HAP surface topography than by surface chemistry.

IL-8 secretion follows the same general trend as VEGF secretion, but seems to be more sensitive to Fn conformational changes induced by HAP surface chemistry (**Figure 4.9**). The highest level of IL-8 secretion was measured on 001S, which is associated with the lowest FRET intensity detected, i.e. the smallest amounts of most extended/unfolded Fn conformations. These results suggest that the up-regulated IL-8 secretion can also be attributed to varied integrin engagement with Fn, which agrees with previous studies [12,13]. The observation that VEGF secretion is not as dramatically affected as IL-8 secretion by the microenvironment cues, in particular integrin engagement, has also been observed in other 2D and 3D culture platforms [12]. Together, the up-regulation of IL-8 and VEGF, and their interplay, is likely critical in promoting tumorigenesis through increased angiogenesis and in facilitating bone metastasis through enhanced osteolysis.

Our results indicate that crucial breast cancer cell functions such as adhesion and proangiogenic/proinflammatory secretion are mediated by the conformation and deposition of Fn films imposed by HAP surface properties, probably via differential integrin engagement. More specifically, fewer amounts of more extended/unfolded conformations of Fn were associated with enhanced FA assembly and elevated VEGF and IL-8 secretion levels by breast cancer cells. Thus HAP surface properties may contribute to breast cancer adhesion and angiogenesis through Fn-integrin engagement mediated pathways. The importance of integrins in mediating tumor progression makes them targets for cancer therapy, and some integrin antagonists have been tested in clinical trials with promising results [29]. It should be noted that the Fn conformation

and deposition may be remodeled by cancer cells after initial cell seeding, especially at the 24 h time point, thus our FRET results in Chapter 3 is only relevant when interpreting initial cell responses to the underlying Fn layer. Additionally, cellular behaviors in 2D culture platforms can be very different from those in 3D compliant scaffolds, although the rough facets present 3D surface features [4,12,30]. Nevertheless, the simplicity of 2D culture platforms allows the capability to separate effects of surface chemistry and topography in how HAP materials properties affect Fn-mediated breast cancer cell functions and provide important implications for our understanding of bone metastasis. In future work, the use of 3D scaffolds and biologic apatite will provide better implications for *in vivo* responses of breast cancer cells. The mechanism of integrin-mediated FA assembly and secretion proposed above can be validated by immunostaining or blocking specific integrins, such as  $\alpha_5\beta_1$  and  $\alpha_v\beta_3$ .

## 4.6 Conclusions

In this chapter, we utilized the Fn coated geologic HAP facets characterized in Chapter 3 as cell culture platforms to demonstrate that HAP surface chemistry and topography have both individual and combined effects on Fn-mediated breast cancer cell functions, in particular FA assembly and proangiogenic/proinflammatory capability. Specifically, 100S facets with high density of surface charges favor high amounts of adsorbed Fn at the HAP surface, adopting overall compact conformations that result in low levels of VEGF and IL-8 secretion per cell. In contrast, more hydrophobic 001S facets (with low density of surface charges) lead to lower amounts of adsorbed Fn at the HAP surface, adopting overall extended/unfolded conformations.

Such unfolded Fn coating provides the most favorable platform for FA development (more FAs per cell and larger FA sizes) and triggers the highest levels of VEGF and IL-8 secretions by breast cancer cells among all four types of HAP facets, suggesting that altered integrin specificity may underlie these secretion changes. Additionally, increasing surface roughness promotes Fn adsorption in more compact conformation and decreases levels of VEGF and IL-8 secretion, which is consistent with less VEGF and IL-8 secreted on 100S than on 001S. However, increasing surface roughness has different effects on FA assembly in cells seeded on (100) and (001) facets: while larger FA sizes were measured on 100R than on 100S, fewer FAs per cell were observed on 001R than on 001S. The complicated effect of surface roughness may be due to changes not only in Fn conformation (ligand availability) but also in Fn quantity (ligand density). Additionally, the topography itself may be another important factor in regulating cell behaviors [31–34]. These findings can help us better understand the role of mineral/ECM interface in regulating breast cancer bone metastasis.

## REFERENCES

- [1] F.G. Giancotti, E. Ruoslahti, Integrin Signaling, *Science*. 285 (1999) 1028–1032. doi:10.1126/science.285.5430.1028.
- [2] L.B. Case, M.A. Baird, G. Shtengel, S.L. Campbell, H.F. Hess, M.W. Davidson, et al., Molecular mechanism of vinculin activation and nano-scale spatial organization in focal adhesions, *Nat. Cell Biol.* 17 (2015) 880–892. doi:10.1038/ncb3180.
- [3] R. Rathinam, S.K. Alahari, Important role of integrins in the cancer biology, *Cancer Metastasis Rev.* 29 (2010) 223–237. doi:10.1007/s10555-010-9211-x.
- [4] P. Costa, T.M.E. Scales, J. Ivaska, M. Parsons, Integrin-Specific Control of Focal Adhesion Kinase and RhoA Regulates Membrane Protrusion and Invasion, *PLoS One*. 8 (2013). doi:10.1371/journal.pone.0074659.
- [5] G. Maity, P.R. Choudhury, T. Sen, K.K. Ganguly, H. Sil, A. Chatterjee, Culture of human breast cancer cell line (MDA-MB-231) on fibronectin-coated surface induces pro-matrix metalloproteinase-9 expression and activity, *Tumor Biol.* 32 (2011) 129–138. doi:10.1007/s13277-010-0106-9.
- [6] F. Aoudjit, K. Vuori, Integrin signaling inhibits paclitaxel-induced apoptosis in breast cancer cells., *Oncogene*. 20 (2001) 4995–5004. doi:10.1038/sj.onc.1204554.
- [7] R. Korah, M. Boots, R. Wieder, Integrin alpha5beta1 promotes survival of growth-arrested breast cancer cells: an in vitro paradigm for breast cancer dormancy in bone marrow., *Cancer Res.* 64 (2004) 4514–4522. doi:10.1158/0008-5472.CAN-03-3853.
- [8] G. Neufeld, T. Cohen, S. Gengrinovitch, Z. Poltorak, Vascular endothelial growth factor (VEGF) and its receptors., *FASEB J.* 13 (1999) 9–22. doi:10.1210/Er.2003-0027.
- [9] D. Hanahan, R.A. Weinberg, The hallmarks of cancer, *Cell*. 100 (2000) 57–70. doi:10.1007/s00262-010-0968-0.
- [10] S. De, O. Razorenova, N.P. McCabe, T. O’Toole, J. Qin, T. V Byzova, VEGF-integrin interplay controls tumor growth and vascularization., *Proc. Natl. Acad. Sci. U. S. A.* 102 (2005) 7589–7594. doi:10.1073/pnas.0502935102.

- [11] K. Wang, R.C. Andresen Eguiluz, F. Wu, B.R. Seo, C. Fischbach, D. Gourdon, Stiffening and unfolding of early deposited-fibronectin increase proangiogenic factor secretion by breast cancer-associated stromal cells, *Biomaterials*. 54 (2015) 63–71. doi:10.1016/j.biomaterials.2015.03.019.
- [12] C. Fischbach, H.J. Kong, S.X. Hsiong, M.B. Evangelista, W. Yuen, D.J. Mooney, Cancer cell angiogenic capability is regulated by 3D culture and integrin engagement., *Proc. Natl. Acad. Sci. U. S. A.* 106 (2009) 399–404. doi:10.1073/pnas.0808932106.
- [13] S.P. Pathi, C. Kowalczewski, R. Tadipatri, C. Fischbach, A novel 3-D mineralized tumor model to study breast cancer bone metastasis., *PLoS One*. 5 (2010) e8849. doi:10.1371/journal.pone.0008849.
- [14] Y. Lin, R. Huang, L. Chen, S. Li, Q. Shi, C. Jordan, et al., Identification of interleukin-8 as estrogen receptor-regulated factor involved in breast cancer invasion and angiogenesis by protein arrays, *Int. J. Cancer*. 109 (2004) 507–515. doi:10.1002/ijc.11724.
- [15] K. Xie, Interleukin-8 and human cancer biology., *Cytokine Growth Factor Rev.* 12 (2001) 375–391. doi:10.1016/S1359-6101(01)00016-8.
- [16] M.S. Bendre, D.C. Montague, T. Peery, N.S. Akel, D. Gaddy, L.J. Suva, Interleukin-8 stimulation of osteoclastogenesis and bone resorption is a mechanism for the increased osteolysis of metastatic bone disease, *Bone*. 33 (2003) 28–37. doi:10.1016/S8756-3282(03)00086-3.
- [17] J.E. De Larco, B.R. Wuertz, K.A. Rosner, S.A. Erickson, D.E. Gamache, J.C. Manivel, et al., A potential role for interleukin-8 in the metastatic phenotype of breast carcinoma cells., *Am. J. Pathol.* 158 (2001) 639–646. doi:10.1016/S0002-9440(10)64005-9.
- [18] A. von Au, M. Vasel, S. Kraft, C. Sens, N. Hackl, A. Marx, et al., Circulating Fibronectin Controls Tumor Growth, *Neoplasia*. 15 (2013) 925–IN24. doi:10.1593/neo.13762.
- [19] M. Lacroix, G. Leclercq, Relevance of breast cancer cell lines as models for breast tumours: An update, *Breast Cancer Res. Treat.* 83 (2004) 249–289. doi:10.1023/B:BREA.0000014042.54925.cc.
- [20] M.H. Lee, P. Ducheyne, L. Lynch, D. Boettiger, R.J. Composto, Effect of biomaterial surface properties on fibronectin- $\alpha 5\beta 1$  integrin interaction and cellular attachment., *Biomaterials*. 27 (2006) 1907–16. doi:10.1016/j.biomaterials.2005.11.003.

- [21] A. Krammer, D. Craig, W.E. Thomas, K. Schulten, V. Vogel, A structural model for force regulated integrin binding to fibronectin's RGD-synergy site, *Matrix Biol.* 21 (2002) 139–147. doi:10.1016/S0945-053X(01)00197-4.
- [22] A.J. Garcia, J.E. Schwarzbauer, D. Boettiger, Distinct activation states of  $\alpha 5\beta 1$  integrin show differential binding to RGD and synergy domains of fibronectin, *Biochemistry.* 41 (2002) 9063–9069. doi:10.1021/bi025752f.
- [23] F. Li, S.D. Redick, H.P. Erickson, V.T. Moy, Force measurements of the  $\alpha 5\beta 1$  integrin-fibronectin interaction., *Biophys. J.* 84 (2003) 1252–62. doi:10.1016/S0006-3495(03)74940-6.
- [24] T.A. Petrie, J.R. Capadona, C.D. Reyes, A.J. García, Integrin specificity and enhanced cellular activities associated with surfaces presenting a recombinant fibronectin fragment compared to RGD supports, *Biomaterials.* 27 (2006) 5459–5470. doi:10.1016/j.biomaterials.2006.06.027.
- [25] F.A. Vanterpool, M. Cantini, F.P. Seib, M. Salmerón-Sánchez, A Material-Based Platform to Modulate Fibronectin Activity and Focal Adhesion Assembly., *Biores. Open Access.* 3 (2014) 286–296. doi:10.1089/biores.2014.0033.
- [26] T. Miller, D. Boettiger, Control of Intracellular Signaling by Modulation of Fibronectin Conformation at the Cell - Materials Interface, *Langmuir.* 19 (2003) 1723–1729.
- [27] A.M.D. Wan, E.M. Chandler, M. Madhavan, D.W. Infanger, C.K. Ober, D. Gourdon, et al., Fibronectin conformation regulates the proangiogenic capability of tumor-associated adipogenic stromal cells., *Biochim. Biophys. Acta.* 1830 (2013) 4314–20. doi:10.1016/j.bbagen.2013.03.033.
- [28] N.C. Wong, B.M. Mueller, C.F. Barbas, P. Ruminiski, V. Quaranta, E.C.K. Lin, et al.,  $\alpha v$  Integrins mediate adhesion and migration of breast carcinoma cell lines, *Clin. Exp. Metastasis.* 16 (1998) 50–61.
- [29] J.S. Desgrosellier, D.A. Cheresh, Integrins in cancer: biological implications and therapeutic opportunities, *Nat. Rev. Cancer.* 10 (2010) 9–22. doi:10.1038/nrc2748\rnrc2748.
- [30] M.M. Martino, M. Mochizuki, D.A. Rothenfluh, S.A. Rempel, J.A. Hubbell, T.H. Barker, Controlling integrin specificity and stem cell differentiation in 2D and 3D environments through regulation of fibronectin domain stability., *Biomaterials.* 30 (2009) 1089–97.

doi:10.1016/j.biomaterials.2008.10.047.

- [31] S. Choi, S. Coonrod, L. Estroff, C. Fischbach, Chemical and physical properties of carbonated hydroxyapatite affect breast cancer cell behavior, *Acta Biomater.* 24 (2015) 333–342. doi:10.1016/j.actbio.2015.06.001.
  
- [32] M.T. Frey, I.Y. Tsai, T.P. Russell, S.K. Hanks, Y.-L. Wang, Cellular responses to substrate topography: role of myosin II and focal adhesion kinase., *Biophys. J.* 90 (2006) 3774–3782. doi:10.1529/biophysj.105.074526.
  
- [33] D. Geblinger, L. Addadi, B. Geiger, Nano-topography sensing by osteoclasts., *J. Cell Sci.* 123 (2010) 1503–1510. doi:10.1242/jcs.060954.
  
- [34] L. Chou, J.D. Firth, V.J. Uitto, D.M. Brunette, Substratum surface topography alters cell shape and regulates fibronectin mRNA level, mRNA stability, secretion and assembly in human fibroblasts., *J. Cell Sci.* 108 ( Pt 4 (1995) 1563–73. <http://www.ncbi.nlm.nih.gov/pubmed/7615675>.

## **Chapter 5.**

# **Osteoblast-like Cell Functions on Fibronectin-coated Geologic Apatite Crystal Facets**

Contributors: Weisi Chen, Nicole Marroquin, Lara Estroff, and Delphine Gourdon.

### **5.1 Abstract**

Geologic hydroxyapatite (HAP) facets with controlled surface chemistry (or crystallographic orientation) and topography/roughness were functionalized with physisorbed fibronectin (Fn) and seeded with MC3T3-E1 pre-osteoblasts to investigate their early stage adhesion and focal adhesion (FA) assembly. Although no significant difference was observed in the number of cells adhered on all samples, a systematic increase in the size of FA complexes was measured (i) on all rough HAP facets as compared with smooth HAP facets, and (ii) on 100-oriented facets as compared with their 001-oriented counterparts, in the case of rough HAP. This enhanced FA assembly was associated with higher amounts of Fn adsorbed and to more compact Fn conformations present at the 100 rough HAP surface. We propose that the differential Fn adsorption on HAP surfaces may regulate FA assembly by modulating the specificity of surface receptors, in particular integrins and glycosaminoglycans (GAGs), that pre-osteoblasts utilize to adhere to the underlying surface. Both the higher number and the higher accessibility of ligand binding sites on more compact Fn seems to promote assembly of larger FAs. Our findings suggest that this early stage alteration of FA assembly, likely induced by differential engagement

of surface receptors, may persist over time and influence late stage osteoblast proliferation, differentiation, and secretion. The altered osteoblast behaviors will in turn affect osteoclast activities and together modulate pathological remodeling of the bone matrix.

## **5.2 Introduction**

Cancer metastasis to bone induces pathological remodeling of the bone matrix, perturbing the balance between new bone deposition by osteoblasts and old bone degradation by osteoclasts. Cancer bone metastasis is generally divided into two categories: (i) osteoblastic metastases caused by the factors that stimulate osteoblast proliferation, differentiation and bone formation, and (ii) osteolytic metastases caused by osteoclast-activating factors. For example, breast cancer bone metastasis is predominantly osteolytic, resulting in bone loss (or osteolysis), increased bone fragility, and pathological fractures, while prostate cancer bone metastasis is usually osteoblastic, resulting in bone formation [1,2]. However, in most cases the site of metastasis have both osteolytic and osteoblastic characteristics, as bone resorption and bone formation are usually coupled [3]. In fact, osteoblasts play a critical role in mediating osteoclast differentiation and activation [4]. Moreover, cell-cell interactions are altered as breast cancer cells enter the bone microenvironment. The presence of breast cancer cells has been shown to impair osteoblasts viability, suppress their differentiation and expression of proteins required for bone formation [5], while enhancing secretion of pro-inflammatory cytokines by osteoblasts such as IL-8 [5,6], which may be a potential activator of osteoclast-mediated bone resorption [7]. The formation of actin stress fibers and focal adhesion plaques are also reduced in osteoblasts due to cytokines

secreted by breast cancer cells [8]. Thus osteolysis induced by breast cancer metastasis is due to both activation of osteoclasts and suppression of osteoblasts.

A lot of efforts has been devoted to studying how breast cancer secretion of parathyroid hormone-related protein (PTHrP) [9], cytokines (IL-6, IL-8, IL-11, etc) [5,7,8], and bone-derived growth factors (TGF- $\beta$ , etc) [10] affect osteoblast functions and osteoclast activation, but the cell-matrix interactions has been more rarely investigated. Since matrix properties are significantly altered in the tumor microenvironment [11,12], we hypothesize that these alterations will also impact bone cell functions through modified cell-matrix interactions. The bone extracellular matrix is composed primarily of collagen I (90%), proteoglycans, and glycoproteins. We focus on glycoprotein fibronectin (Fn) because it is the first bone matrix protein deposited by osteoblasts. Fn also plays an essential role in the subsequent deposition of collagen I and in maintaining the integrity of the collagen matrix [13–18]. In addition to cell-derived Fn, circulating plasma Fn has also been found in the bone matrix. In fact, plasma Fn represents the predominant source of Fn affecting bone mineralization and matrix properties, while osteoblast-derived Fn locally modulates osteoblast differentiation without appreciably changing matrix properties [19]. Additionally, Fn is a critical mechanotransducer known to regulate cellular responses to chemical, physical, and mechanical signals from the microenvironment [20,21]. Previous studies have shown that osteogenesis, osteoblast differentiation, and survival of matured osteoblast all depend on integrin-mediated interactions between osteoblasts and Fn [22,23]. In addition to integrins, cell surface proteoglycans or glycosaminoglycans (GAGs), in particular heparin sulfate, can also bind to the heparin-binding domains of Fn and this binding event has been shown to be necessary for initial osteoblast attachment to Fn-coated surfaces [24]. Therefore, osteoblast attachment and subsequent cell fate

may be regulated by differential Fn conformations via altered engagement of integrins (e.g., with RGD and its synergy site) and/or GAGs (e.g., with the heparin binding domains).

In Chapter 3, we have shown that hydroxyapatite (HAP) surfaces of controlled roughness and surface chemistry can induce differential Fn adsorption. Therefore these Fn coated HAP surfaces represent ideal ready-to-use platforms for studying interactions between osteoblasts and Fn. We choose to specifically investigate osteoblasts because previous studies have reported that their activities are highly sensitive to Fn conformational changes, surface chemistry, and topography of underlying substrates [25–30]. Since HAP is widely used as a bioactive material to promote bone regeneration and enhance integration of implants, there have been various studies on how HAP materials properties affect osteoblasts functions. For example, carbonated apatites with a high carbonate content (decreased surface charge and crystallinity) tend to enhance osteoblast adhesion and support high cell proliferation [31]. In physiological environment, the surface of implants is readily decorated with extracellular matrix (ECM) proteins such as Fn. The presence of Fn was reported to enhance osteoblast adhesion and spreading, and to promote the formation of focal adhesions and stress fibers on various substrates [32,33]. Fn adsorption force has also been shown to regulate late osteoblast adhesion, reorganization of the adsorbed Fn, and fibrillogenesis of endogenous Fn on self-assembled monolayers (SAMs) [26]. The integrin-mediated Fn fibrillogenesis is also important for osteoblast compaction, an early step during their differentiation [34]. Moreover, Fn-substrate interactions may persist to affect long-term osteoblast responses, in particular collagen deposition and matrix mineralization on microgrooved stainless steel surfaces [35]. However, whether the differential Fn adsorption induced by HAP surface properties will affect osteoblasts behaviors is unclear.

In this chapter, we focused on the initial adhesion of osteoblasts on Fn coated HAP facets to investigate whether early steps of the adhesion process, in particular the assembly of the first focal adhesion (FA) complexes were influenced by Fn coated HAP surface properties. Our results indicate that while neither the number of cells adhered nor the number of FAs per cell differed significantly on all HAP facets, the size of FA complexes varied as a function of Fn deposition and conformation induced by underlying HAP surface properties. Specifically, larger FAs systematically formed on rough HAP facets where larger amounts of more compact Fn were detected. Additionally, larger FAs were also measured on 100R as compared with 001R but, surprisingly, such surface chemistry effect was not observed on smooth facets.

## **5.3 Materials and Methods**

### **5.3.1 Cell culture and seeding**

MC3T3-E1 Subclone 4 (ATCC® CRL2593™) pre-osteoblast cells were cultured in  $\alpha$ -MEM media supplemented with 10% FBS and 1% P/S at 37 °C in 5% CO<sub>2</sub>, with media refreshed every 48 h. At approximately 80% confluency, cells were detached with trypsin-EDTA and used for cell seeding (passage number 4 ~ 13).

For cell seeding, HAP facets with controlled surface chemistry and roughness were embedded in PDMS slabs, as previously described in Chapter 4.3. Briefly, HAP/PDMS slabs were blocked with SuperBlock (Thermo Scientific) for 1 h and dried in air. Then a thin layer of PDMS sheet was removed to expose HAP surface area of approximately 5 mm by 7 mm. After UV sterilization for 1 h, HAP surfaces were washed three times with sterile PBS and a droplet of

50  $\mu\text{L}$  Fn solution (Invitrogen, diluted to 50  $\mu\text{g}/\text{mL}$  in PBS) was incubated on each HAP surface at 4  $^{\circ}\text{C}$  for 24 h in 24-well plates. For control sample, 130  $\mu\text{L}$  Fn solution was added per lab-tek chambered well. After washing three times with PBS, a droplet of 50  $\mu\text{L}$  cell solution containing circa 7,000 MC3T3-E1 cells was added onto each Fn coated HAP facet (in serum-free  $\alpha$ -MEM supplemented with 1% P/S, seeding density  $2 \times 10^4 / \text{cm}^2$ ). After 30 min of initial cell adhesion, additional 750  $\mu\text{L}$  serum-free  $\alpha$ -MEM supplemented with 1% P/S was added into each well, resulting in a total volume of 800  $\mu\text{L}$  media per well. For control sample (8-well Lab-Tek chambered borosilicate coverglass, Thermo Fisher Scientific), 114  $\mu\text{L}$  cell solution containing circa 16,000 cells was added per well (seeding density  $2 \times 10^4 / \text{cm}^2$ ); after 30 min, additional 286  $\mu\text{L}$  media was added leading to a total volume of 400  $\mu\text{L}$  media per well. After culturing at 37  $^{\circ}\text{C}$  in 5%  $\text{CO}_2$  for 2 h post initial cell seeding, culture media were collected and cells were stained for viability and adhesion analysis.

### 5.3.2 Cell viability and adhesion

Cell viability was examined with a LIVE/DEAD<sup>®</sup> Viability/Cytotoxicity Kit (Molecular Probes, OR) based on the simultaneous determination of live and dead cells with calcein AM and ethidium homodimer (EthD-1), respectively. Nonfluorescent cell-permeant calcein AM converts to intensely green fluorescent calcein, which is membrane impermeable, after cleaved by intracellular esterase in live cells. EthD-1 can only enter damaged membranes of dead cells and produces a bright red fluorescence upon binding to nucleic acids. After collecting culture media, samples were washed once gently with warm PBS, and incubated in Live/Dead working solution (PBS containing 2  $\mu\text{M}$  calcein-AM and 4  $\mu\text{M}$  EthD-1) for 30 minutes at 37  $^{\circ}\text{C}$  in 5%  $\text{CO}_2$ . Then images were acquired in phenol red free DMEM/F12 media with a Zeiss LSM880 inverted confocal microscope (Zeiss, Munich, Germany), using a Fluar 5x/0.25 M27 objective. Calcein

was excited with a 488 nm laser set at 2% laser power, and EthD-1 was excited with a 561 nm laser set at 2% laser power. Tiling images were acquired with 10% overlap between adjacent images over the entire sample surface. Images were analyzed in ImageJ (NIH).

### 5.3.3 Immunostaining and imaging

For immunostaining, samples were washed with 800  $\mu$ L (200  $\mu$ L for control) warm PBS for three times and fixed in 50  $\mu$ L (200  $\mu$ L for control) 3.7% formalin for 1 h at 4 °C. To permeabilize cell membranes, samples were washed twice with 50  $\mu$ L 0.05% Triton-X in PBS (PBS-X, Thermo Scientific, 200  $\mu$ L for control) for 5 min each time, and then blocked for 30 min at room temperature with 50  $\mu$ L (200  $\mu$ L for control) PBS-X/1% SuperBlock (Thermo Scientific). To immunostain for vinculin, samples were incubated with 50  $\mu$ L (125  $\mu$ L for control) primary mouse anti-vinculin antibodies (1:1000, clone VIN115, Sigma-Aldrich) in PBS/1%SuperBlock at 4 °C overnight. Samples were then washed twice with 50  $\mu$ L PBS-X (200  $\mu$ L for control) for 5 min each time, and incubated with 50  $\mu$ L (200  $\mu$ L for control) goat anti-mouse IgG1 ( $\gamma$ 1), CF<sup>TM</sup>555 secondary antibodies (1:1000, Sigma-Aldrich) and DAPI (1:1000, Life Technologies) in PBS/1%SuperBlock at room temperature for 1 h. Finally samples were washed twice with 50  $\mu$ L PBS (200  $\mu$ L for control) for 5 min each time and kept in PBS at 4 °C until imaging.

Z-stack images were acquired with a Zeiss LSM880 inverted confocal microscope (Zeiss, Munich, Germany) using a C-Achroplan water-immersion 32x/0.85 objective, zoom-in 1.3x, a pinhole of 2AU (2  $\mu$ m section), and a z step size of 1  $\mu$ m. DAPI was excited with a 405 nm laser set at 5% laser power, and CF<sup>TM</sup>555 was excited with a 561 nm laser set at 5% laser power. For

nuclei counting, a Fluar 5x/0.25 M27 objective was used, and tiling images were acquired with 10% overlap between adjacent images. Images were analyzed in ImageJ (NIH).

#### 5.3.4 HAP facets cleaning

After each experiment, cells were removed from HAP facets by washing three times with PBS and then incubating in 0.5% trypsin in PBS at 37 °C for 30 min. After washing three times with PBS, any remaining cell residues were cleaned by cell scrapers. HAP facets were then immersed in PBS containing 5% sodium dodecyl sulfate (SDS) overnight, sonicated in 0.1 M NaOH, and rinsed with DI water and ethanol.

#### 5.3.5 Statistical analysis

One-way ANOVA with Tukey's post test and Student's t-test were used to determine statistical significance between conditions in GraphPad Prism (GraphPad Software, Inc., CA). In all cases,  $p < 0.05$  is indicated by a single star,  $p < 0.01$  by two stars and  $p < 0.001$  by three stars.

## 5.4 Results

### 5.4.1 Pre-osteoblast cell viability

First we investigated the viability of pre-osteoblast cells on Fn coated geologic HAP facets, as quantified by the percentage of live cells (live cells in green, dead cells in red, **Figure 5.1**). After culturing for 2 h, cell viability was found to be 92.9%, 92.4%, 90.2%, 92.7%, and 93.6% for 100S, 001S, 100R, 001R, and control coverglass, respectively. Thus cell viability was not affected after culturing for 2 h on Fn-coated HAP facets.

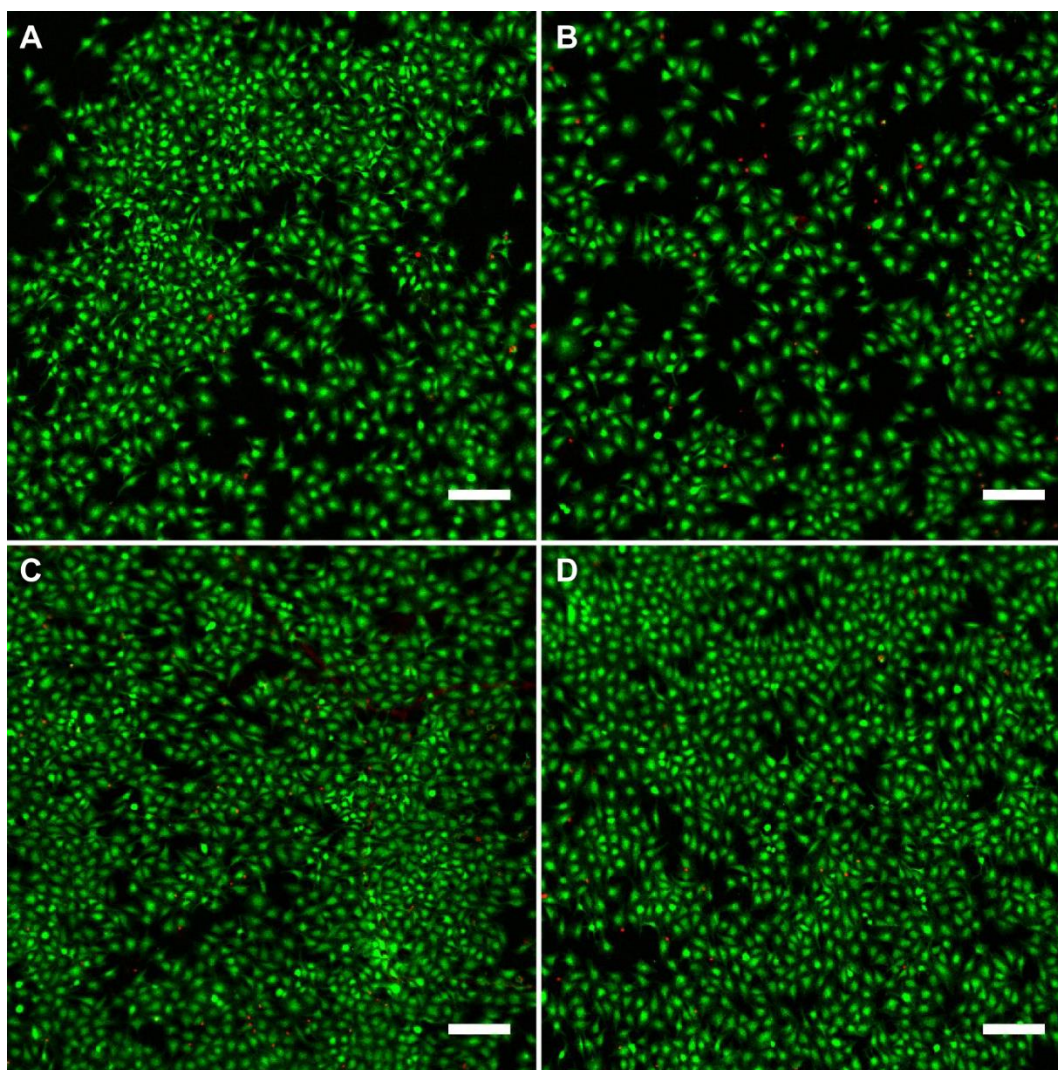


**Figure 5.1** Live/Dead confocal images acquired for (A) 100S, (B) 001S, (C) 100R, and (D) 001R after culturing for 2 h. Live cells were stained in green and dead cells in red. Only one representative confocal tile image is shown for each HAP facet. Scale bars 200  $\mu\text{m}$ .

#### 5.4.2 Pre-osteoblast cell adhesion

Next we investigated whether the number of live cells adhered depends on the differential Fn adsorption on HAP facets. Our results show that cell numbers were similar on all HAP facets and control coverglass (**Figure 5.2**).

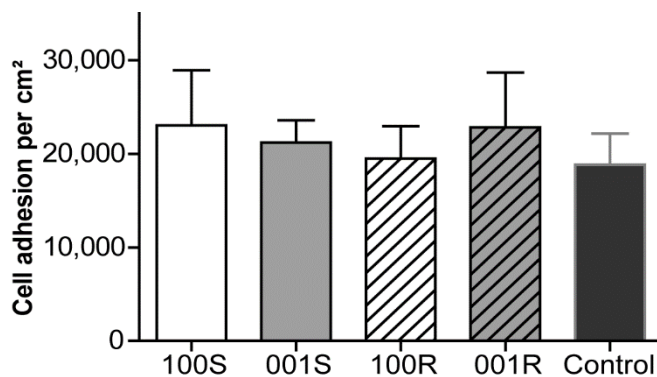


**Figure 5.2** Number of pre-osteoblasts adhered per unit area after culturing for 2 h on Fn coated HAP facets and control coverglass. Data collected from three independent experiments. Mean  $\pm$  SD.

#### 5.4.3 Focal adhesion assembly

To investigate whether the initial formation of FAs depends on underlying Fn properties induced by HAP substrates, pre-osteoblasts were then stained for nuclei and FA complexes were identified by immunofluorescence staining of vinculin. Confocal images were next analyzed to determine FA features. Representative images are shown in **Figure 5.3**. Compared with MDA-MB-231 breast cancer cells (Chapter 4, **Figure 4.5**), there was overall less vinculin present within the central regions of MC3T3-E1 osteoblast cells cytoplasm, i.e., vinculin not associated with FAs.

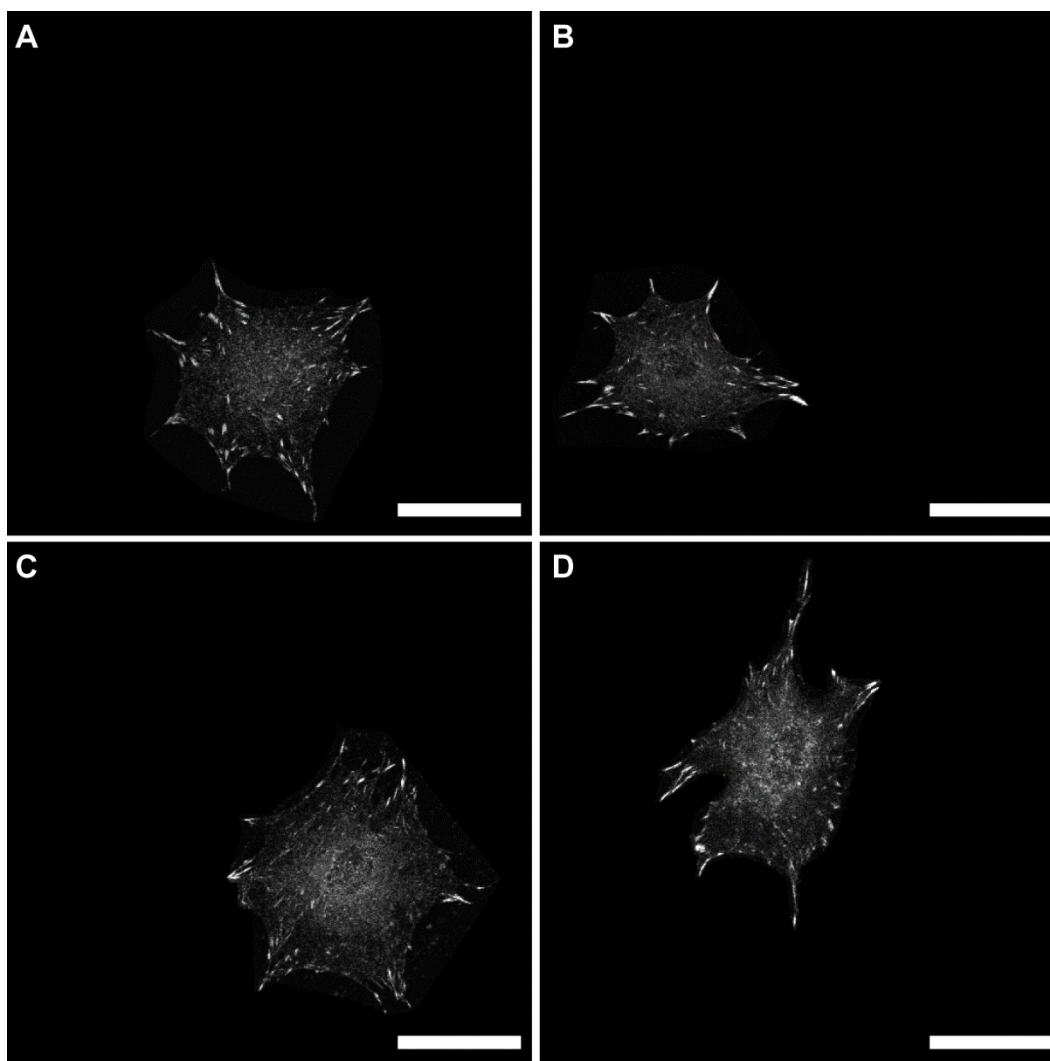


**Figure 5.3** Representative confocal images of immunostained vinculin in MC3T3-E1 pre-osteoblast cells seeded on Fn coated (A) 100S, (B) 001S, (C) 100R, and (D) 001R HAP facets. Scale bars 50  $\mu\text{m}$ .

Our analysis of FA features is summarized in **Figure 5.4**. The number of FAs per cell seemed to be independent on underlying Fn and HAP surface properties. However, after only 2 h in contact with HAP facets, MC3T3-E1 cells developed nearly twice the number of FAs per cell

as that of MDA-MB-231 cells after 24 h, while only a small increase in FA number was observed for MC3T3-E1s on control samples (Chapter 4, **Figure 4.6**). These results suggest that HAP is a more suitable substrate for adhesion of pre-osteoblast cells as compared with breast cancer cells.

Moreover, the size of FA complexes strongly depended on both surface roughness and surface chemistry of HAP facets (**Figure 5.4**). Increasing surface roughness resulted in an increase in both FA area and FA width, regardless of surface chemistry. The length of FAs also increased on 100R as compared with 100S. The frequency distribution histograms consistently showed a higher fraction of large and wide FAs on rough HAP facets (**Figure 5.5**). Interestingly, surface chemistry only influenced FA area and FA length on rough facets (in spite of the heterogeneity of surface chemistry due to the presence of polishing grooves): an increase in both FA area and FA length was observed on 100R as compared with on 001R, as also reflected in the frequency distribution histograms.

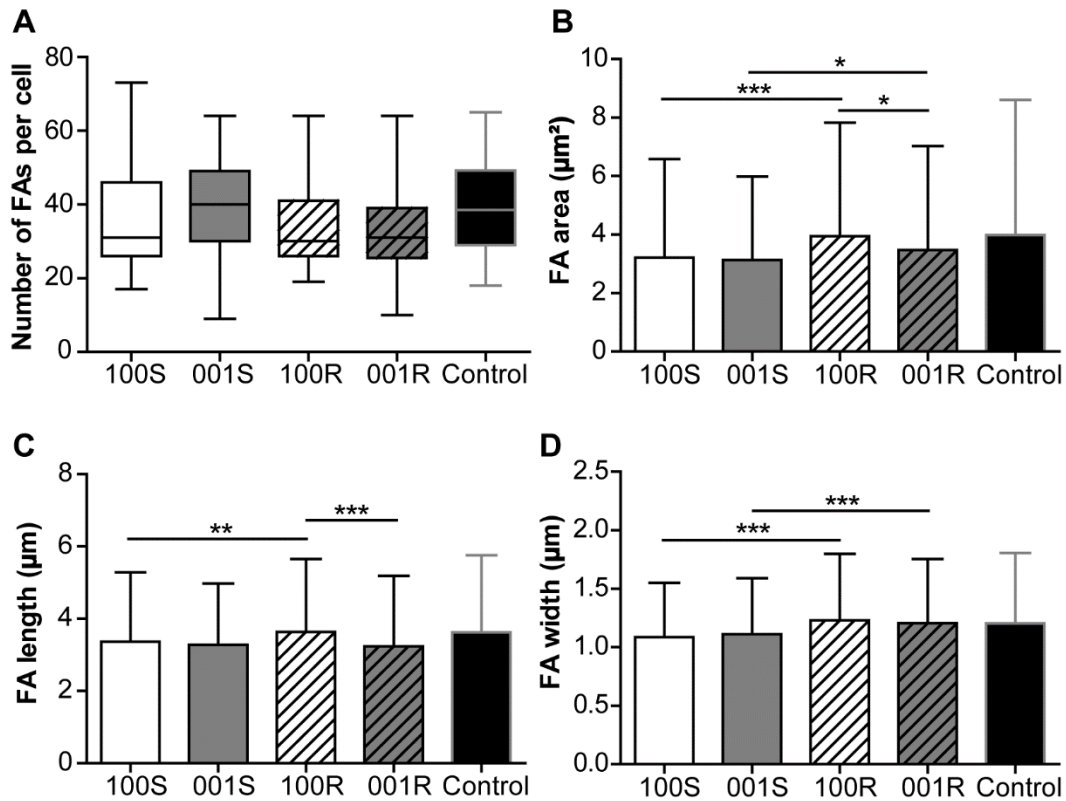


**Figure 5.4** Focal adhesion (FA) analysis of MC3T3-E1 pre-osteoblast cells after culturing for 2 h on Fn coated HAP facets and control coverglass: (A) number of FAs per cell, (B) FA area, (C) FA length, and (D) FA width. Immunofluorescence of vinculin was used to identify and characterize FAs. Data collected from three independent experiments. Number of cells analyzed: N = 31, 27, 27, 21 and 30 for 100S, 001S, 100R, 001R, and control, respectively. Number of FAs analyzed: n = 1094, 1089, 921, 691, and 1177, for 100S, 001S, 100R, 001R, and control, respectively. In all cases,  $p < 0.05$  is indicated by a single asterisk,  $p < 0.01$  by two asterisks, and  $p < 0.001$  by three asterisks. Mean  $\pm$  SD.

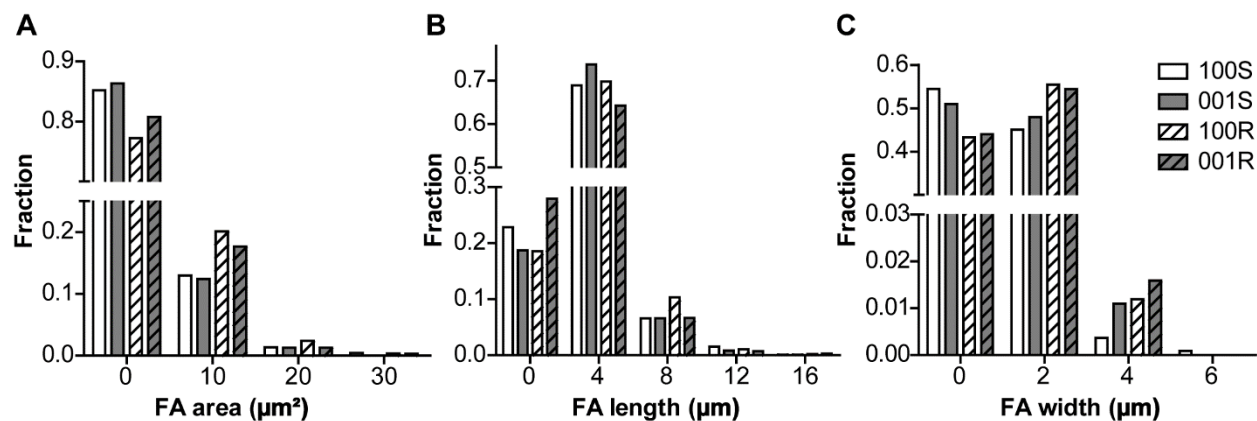


**Figure 5.5** Frequency distributions of (A) FA area, (B) FA length, and (C) FA width of MC3T3-E1 pre-osteoblast cells seeded on Fn coated HAP facets after culturing for 2 h.

## 5.5 Discussion

The number of MC3T3-E1 cells adhered to HAP was independent on underlying Fn conformation or HAP surface properties, similar to what was observed for MDA-MB-231 cells in Chapter 4 (**Figure 4.4**). Although different HAP surface chemistry and topography trigger changes in Fn conformation (Chapter 3, **Figure 3.7A**) leading to either exposure or disruption of binding sites for various cell ligands such as integrins, pre-osteoblasts may express multiple types of integrins on cell surface that compensate for each other. Indeed, it has been shown that osteoblasts express  $\alpha_5\beta_1$ ,  $\alpha_3\beta_1$ ,  $\alpha_8\beta_1$ , and  $\alpha_v\beta_3$  integrins at early stage of culture (3 days), although expression levels of  $\alpha_3\beta_1$  and  $\alpha_8\beta_1$  are possibly down-regulated at late stage of osteoblast differentiation [22]. All these types of integrins recognize the RGD binding site located on Fn-III<sub>10</sub> [36], while  $\alpha_5\beta_1$  integrins require the additional synergy site located on Fn-III<sub>9</sub> for

concomitant engagement of both Fn-III<sub>9</sub> and Fn-III<sub>10</sub>, which makes their binding highly dependent on Fn conformation [37]. Thus when unfolding of Fn disrupts the binding region for  $\alpha_5\beta_1$  integrins (either because the distance between Fn-III<sub>9</sub> and Fn-III<sub>10</sub> is too large or because the relative angle between modules is altered), other types of integrins can compensate for the loss of  $\alpha_5\beta_1$  [38]. Since  $\alpha_5\beta_1$  integrins have been shown to mediate critical osteoblast-Fn interactions that are required for both bone morphogenesis and osteoblast differentiation, differential integrin engagement with Fn may exhibit more significant effects at later stage of osteoblast differentiation [22,28].

Additionally, although higher amounts of Fn could adsorb on rough HAP facets (Chapter 3, **Figure 3.7B**), this increased Fn quantity (hence increased ligand density) was not associated with enhanced pre-osteoblasts adhesion. This may be explained by the concept of ‘minimum Fn active density’ observed in previous studies: a minimum active/functional Fn ligand density (measured by HFN7.1 antibody binding) is required to achieve maximum 3T3-E1 osteoblast adhesion, regardless of surface chemistry of underlying substrates [25]. Thus, although there were less Fn molecules adsorbed onto smooth HAP facets, the level of active Fn ligand density might have reached the minimum requirement for maximum cell adhesion, which is approximately 20 ~ 200 ng/cm<sup>2</sup> (maximum Fn coating concentration 20 µg/mL) for SAMs with various functional groups [25], while we used a much higher Fn coating concentration (50 µg/mL, approximately 7 µg/cm<sup>2</sup>).

In addition to the integrin family of receptors, cell surface GAGs such as heparan sulfate are also known to interact with Fn via heparin-binding domains. In fact, it has been shown that the participation of cell-surface GAGs is necessary for initial human osteoblast attachment, in addition to integrin binding [24]. The major binding site for heparin-like GAGs is the C-terminal

Hep-2 binding domain located on Fn-III<sub>13-14</sub> (with highest affinity for heparin and heparan sulfate [39,40]). Since Fn-III<sub>13</sub> carries a clump of positively charged residues [41], it may interact with negatively GAGs via electrostatic interactions, which could interfere with quaternary structure of the module and expose cryptic binding sites. Moreover, the underlying negatively charged HAP surfaces (Chapter 3, **Table 3.1**) could also affect the accessibility of binding sites in both positively charged Fn-III<sub>13-14</sub> (GAGs binding) and negatively charge Fn-III<sub>9-10</sub> (integrin binding) modules. These competing effects may together regulate osteoblast adhesion onto Fn coated HAP facets. As the Fn-III<sub>12-14</sub> domain also binds to a variety of growth factors, including vascular endothelial growth factors [42], the conformational changes in this domain will regulate sequestration and presentation of growth factors in Fn matrix [43]. For example, the binding of heparin to Fn has been shown to co-regulate Fn conformation with mechanical strain in matrix Fn fibers [44], and subsequently affect human mesenchymal stem cells osteogenic differentiation [45].

The assembly of FAs, in particular FA sizes, seem to depend on both HAP surface chemistry and topography/roughness, probably mediated by cell-Fn interactions. Regarding FA assembly on Fn coated substrates, there have been debatable results reported in previous studies utilizing SAMs. Previous work by García et al using Fn coated SAMs have shown that surface chemistry modulate the localization of clustered  $\alpha_5\beta_1$  and  $\alpha_v$  integrins (probably  $\alpha_v\beta_3$ ) within FAs of MC3T3-E1 cells: while  $-\text{COOH}$  surfaces support binding of both  $\alpha_5\beta_1$  and  $\alpha_v$  integrins,  $-\text{OH}$  and  $-\text{NH}_2$  surfaces selectively recruited  $\alpha_5\beta_1$  [25]. Later their study shows that surface chemistry also influence the organization of vinculin as well as other components in FAs. In particular, vinculin is localized to large mature FA complexes on the charged  $-\text{NH}_2$  and  $-\text{COOH}$  surfaces, while forming smaller, more punctate nascent clusters on the neutral  $-\text{OH}$  surfaces, and poorly defined

structures on the hydrophobic  $-\text{CH}_3$  surfaces, although a different trend was observed for other FA components [29]. However, another study using Fn coated SAMs demonstrated larger FA areas formed in MC3T3-E1 cells on  $-\text{OH}$  surfaces (with less amount of Fn adsorbed but better accessibility of cell binding domain located on Fn-III<sub>9-10</sub> in agreement with [25,29]) than on  $-\text{NH}_2$  and  $-\text{CH}_3$  surfaces [26]. Since these studies used different Fn coating concentrations, it may suggest that FA assembly not only depends on surface chemistry induced Fn conformational changes, but also on surface Fn density. We propose that the larger FA sizes we observed with increasing surface roughness may be correlated with better accessibility of the cell binding domain, as suggested by the more compact Fn conformation measured via FRET (Chapter 3, **Figure 3.7A**). The recruitment of specific integrins in the FAs remains to be further investigated.

Furthermore, the assembly of FAs by 3T3-E1 cells, in particular FA sizes, seems to be more sensitive to HAP topography/roughness than to surface chemistry induced Fn conformational changes. Similarly, previous work has shown that 3T3-E1 osteoblast adhesion and metabolic activity were more sensitive to surfaces roughness than to the type of proteins adsorbed on HAP substrates [46]. They also showed that HAP substrates with higher surface roughness and more negative zeta potential enhanced Fn adsorption, revealing increased accessibility of Fn cell binding domains, which is in agreement with our FRET results in Chapter 3 (**Figure 3.7**). Other work has suggested that specific substrate topographical features may mediate osteoblasts responses via different intracellular signaling pathways, which could possibly explain why differences in FA area and length induced by surface chemistry were observed on rough HAP facets but not on smooth HAP facets [47].

Collectively, these results and previous results in Chapter 4 suggest that HAP surface chemistry and topography/roughness can regulate FA assembly in both pre-osteoblast cells and

breast cancer cells via different mechanisms. While MDA-MB-231 cells are more sensitive to surface chemistry, MC3T3-E1 cells seem to better respond to surface topography/roughness of HAP facets. Moreover, the number of FA complexes per cell increased with HAP surface roughness for MC3T3-E1 cells, but decreased on 001R vs. 001S for MDA-MB-231 cells. Thus the roles of surface chemistry and topography/roughness of HAP in regulating cellular behaviors are cell-type dependent, and differential engagement of ligands with underlying Fn may be responsible for varied cell-HAP interactions.

In future experiments, investigating pre-osteoblasts seeded on HAP facets without Fn will help us elucidate whether the differential FA assembly by these cells is mediated by integrin/GAGs engagement or by surface roughness of HAP itself. Additionally, the use of 3D culture systems instead of 2D substrates will provide more suitable platforms for deciphering *in vivo* cellular behaviors.

## 5.6 Conclusions

In summary, using geologic HAP facets we are able to investigate individual effects of HAP surface chemistry and topography on Fn-mediated early osteoblast adhesion. We observed high efficiency of initial cell attachment on all samples (much higher than for breast cancer cells), probably due to the high Fn concentration used and therefore high ligand density. The differential assembly of FAs depended on both surface chemistry and surface topography, while the latter seemed to play a predominant role. The larger size of FA complexes formed on rough HAP facets was associated with higher amounts of more compact Fn adsorbed. The interactions between Fn and osteoblasts surface receptors, in particular integrins and GAGs, were probably

involved in this process. It should be noted that both surface chemistry and topography can directly induce altered FA assembly, cell adhesion, and differentiation, without the presence of Fn [48,49]. Further investigations are required to elucidate whether Fn mediates or simply amplifies the effects of HAP surface chemistry and topography on initial osteoblasts attachment.

## REFERENCES

- [1] G.R. Mundy, Metastasis to bone: causes, consequences and therapeutic opportunities., *Nat. Rev. Cancer.* 2 (2002) 584–93. doi:10.1038/nrc867.
- [2] Y.-C. Chen, D.M. Sosnoski, A.M. Mastro, Breast cancer metastasis to the bone: mechanisms of bone loss., *Breast Cancer Res.* 12 (2010) 215. doi:10.1186/bcr2781.
- [3] P. Garnero, N. Buchs, J. Zekri, R. Rizzoli, R.E. Coleman, P.D. Delmas, Markers of bone turnover for the management of patients with bone metastases from prostate cancer., *Br. J. Cancer.* 82 (2000) 858–64. doi:10.1054/bjoc.1999.1012.
- [4] Khosla S, Minireview: the OPG/RANKL/RANK system., *Endocrinology.* 142 (2001) 5050–5055. doi:10.1210/endo.142.12.8536.
- [5] M. Kinder, E. Chislock, K.M. Bussard, L. Shuman, A.M. Mastro, Metastatic breast cancer induces an osteoblast inflammatory response, *Exp. Cell Res.* 314 (2008) 173–183. doi:10.1016/j.yexcr.2007.09.021.
- [6] K.M. Bussard, D.J. Venzon, A.M. Mastro, Osteoblasts are a major source of inflammatory cytokines in the tumor microenvironment of bone metastatic breast cancer, *J. Cell. Biochem.* 111 (2010) 1138–1148. doi:10.1002/jcb.22799.
- [7] M.S. Bendre, D.C. Montague, T. Peery, N.S. Akel, D. Gaddy, L.J. Suva, Interleukin-8 stimulation of osteoclastogenesis and bone resorption is a mechanism for the increased osteolysis of metastatic bone disease, *Bone.* 33 (2003) 28–37. doi:10.1016/S8756-3282(03)00086-3.
- [8] R.R. Mercer, A.M. Mastro, Cytokines secreted by bone-metastatic breast cancer cells alter the expression pattern of f-actin and reduce focal adhesion plaques in osteoblasts through PI3K, *Exp. Cell Res.* 310 (2005) 270–281. doi:10.1016/j.yexcr.2005.07.029.
- [9] T.A. Guise, Parathyroid hormone-related protein and bone metastases., *Cancer.* 80 (1997) 1572–1580. doi:10.1002/(SICI)1097-0142(19971015)80:8+<1572::AID-CNCR7>3.0.CO;2-M.
- [10] P. Juárez, T.A. Guise, TGF- $\beta$  in cancer and bone: Implications for treatment of bone metastases, *Bone.* 48 (2011) 23–29. doi:10.1016/j.bone.2010.08.004.

- [11] K. Wang, R.C. Andresen Eguiluz, F. Wu, B.R. Seo, C. Fischbach, D. Gourdon, Stiffening and unfolding of early deposited-fibronectin increase proangiogenic factor secretion by breast cancer-associated stromal cells, *Biomaterials*. 54 (2015) 63–71. doi:10.1016/j.biomaterials.2015.03.019.
- [12] X. Bi, C. Patil, C. Morrissey, M.P. Roudier, A. Mahadevan-Jansen, J. Nyman, Characterization of Bone Quality in Prostate Cancer Bone Metastases Using Raman Spectroscopy, *Proc. SPIE Vol. 7548* (2010) 75484L–1–75484L–6. doi:10.1117/12.853551.
- [13] R.E. Weiss, A.H. Reddi, Appearance of fibronectin during the differentiation of cartilage, bone, and bone marrow., *J. Cell Biol.* 88 (1981) 630–6. doi:10.1083/jcb.88.3.630.
- [14] E.A. Cowles, M.E. DeRome, G. Pastizzo, L.L. Brailey, G.A. Gronowicz, Mineralization and the expression of matrix proteins during in vivo bone development, *Calcif Tissue Int.* 62 (1998) 74–82.
- [15] P. Singh, C. Carraher, J.E. Schwarzbauer, Assembly of fibronectin extracellular matrix, *Annu. Rev. Cell Dev. Biol.* 26 (2010) 397–419. doi:10.1146/annurev-cellbio-100109-104020.
- [16] S.L. Dallas, Q. Chen, P. Sivakumar, Dynamics of assembly and reorganization of extracellular matrix proteins., *Curr. Top. Dev. Biol.* 75 (2006) 1–24. doi:10.1016/S0070-2153(06)75001-3.
- [17] J. Sottile, D.C. Hocking, Fibronectin polymerization regulates the composition and stability of extracellular matrix fibrils and cell-matrix adhesions, *Mol. Biol. Cell.* 13 (2002) 3546–3559. doi:10.1091/mbc.E02-01-0048.
- [18] P.G. Grzesik, Wojciech J, Robey, Bone Matrix RGD Glycoproteins: Immunolocalization Bone Cells In Vitro, *J. Bone Miner. Res.* 9 (1994) 487–496.
- [19] A. Bentmann, N. Kawelke, D. Moss, H. Zentgraf, Y. Bala, I. Berger, et al., Circulating fibronectin affects bone matrix, whereas osteoblast fibronectin modulates osteoblast function., *J. Bone Miner. Res.* 25 (2010) 706–715. doi:10.1359/jbmr.091011.
- [20] K.C. Clause, T.H. Barker, Extracellular matrix signaling in morphogenesis and repair., *Curr. Opin. Biotechnol.* 24 (2013) 830–3. doi:10.1016/j.copbio.2013.04.011.
- [21] M.J. Bradshaw, M.L. Smith, Multiscale relationships between fibronectin structure and

- functional properties., *Acta Biomater.* 10 (2014) 1524–31. doi:10.1016/j.actbio.2013.08.027.
- [22] A.M. Moursi, R.K. Globus, C.H. Damsky, Interactions between integrin receptors and fibronectin are required for calvarial osteoblast differentiation in vitro., *J. Cell Sci.* 110 ( Pt 1 (1997) 2187–2196.
- [23] R.K. Globus, S.B. Doty, J.C. Lull, E. Holmuhamedov, M.J. Humphries, C.H. Damsky, Fibronectin is a survival factor for differentiated osteoblasts., *J. Cell Sci.* 111 (1998) 1385–1393.
- [24] B. Sim, J. Cladera, P. O’Shea, Fibronectin interactions with osteoblasts: identification of a non-integrin-mediated binding mechanism using a real-time fluorescence binding assay, *J Biomed Mater Res A.* 68 (2004) 352–359. doi:10.1002/jbm.a.20022.
- [25] B.G. Keselowsky, D.M. Collard, A.J. García, Surface chemistry modulates fibronectin conformation and directs integrin binding and specificity to control cell adhesion., *J. Biomed. Mater. Res. A.* 66 (2003) 247–59. doi:10.1002/jbm.a.10537.
- [26] M. Lin, H. Wang, C. Ruan, J. Xing, J. Wang, Y. Li, et al., Adsorption Force of Fibronectin on Various Surface Chemistries and Its Vital Role in Osteoblast Adhesion, *Biomacromolecules.* 16 (2015) 973–984. doi:10.1021/bm501873g.
- [27] Aniket, R. Reid, B. Hall, I. Marriott, A. El-Ghannam, Early osteoblast responses to orthopedic implants: Synergy of surface roughness and chemistry of bioactive ceramic coating, *J. Biomed. Mater. Res. Part A.* (2014) n/a–n/a. doi:10.1002/jbm.a.35326.
- [28] S.N. Stephansson, B.A. Byers, A.J. García, Enhanced expression of the osteoblastic phenotype on substrates that modulate fibronectin conformation and integrin receptor binding, *Biomaterials.* 23 (2002) 2527–2534. doi:10.1016/S0142-9612(01)00387-8.
- [29] B.G. Keselowsky, D.M. Collard, A.J. García, Surface chemistry modulates focal adhesion composition and signaling through changes in integrin binding, *Biomaterials.* 25 (2004) 5947–5954. doi:10.1016/j.biomaterials.2004.01.062.
- [30] M.H. Lee, N. Oh, S.W. Lee, R. Leesungbok, S.E. Kim, Y.P. Yun, et al., Factors influencing osteoblast maturation on microgrooved titanium substrata, *Biomaterials.* 31 (2010) 3804–3815. doi:10.1016/j.biomaterials.2010.01.117.

- [31] I.Y. Pieters, N.M.F. Van den Vreken, H. a Declercq, M.J. Cornelissen, R.M.H. Verbeeck, Carbonated apatites obtained by the hydrolysis of monetite: influence of carbonate content on adhesion and proliferation of MC3T3-E1 osteoblastic cells, *Acta Biomater.* 6 (2010) 1561–8. doi:10.1016/j.actbio.2009.11.002.
- [32] G. Schneider, K. Burrige, Formation of focal adhesions by osteoblasts adhering to different substrata, *Exp. Cell Res.* 214 (1994) 264–269. doi:10.1006/excr.1994.1257.
- [33] M. Hindie, M.C. Degat, F. Gaudiere, O. Gallet, P.R. Van Tassel, E. Pauthe, Pre-osteoblasts on poly(l-lactic acid) and silicon oxide: Influence of fibronectin and albumin adsorption, *Acta Biomater.* 7 (2011) 387–394. doi:10.1016/j.actbio.2010.08.001.
- [34] M. Brunner, A. Millon-Frémillon, G. Chevalier, I.A. Nakchbandi, D. Mosher, M.R. Block, et al., Osteoblast mineralization requires  $\beta 1$  integrin/ICAP-1-dependent fibronectin deposition, *J. Cell Biol.* 194 (2011) 307–322. doi:10.1083/jcb.201007108.
- [35] A.C. De Luca, M. Zink, A. Weidt, S.G. Mayr, A.E. Markaki, Effect of microgrooved surface topography on osteoblast maturation and protein adsorption, *J. Biomed. Mater. Res. - Part A.* 103 (2015) 2689–2700. doi:10.1002/jbm.a.35407.
- [36] S. Johansson, G. Svineng, K. Wennerberg, L. Lohikangas, Fibronectin-integrin interactions, *Front. Biosci.* 2 (1997) 126–146.
- [37] A. Krammer, D. Craig, W.E. Thomas, K. Schulten, V. Vogel, A structural model for force regulated integrin binding to fibronectin's RGD-synergy site, *Matrix Biol.* 21 (2002) 139–147. doi:10.1016/S0945-053X(01)00197-4.
- [38] T.A. Petrie, J.R. Capadona, C.D. Reyes, A.J. García, Integrin specificity and enhanced cellular activities associated with surfaces presenting a recombinant fibronectin fragment compared to RGD supports, *Biomaterials.* 27 (2006) 5459–5470. doi:10.1016/j.biomaterials.2006.06.027.
- [39] F.J.B. Barkalow, J.E. Schwarzbauer, Localization of the major heparin-binding site in fibronectin, *J. Biol. Chem.* 266 (1991) 7812–7818.
- [40] M.J. Benecky, C.G. Kolvenbach, D.L. Amrani, M.W. Mosesson, Evidence that binding to the carboxyl-terminal heparin-binding domain (Hep II) dominates the interaction between plasma fibronectin and heparin., *Biochemistry.* 27 (1988) 7565–71. <http://www.ncbi.nlm.nih.gov/pubmed/3207688>.

- [41] A. Sharma, J.A. Askari, M.J. Humphries, E.Y. Jones, D.I. Stuart, Crystal structure of a heparin- and integrin-binding segment of human fibronectin., *EMBO J.* 18 (1999) 1468–79. doi:10.1093/emboj/18.6.1468.
- [42] M.M. Martino, J.A. Hubbell, The 12th-14th type III repeats of fibronectin function as a highly promiscuous growth factor-binding domain., *FASEB J.* 24 (2010) 4711–4721. doi:10.1096/fj.09-151282.
- [43] M. Mitsi, K. Forsten-Williams, M. Gopalakrishnan, M.A. Nugent, A catalytic role of heparin within the extracellular matrix, *J. Biol. Chem.* 283 (2008) 34796–34807. doi:10.1074/jbc.M806692200.
- [44] B. Hubbard, J.A. Buczek-Thomas, M.A. Nugent, M.L. Smith, Heparin-dependent regulation of fibronectin matrix conformation., *Matrix Biol.* 34 (2014) 124–31. doi:10.1016/j.matbio.2013.10.006.
- [45] B. Li, Z. Lin, M. Mitsi, Y. Zhang, V. Vogel, Heparin-induced conformational changes of fibronectin within the extracellular matrix promote hMSC osteogenic differentiation, *Biomater. Sci.* 3 (2015) 73–84. doi:10.1039/C3BM60326A.
- [46] N. Ribeiro, S.R. Sousa, F.J. Monteiro, Influence of crystallite size of nanophased hydroxyapatite on fibronectin and osteonectin adsorption and on MC3T3-E1 osteoblast adhesion and morphology., *J. Colloid Interface Sci.* 351 (2010) 398–406. doi:10.1016/j.jcis.2010.08.013.
- [47] D.W. Hamilton, D.M. Brunette, The effect of substratum topography on osteoblast adhesion mediated signal transduction and phosphorylation, *Biomaterials.* 28 (2007) 1806–1819. doi:10.1016/j.biomaterials.2006.11.041.
- [48] D.W. Hamilton, F. Jamshidi, D.M. Brunette, Focal adhesion mediated intracellular signaling, Stat3 translocation and osteoblast differentiation: Regulation by substratum topography, *Materwiss. Werksttech.* 40 (2009) 101–107. doi:10.1002/mawe.200800370.
- [49] J.Y. Lim, A.F. Taylor, Z. Li, E.A. Vogler, H.J. Donahue, Integrin expression and osteopontin regulation in human fetal osteoblastic cells mediated by substratum surface characteristics., *Tissue Eng.* 11 (2005) 19–29. doi:10.1089/ten.2005.11.19.

## Chapter 6.

### Conclusions & Future Directions

The aim of this thesis was to develop cell culture platforms to investigate the role of HAP/Fn interactions in mediating subsequent cellular behaviors with possible implications in cancer bone metastasis. We first combined nanoparticle synthesis with FRET spectroscopy to quantify the deposition and conformation of Fn adsorbed onto HAP nanoparticles with various materials properties (Chapter 2). Our data reveal that larger amounts of more compact Fn molecules adsorbed onto HAP nanoparticles with smaller size, lower crystallinity, and more negative zeta potential, *i.e.*, onto HAP that resembled normal bone apatite. Additionally, the adsorption of compact Fn molecules systematically increased with increasing HAP concentration, which was attributed to the formation of large HAP agglomerates. Collectively, these results suggest that both the surface chemistry of single HAP nanoparticles and the size and morphology of agglomerates forming at HAP high concentration contribute to Fn adsorption [1]. The major limitations of this Fn/HAP nanoparticles platform were (i) that cellular uptake of nanoparticles could affect cell viability and behaviors, and (ii) that it was difficult to deconvolute the effects of surface chemistry and morphology/topography of HAP.

Consequently, we next utilized large geologic apatite single crystals both to avoid cellular uptake of nanoparticles and to enable the deconvolution of surface chemistry and topography effects of the mineral (Chapters 3 & 4). Our data indicated that HAP surface properties induced changes not only in Fn conformation (ligand availability) but also in the amount of Fn adsorbed (ligand density). Additionally, among all four types of HAP facets investigated, the smooth (001)

facet coated with the most unfolded Fn triggered the highest levels of proangiogenic (VEGF) and proinflammatory (IL-8) secretions by MDA-MB-231 breast cancer cells. These findings suggest that Fn conformation regulates early cell signaling independently of other variables typically associated with altered ECM deposition (*e.g.*, composition, rigidity) [2], and that variations in integrin binding specificity may underlie these changes. Further experiments are required to confirm this mechanism of integrin binding, for example, blocking specific integrins individually and concomitantly to see if it affects cell functions. The importance of integrins in regulating tumor progression makes them appealing targets for cancer therapy, and some integrin antagonists have been tested in clinical trials with promising results [3]. Our results are consistent with previous studies, where HAP nanoparticles that least resembled normal bone minerals (smaller size, lower crystallinity, plate-like shape) were found to induce the most unfolded Fn conformations and correlate with the highest IL-8 secretion of breast cancer cells [1,4].

Our geologic HAP/Fn platform can readily be used to evaluate other cell types composing the metastatic microenvironment (*e.g.*, osteoblasts, endothelial cells, immune cells) that may be similarly responding to Fn conformational changes. Our preliminary results suggest that HAP surface chemistry and topography have individual effects on Fn-mediated early osteoblast adhesion (Chapter 5). We observed much higher efficiency of initial osteoblast attachment on all samples compared to that of breast cancer cells. Although the differential assembly of FAs depended both on surface chemistry and on surface topography, the latter seemed to play a predominant role. The larger size of FA complexes formed on rough HAP facets was associated with higher amounts of more compact Fn adsorbed. The interactions between Fn and osteoblasts surface receptors, in particular integrins and GAGs, were probably involved in this process. It

should be noted that both surface chemistry and topography, without the presence of Fn, can directly induce altered FA assembly, cell adhesion, and differentiation [5,6]. Further investigations and control experiments are therefore required to elucidate whether Fn mediates or simply amplifies the effects of HAP surface chemistry and topography on initial osteoblasts attachment. For example, bare HAP facets without Fn coating can be used as control surfaces to study whether HAP surface chemistry and topography have similar effects as in presence of the Fn layer on initial cell adhesion and FA assembly.

Our highly controlled 2D model system can help us better understand the role of mineral/ECM interface in regulating cell functions during breast cancer bone metastasis. It needs to be noted that surface properties such as surface ion species and hydration layer are probably different between our geologic HAP crystals and biologically relevant HAP nanoparticles [7]. Additionally, the thin Fn film adsorbed onto HAP surfaces is likely remodeled by cancer cells, especially at later stage after initial cell adhesion. Thus our FRET results are mainly relevant when interpreting initial cell responses to the underlying Fn layer. Finally, cellular behaviors in 2D culture platforms can be very different from those in 3D compliant scaffolds, although rough HAP facets present 3D microstructured features [8–10]. Nevertheless, the simplicity and high control achieved in our 2D model systems allowed us to deconvolute the effects of HAP surface chemistry and nanoscale/microscale topography on Fn-mediated cell functions, enhancing our knowledge of apatite-induced cell-ECM early interactions that may be implicated in bone metastasis. In future work, the use of 3D collagen scaffolds containing Fn and biologically relevant apatite will provide better implications for *in vivo* cell responses.

## REFERENCES

- [1] F. Wu, D.D.W. Lin, J.H. Chang, C. Fischbach, L.A. Estroff, D. Gourdon, Effect of the Materials Properties of Hydroxyapatite Nanoparticles on Fibronectin Deposition and Conformation, *Cryst. Growth Des.* 15 (2015) 2452–2460. doi:10.1021/acs.cgd.5b00231.
- [2] K. Wang, R.C. Andresen Eguiluz, F. Wu, B.R. Seo, C. Fischbach, D. Gourdon, Stiffening and unfolding of early deposited-fibronectin increase proangiogenic factor secretion by breast cancer-associated stromal cells, *Biomaterials.* 54 (2015) 63–71. doi:10.1016/j.biomaterials.2015.03.019.
- [3] J.S. Desgrosellier, D.A. Cheresh, Integrins in cancer: biological implications and therapeutic opportunities, *Nat. Rev. Cancer.* 10 (2010) 9–22. doi:10.1038/nrc2748\nrc2748.
- [4] S.P. Pathi, D.D.W. Lin, J.R. Dorvee, L.A. Estroff, C. Fischbach, Hydroxyapatite nanoparticle-containing scaffolds for the study of breast cancer bone metastasis., *Biomaterials.* 32 (2011) 5112–22. doi:10.1016/j.biomaterials.2011.03.055.
- [5] D.W. Hamilton, F. Jamshidi, D.M. Brunette, Focal adhesion mediated intracellular signaling, Stat3 translocation and osteoblast differentiation: Regulation by substratum topography, *Materwiss. Werksttech.* 40 (2009) 101–107. doi:10.1002/mawe.200800370.
- [6] J.Y. Lim, A.F. Taylor, Z. Li, E. a Vogler, H.J. Donahue, Integrin expression and osteopontin regulation in human fetal osteoblastic cells mediated by substratum surface characteristics., *Tissue Eng.* 11 (2005) 19–29. doi:10.1089/ten.2005.11.19.
- [7] D. Grossin, S. Rollin-Martinet, C. Estournès, F. Rossignol, E. Champion, C. Combes, et al., Biomimetic apatite sintered at very low temperature by spark plasma sintering: Physico-chemistry and microstructure aspects, *Acta Biomater.* 6 (2010) 577–585. doi:10.1016/j.actbio.2009.08.021.
- [8] P. Costa, T.M.E. Scales, J. Ivaska, M. Parsons, Integrin-Specific Control of Focal Adhesion Kinase and RhoA Regulates Membrane Protrusion and Invasion, *PLoS One.* 8 (2013). doi:10.1371/journal.pone.0074659.
- [9] C. Fischbach, H.J. Kong, S.X. Hsiong, M.B. Evangelista, W. Yuen, D.J. Mooney, Cancer cell angiogenic capability is regulated by 3D culture and integrin engagement., *Proc. Natl. Acad. Sci. U. S. A.* 106 (2009) 399–404. doi:10.1073/pnas.0808932106.

- [10] M.M. Martino, M. Mochizuki, D.A. Rothenfluh, S.A. Rempel, J.A. Hubbell, T.H. Barker, Controlling integrin specificity and stem cell differentiation in 2D and 3D environments through regulation of fibronectin domain stability., *Biomaterials*. 30 (2009) 1089–97. doi:10.1016/j.biomaterials.2008.10.047.

## **Appendix A.**

# **Altered Conformational and Mechanical Properties of Fibronectin Fibers in the Presence of Hydroxyapatite Nanoparticles**

Contributors: Michael Rothstein, Lara Estroff, Delphine Gourdon.

### **A.1 Introduction**

Inflammation widely occurs in physiological and pathological conditions, such as wound healing and cancer. Inflamed tissue have altered structural and mechanical properties associated with altered composition, protein conformation, and fiber network stiffness/density of the extracellular matrix (ECM) [1–3]. Meanwhile, the presence of micro-calcifications (usually calcium phosphates or oxalates) is indicative of inflammation in various tissues, including blood vessels, muscles, and skin [4–6]. It has been shown that matrix stiffness can regulate calcification by valve interstitial cells and their differentiation into pathological phenotypes [7]. However, it is unclear whether or how the formation of micro-calcifications will in turn affect matrix properties. To this end, we focus on mammary micro-calcifications, in particular hydroxyapatite, which occurs in breast cancer ductal carcinoma and is associated with a poor prognosis for certain breast cancer patients [8].

Mammary micro-calcifications occur in a significant proportion of breast cancer cases and constitute one of the most important early diagnostic markers of breast lesions. Two types of mammary micro-calcifications have been identified, calcium oxalate and hydroxyapatite (HAP),

while only the latter has been associated with malignant tumors [8]. It has been shown that the presence of HAP could promote a pro-inflammatory microenvironment by upregulating inflammatory cytokine IL-1 $\beta$  in human breast cancer cell lines [9]. HAP could also assist breast cancer cell invasion into surrounding tissues by upregulating a variety of matrix metalloproteinases [10]. There have also been studies suggesting that the chemical nature of HAP micro-calcifications is associated with tumor progression. For example, HAP calcifications formed in malignant duct contain larger amounts of proteins and less calcium carbonate than those formed in benign ducts [11]. Furthermore, the decrease in carbonate content of micro-calcification has been correlated with increasing lesion grades, or malignancy of breast tumor [12]. Therefore, the presence of HAP micro-calcifications and their materials properties could play a critical role in breast tumor progression.

Fibronectin (Fn) is a major fibrillar ECM protein and regulates a wide range of cellular behaviors via binding sites for ECM proteins, cells, and growth factors. Cells deposit Fn fiber matrix by applying forces on their surroundings to initiate assembly of Fn molecules into fibers [13,14]. The porous structure of Fn fibers makes them chemical reservoirs for growth factors that could be released from the pores when fibers are stretched (by cells). The ligand density on surface of the fiber also varies with fiber strain, which influences binding of growth factors and integrin clustering during cell attachment. Moreover, the stiffness of the fibers can be directly sensed by cells via attachments to the fibers [15].

We hypothesize that the presence and materials properties of HAP could induce altered structural and mechanical properties of the ECM, which will subsequently affect breast cancer cell functions. Specifically, HAP nanoparticles developed in Chapter 2 were used to study whether and how the presence and materials properties of HAP alter the conformational and

mechanical properties of Fn fibers. Fn fibers were manually pulled in presence or absence of HAP nanoparticles and then deposited on chemically treated polydimethylsiloxane (PDMS) trenches mounted on a customized strain device [16]. The conformation and the elastic moduli of these fibers were determined using Förster resonance energy transfer (FRET) mapping and Micro-electro-mechanical system (MEMS), respectively. FRET analysis allows detecting Fn conformation at the molecular level, while MEMS allows measuring mechanical properties at the fiber level. Preliminary results showed differential binding of HAP nanoparticles onto Fn fibers at various strain states. In addition, the incorporation of HAP nanoparticles into Fn fibers induced changes in Fn molecular conformation and mechanical properties of Fn fibers. These results provide implications for understanding the functional link between micro-calcifications and ECM structural and mechanical properties in inflamed tissues.

## **A.2 Materials and Methods**

### **A.2.1 HAP nanoparticles synthesis and characterization**

Refer to Chapter 2, section 2.3.1 and 2.3.2.

### **A.2.2 Fabrication of Fn fibers and Fn-HAP composite fibers**

Pure Fn fibers were manually pulled from a droplet of Fn solution (0.3 mg/mL Fn in PBS) at the air-water interface with a pipette tip. Fn-HAP composite fibers were pulled from solutions containing 0.3 mg/mL Fn mixed with HAP nanoparticles at concentrations ranging from 0.1 to 8.4 mg/mL in PBS.

### A.2.3 PDMS surface modification and strain device

PDMS trenches were fabricated following a previously published protocol [17]. Briefly, arrays of trenches (20  $\mu\text{m}$  deep and 50  $\mu\text{m}$  wide trenches spaced 75  $\mu\text{m}$  apart) were patterned on silicon wafers using photolithography. The silicon wafer was then coated with SIGMACOTE® (Sigma Aldrich) and dried with  $\text{N}_2$  gun. PDMS replica trenches were made by pouring degassed PDMS (1:10 curing agent to base monomer, Sigma Aldrich) onto the silicon wafer, and cured at 60 °C for 1 h. The PDMS sheet with trenches was peeled off the wafer and plasma treated for 1 min. Then the PDMS surface was functionalized with amino groups by incubation with 3% 3-aminopropyltriethoxysilane (Sigma-Aldrich) in DI water for 15 min, and washed three times with DI water. Lastly the PDMS sheet was immersed in 1% glutaraldehyde (Sigma-Aldrich) in DI water for 30 min, rinsed three times with DI water and dried with  $\text{N}_2$  gun.

The surface functionalized PDMS sheet was then mounted on a customized strain device. Fn fibers and Fn-HAP fibers were deposited on the PDMS sheet so that fibers adhered to the top of the trenches via chemical bonds. PDMS sheet was pre-strained to about 70% before fiber deposition and relaxed until about 50% of the deposited fibers began to sag (fully relaxed state). Fibers were immersed in PBS and equilibrated for at least 15 min before measurement.

### A.2.4 FRET confocal imaging

For FRET analysis, 10% FRET-labeled Fn was mixed with 90% unlabeled Fn. The PDMS sheet with fibers deposited on it was clamped onto the strain device and mounted on the stage of the microscope. 16-bit z-stack confocal images were acquired with a Zeiss 710 confocal microscope (Zeiss, Munich, Germany), using the EC Plan-Neofluar 10x/0.3 objective (zoom in 2x), a 488 nm laser set at 15% laser power, a pinhole of 1 AU, pixel dwell time of 3.15  $\mu\text{s}$ ,

PMT1 and PMT2 gains of 600 V, and z step size of 1  $\mu\text{m}$ . Emissions from donor and acceptor fluorophores were simultaneously collected in the PMT1 channel (514-526 nm) and the PMT2 channel (566-578 nm), respectively, along with bright field images acquired in the T-PMT channel (transmitted light detector). Images were analyzed with a customized Matlab code to generate FRET ratio ( $I_A/I_D$ ) images and histograms, as well as mean FRET ratios for all z-slices in a z-stack.

#### A.2.5 MEMS device

The mechanical properties of fibers were measured with a MEMS device (CCMR). Suspended fibers (over the trenches) were stretched by a tungsten tip glued onto the MEMS force sensor (Femto Tools) that proceeds in the transverse direction along the PDMS trenches. Videos were acquired using a camera. The force-displacement profile was recorded to obtain stress strain curve for each measurement. Fibers were immersed in PBS during measurement.

#### A.2.6 TEM imaging

The distribution of HAP nanoparticles within Fn fibers was characterized using the Spirit TEM (FEI), with an accelerating voltage of 120 kV. Fibers were deposited onto carbon TEM grids (Electron Microscopy Sciences), washed three times by immersing in DI water, and dried in air.

### **A.3 Results and Discussion**

#### A.3.1 Altered Fn conformations in Fn-HAP1 composite fibers

First, using FRET mapping we investigated whether the conformations of Fn molecules are altered when HAP1 nanoparticles are incorporated into Fn fibers, while the strain states of the fibers are controlled by stretching the underlying PDMS sheet with the strain device. Fiber strain was calculated by  $(L-L_0)/L_0*100\%$ , where L is the fiber length at each strain state, and  $L_0$  is the fiber length at fully relaxed state, measured from confocal bright field images. Results show that FRET ratios decreased with increasing strain for both pure Fn fibers and Fn-HAP1 composite fibers, suggesting that Fn conformation became more extended/unfolded at higher strain, which agrees with previous studies [16,18]. At low strains (less than 50%), the FRET ratios of Fn-HAP1 composite fibers were higher than those of pure Fn fibers, suggesting that the incorporation of HAP1 nanoparticles might hinder the unfolding of Fn molecules. This could be probably attributed to the strong electrostatic/polar interactions between Fn molecules and HAP1 particles, as previously discussed in Chapter 2. At high strains (more than 100%), there were not enough data to make comparison, but it seemed that the two curves started to converge, which would suggest similar Fn conformations in pure Fn fibers and Fn-HAP1 composite fibers. Therefore, the interactions between HAP1 nanoparticles and Fn molecules within the fibers might be strain-dependent.

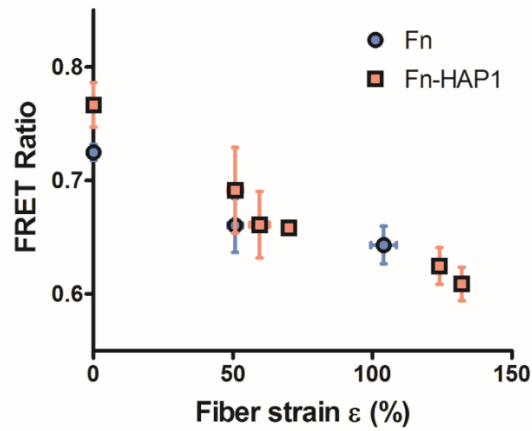


**Figure A.1** Fn conformational changes as a function of fiber strain for pure Fn fibers and Fn-HAP1 composite fibers. Fn-HAP1 fibers were pulled from solution containing 0.3 mg/mL Fn and 0.7 mg/mL HAP1 nanoparticles. Three to eight fibers were measured for each data point. Mean  $\pm$  SD.

### A.3.2 Altered mechanical properties of Fn-HAP1 composite fibers

The mechanical properties of fibers were measured with MEMS by recording the force-displacement profile to extract stress-strain curve for each fiber. Based on the geometry shown in **Figure A.2**, fiber strain is calculated using **Equation 1**:

$$\epsilon = (L-L_0)/L_0 = L/L_0 - 1 = x-1 = (1/25)*\text{SQRT}(625+D^2) - 1$$

where L is the fiber length at each strain state,  $L_0$  is the fiber length at fully relaxed state, x is the fold of extension, D is the displacement, or the distance that the tip has traveled. Assuming that the measured force F is applied by the tip symmetrically when pulling in the middle of the fiber, then the force acting on each fiber segment, f, can be derived from **Equation 2** [17]:

$$f = F/\text{SQRT}(1-1/x^2)$$

where  $F$  is the force ( $\mu\text{N}$ ) measured by the force sensor, and  $x$  is the fold of extension, which can be obtained from **Equation 1**. Assuming that the volume of the fiber remains constant during stretching, then the stress acting on the fiber is obtained using **Equation 3** [17]:

$$\sigma = f*x/A_o$$

where  $A_o$  is the cross sectional area of the fiber at fully relaxed state, and is obtained using the average fiber diameter at fully relaxed state,  $d_o$ , measured in confocal bright field images (distribution of fiber diameters are shown in **Figure A.3**), assuming spherical cross section:

$$A_o = (1/4)\pi d_o^2$$

The use of average fiber diameter is because fiber diameters cannot be accurately measured using the low magnification microscope and camera coupled to the MEMS in real time. There is no significant difference in average fiber diameter between pure Fn fibers and Fn-HAP1 composite fibers, when 2 mg/mL HAP1 nanoparticles were used (**Figure A.3**). Since diameters of these fibers can range from 1 to 6 microns, using average diameter for all fibers could introduce inaccuracy in the stress-strain curve obtained, especially for very thin and very thick fibers. In addition, the starting position of the tip, defined as just in contact with the fiber, could not be very accurately controlled due to the low magnification microscope coupled to the MEMS.

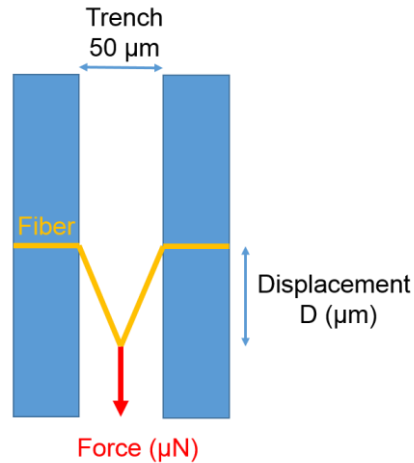


**Figure A.2** Schematic of a fiber (yellow) suspended over a trench pulled by the tip on the force sensor. Displacement is the distance that the tip travels.

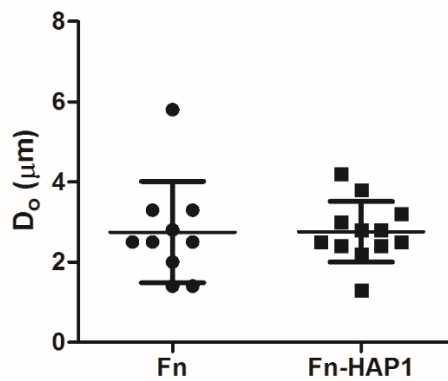


**Figure A.3** Fiber diameter measured using confocal bright field images. Fn-HAP1 composite fibers are pulled from solution containing 2 mg/mL HAP1 nanoparticles.

Using the above equations, force-strain profile of a Fn-HAP composite fiber is shown in Figure A.4. At circa 230% strain, the adhesion contact between Fn fiber and the glutaraldehyde functionalized PDMS surface was disrupted (slippage). Fiber finally fractured in the middle at

around 370% strain. However, this fracture strain is overestimated since slippage resulted in partial relaxation of the fiber. Thus the stress-strain curve of this fiber is shown up till the occurrence of slippage (**Figure A.5**). Then this stress-strain curve is fitted using a cubic model [17], and Young's modulus is obtained by differentiating the fitted curve (**Figure A.6**). Young's modulus increased nonlinearly with fiber strain, suggesting that the fiber became stiffer at higher strain.

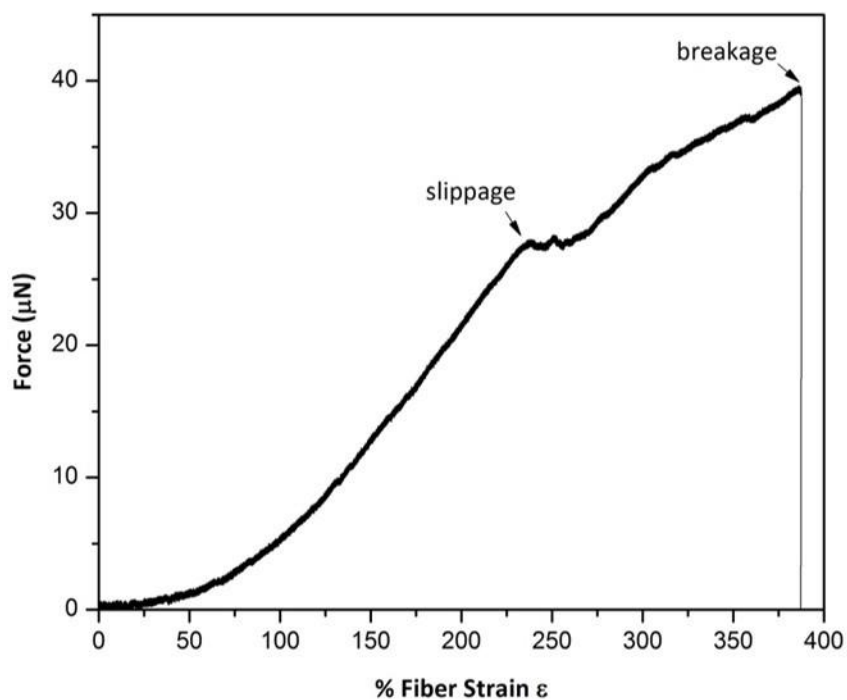


**Figure A.4** Representative force-strain profile for a Fn-HAP1 composite fiber pulled from solution containing 0.3 mg/mL Fn and 8.4 mg/mL HAP1 nanoparticles. Displacement rate 1  $\mu\text{m/s}$ .

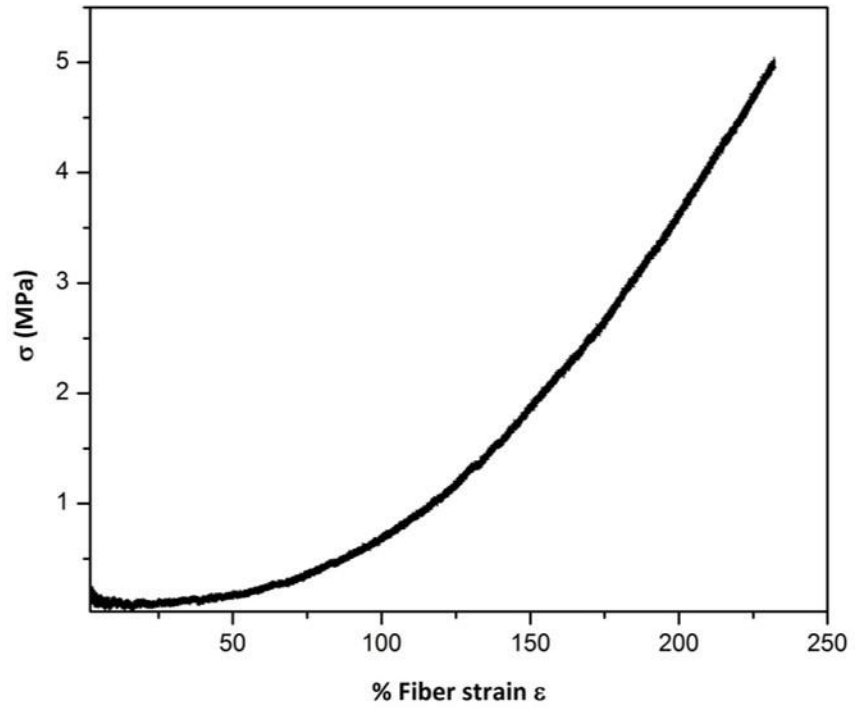


**Figure A.5** Stress-strain profile for the same Fn-HAP1 composite fiber as shown in Figure A.4 before slippage occurred.

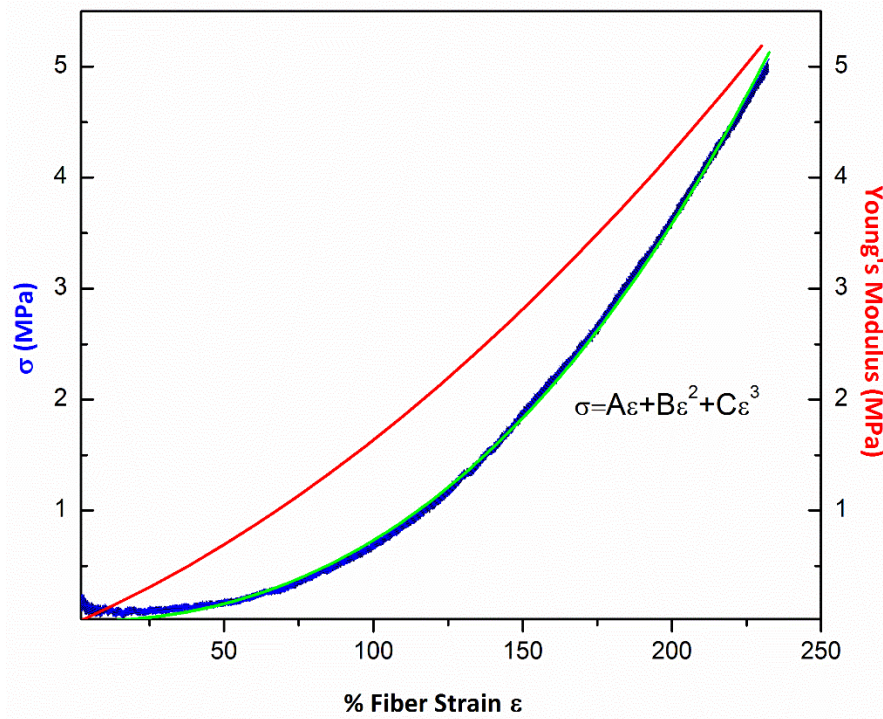


**Figure A.6** Young's modulus of the same Fn-HAP1 composite fiber as shown in Figure A.5 before slippage occurred.

However, the Young's modulus we obtained was much higher than that obtained for pure Fn fibers in previous study [17]. To test if this discrepancy is due to the presence of HAP nanoparticles, we compared stress-strain profiles between pure Fn and Fn-HAP composite fibers. **Figure A.7** shows that in fact there was a slight decrease in stiffness when HAP1 nanoparticles were incorporated, although this effect might not be significant. Therefore the higher Young's modulus we obtained is due to factors other than HAP particles. Together with the Fn conformation results, it seemed that the incorporation of HAP1 nanoparticles impeded Fn molecular unfolding and reduced the stiffness of Fn-HAP1 composite fibers, although the mechanism is unclear.

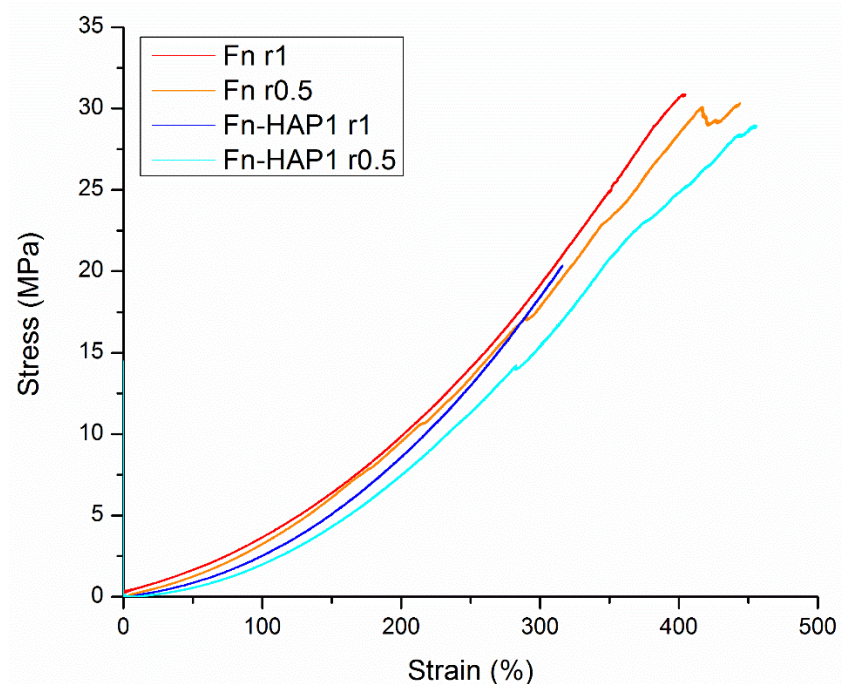


**Figure A.7** Stress-strain curves of pure Fn and Fn-HAP composite fibers. Fn-HAP fibers were pulled from solution containing 0.3 mg/mL Fn and 1 mg/mL HAP1 nanoparticles. The rate of displacement is either 1  $\mu\text{m/s}$  (r1) or 0.5  $\mu\text{m/s}$  (r0.5).

Next we investigated whether HAP materials properties affect Fn fiber mechanics. Our results showed no significant difference between Fn-HAP1 and Fn-HAP2 composite fibers (**Figure A.8**). Additionally, the displacement rates tested (1  $\mu\text{m/s}$  and 0.5  $\mu\text{m/s}$ ) didn't seem to affect fiber mechanics either, for both pure Fn and Fn-HAP composite fibers.

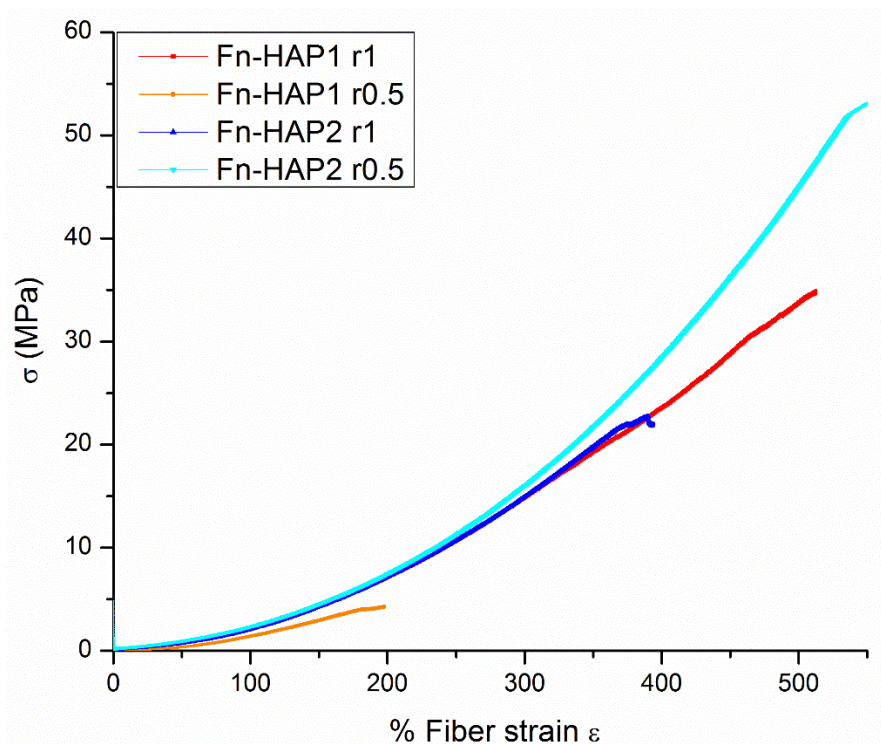


**Figure A.8** Stress-strain curves of pure Fn and Fn-HAP composite fibers. Fn-HAP fibers were pulled from solution containing 0.3 mg/mL Fn and 1 mg/mL HAP1 nanoparticles. The rate of displacement is either 1  $\mu\text{m/s}$  (r1) or 0.5  $\mu\text{m/s}$  (r0.5).

### A.3.3 Distribution of HAP1 nanoparticles within Fn-HAP1 composite fibers

Lastly the distribution of HAP1 nanoparticles within Fn fibers was investigated using TEM (**Figure A.8**). Highly inhomogeneous distribution of HAP1 within Fn fibers was observed at both low (0.01 mg/mL) and high (2 mg/mL) HAP1 concentrations. This is not surprising since we already observed the formation of HAP nanoparticle agglomerates in PBS, as well as increasing agglomerate size with HAP concentration (Chapter 2), which explains the larger clumps formed within Fn fibers at high HAP1 concentration. Due to this inhomogeneous

distribution, the mechanical properties measured are expected to depend on the local concentration of HAP nanoparticles. Therefore, measurement performed on one section of the entire fiber length might not be representative of the average mechanical properties of the entire fiber length, and a large population of fibers needs to be averaged to obtain statistically convincing results.

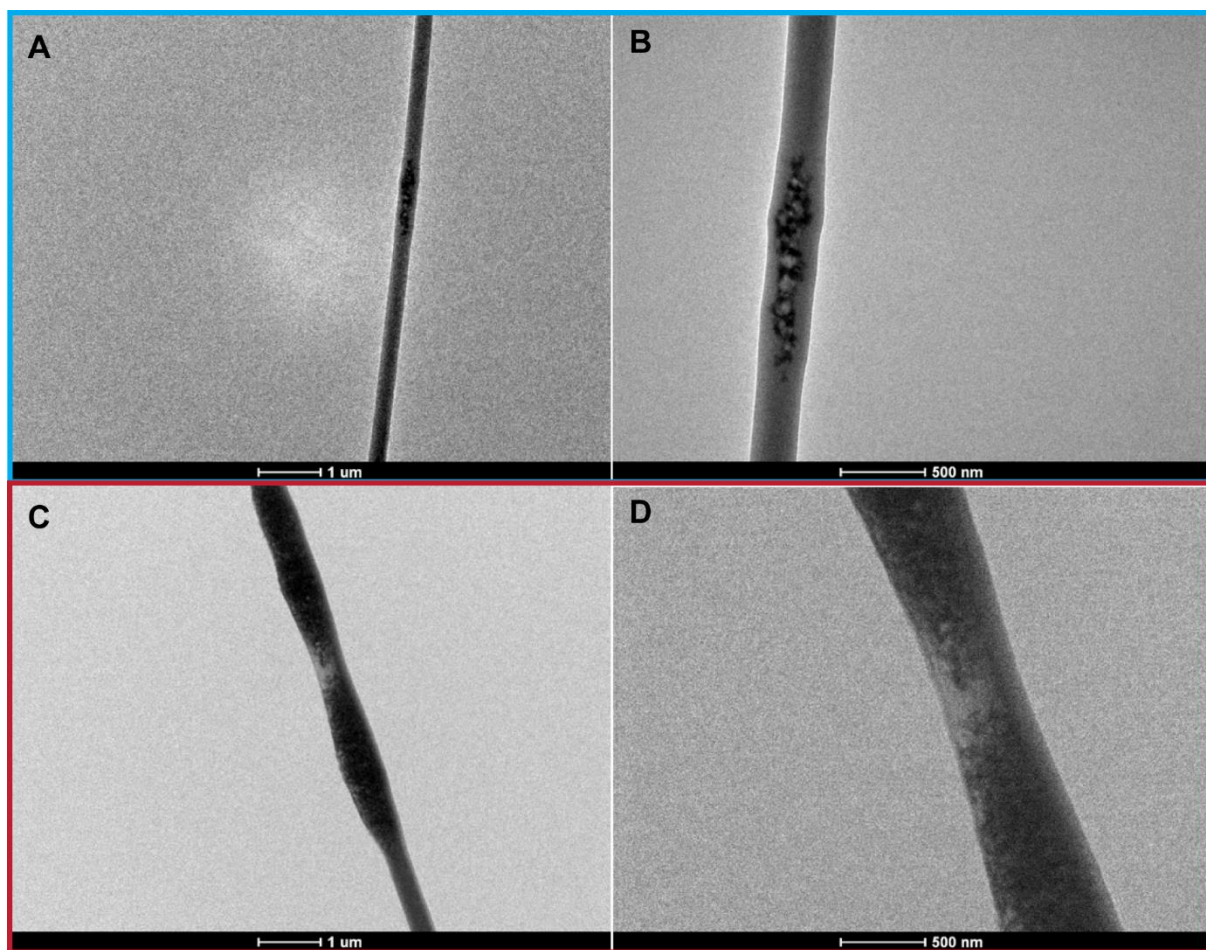


**Figure A.9** TEM images of Fn-HAP1 composite fibers pulled from solution containing 0.3 mg/mL Fn and either (A) 0.01 mg/mL HAP1 particles or (C) 2 mg/mL HAP1 particles. (B) and (D) are zoomed in images of (A) and (C), respectively.

## **A.4 Outlook**

Collectively, preliminary results obtained show that the incorporation of HAP nanoparticles could affect conformational and mechanical properties of Fn fibers, although further analysis is required to confirm these findings. Challenges that need to be resolved include inhomogeneous distribution of particles within Fn fibers, accurate measurement of fiber diameter in real time, and obtain new force sensors adapted to our system. The first challenge could be solved by surface modification of HAP nanoparticles, or sonication of the mixed Fn and HAP solution before pulling fibers. The second challenge could be addressed by coupling the MEMS to a confocal microscope. The last issue requires consulting with the company (Femto Tools) that fabricates these MEMS sensors.

## REFERENCES

- [1] L. Sorokin, The impact of the extracellular matrix on inflammation., *Nat. Rev. Immunol.* 10 (2010) 712–723. doi:10.1038/nri2852.
- [2] B.P. Toole, Hyaluronan: from extracellular glue to pericellular cue., *Nat. Rev. Cancer.* 4 (2004) 528–39. doi:10.1038/nrc1391.
- [3] B. Hinz, S.H. Phan, V.J. Thannickal, M. Prunotto, A. Desmouliere, J. Varga, et al., Recent developments in myofibroblast biology: Paradigms for connective tissue remodeling, *Am. J. Pathol.* 180 (2012) 1340–1355. doi:10.1016/j.ajpath.2012.02.004.
- [4] A.P. Sage, J. Lu, Y. Tintut, L.L. Demer, Hyperphosphatemia-induced nanocrystals upregulate the expression of bone morphogenetic protein-2 and osteopontin genes in mouse smooth muscle cells in vitro., *Kidney Int.* 79 (2011) 414–22. doi:10.1038/ki.2010.390.
- [5] L.M. Pachman, A. Veis, S. Stock, K. Abbott, F. Vicari, P. Patel, et al., Composition of calcifications in children with juvenile dermatomyositis: association with chronic cutaneous inflammation., *Arthritis Rheum.* 54 (2006) 3345–50. doi:10.1002/art.22158.
- [6] N. Eidelman, A. Boyde, A.J. Bushby, P.G.T. Howell, J. Sun, D.E. Newbury, et al., Microstructure and mineral composition of dystrophic calcification associated with the idiopathic inflammatory myopathies., *Arthritis Res. Ther.* 11 (2009) R159. doi:10.1186/ar2841.
- [7] C.Y.Y. Yip, J.-H. Chen, R. Zhao, C.A. Simmons, Calcification by valve interstitial cells is regulated by the stiffness of the extracellular matrix., *Arterioscler. Thromb. Vasc. Biol.* 29 (2009) 936–42. doi:10.1161/ATVBAHA.108.182394.
- [8] R.F. Cox, A. Hernandez-Santana, S. Ramdass, G. McMahon, J.H. Harmey, M.P. Morgan, Microcalcifications in breast cancer: novel insights into the molecular mechanism and functional consequence of mammary mineralisation., *Br. J. Cancer.* 106 (2012) 525–37. doi:10.1038/bjc.2011.583.
- [9] M.M. Cooke, G.M. McCarthy, J.D. Sallis, M.P. Morgan, Phosphocitrate inhibits calcium hydroxyapatite induced mitogenesis and upregulation of matrix metalloproteinase-1, interleukin-1 $\beta$  and cyclooxygenase-2 mRNA in human breast cancer cell lines, *Breast Cancer Res. Treat.* 79 (2003) 253–263. doi:10.1023/A:1023908307108.

- [10] M.P. Morgan, M.M. Cooke, P.A. Christopherson, P.R. Westfall, G.M. McCarthy, Calcium hydroxyapatite promotes mitogenesis and matrix metalloproteinase expression in human breast cancer cell lines, *Mol. Carcinog.* 32 (2001) 111–117. doi:10.1002/mc.1070.
- [11] A.S. Haka, K.E. Shafer-peltier, M. Fitzmaurice, J. Crowe, R.R. Dasari, M.S. Feld, Identifying microcalcifications in benign and malignant breast lesions by probing differences in their chemical composition using Raman spectroscopy., *Cancer Res.* 62 (2002) 5375–5380.
- [12] R. Baker, K.D. Rogers, N. Shepherd, N. Stone, New relationships between breast microcalcifications and cancer., *Br. J. Cancer.* 103 (2010) 1034–9. doi:10.1038/sj.bjc.6605873.
- [13] Y. Mao, J.E. Schwarzbauer, Fibronectin fibrillogenesis, a cell-mediated matrix assembly process., *Matrix Biol.* 24 (2005) 389–99. doi:10.1016/j.matbio.2005.06.008.
- [14] P. Singh, C. Carraher, J.E. Schwarzbauer, Assembly of fibronectin extracellular matrix, *Annu. Rev. Cell Dev. Biol.* 26 (2010) 397–419. doi:10.1146/annurev-cellbio-100109-104020.
- [15] M.J. Bradshaw, M.L. Smith, Multiscale relationships between fibronectin structure and functional properties., *Acta Biomater.* 10 (2014) 1524–31. doi:10.1016/j.actbio.2013.08.027.
- [16] M.L. Smith, D. Gourdon, W.C. Little, K.E. Kubow, R.A. Eguiluz, S. Luna-Morris, et al., Force-induced unfolding of fibronectin in the extracellular matrix of living cells., *PLoS Biol.* 5 (2007) e268. doi:10.1371/journal.pbio.0050268.
- [17] E. Klotzsch, M.L. Smith, K.E. Kubow, S. Muntwyler, W.C. Little, F. Beyeler, et al., Fibronectin forms the most extensible biological fibers displaying switchable force-exposed cryptic binding sites., *Proc. Natl. Acad. Sci. U. S. A.* 106 (2009) 18267–72. doi:10.1073/pnas.0907518106.
- [18] W.C. Little, M.L. Smith, U. Ebnetter, V. Vogel, Assay to mechanically tune and optically probe fibrillar fibronectin conformations from fully relaxed to breakage., *Matrix Biol.* 27 (2008) 451–61. doi:10.1016/j.matbio.2008.02.003.

## **Appendix B.**

# **Fibronectin Conformation on Mica Surfaces as a Function of Curvature**

Contributors: Roberto C. Andresen Eguiluz, and Delphine Gourdon.

## **B.1 Introduction**

Fibronectin (Fn) coated mica surfaces glued on silica discs were used for investigating the role of Fn in mediating enhanced wear protection of lubricin during shear, using surface forces apparatus (SFA) [1]. The conformation of Fn adsorbed onto mica surfaces were measured via FRET. The aim of this experiment was to assess whether the use of silica discs with various curvatures would influence Fn conformation, and help elucidate the interactions between Fn and components of the synovial fluid, such as lubricin, hyaluronan, and serum albumin, which are all believed to contribute to joint lubrication.

## **B.2 Materials and Methods**

### **B.2.1 Preparation of mica surfaces**

Freshly cleaved mica surfaces were glued onto half cylindrical silica discs with various curvature (flat, radius of curvature  $R = 2$  cm, 1 cm, or 0.5 cm) with UV curing glue (Norland 61, Cranbury, NJ) and exposed for 45 min under UV lamp in laminar flow cabinet.

### B.2.2 FRET imaging and analysis

For FRET analysis, 100  $\mu\text{L}$  of Fn solutions (50  $\mu\text{g}/\text{mL}$ ) containing 10% FRET labeled Fn (Batch K1, refer to Chapter 2, **Figure 2.6**) and 90% unlabeled Fn in PBS were incubated on mica surfaces glued on silica discs. Fn-coated mica surfaces were incubated at 4  $^{\circ}\text{C}$  for 24 h, rinsed three times with PBS, and kept immersed in PBS. 16-bit z-stack confocal images were acquired with a Zeiss 710 confocal microscope (Zeiss, Munich, Germany), using the C-Apochromat 40x/1.20 W objective, a 488 nm laser set at 30% laser power, a pinhole of 2 AU, pixel dwell time of 6.3  $\mu\text{s}$ , PMT1 and PMT2 gains of 600 V, and z step size of 1  $\mu\text{m}$ . Emissions from donor and acceptor fluorophores were simultaneously collected in the PMT1 channel (514-526 nm) and the PMT2 channel (566-578 nm), respectively, along with bright field images acquired in the T-PMT channel (transmitted light detector). Images were analyzed with a customized Matlab code to generate FRET ratio ( $I_A/I_D$ ) images and histograms, as well as mean FRET ratios for all z-slices in a z-stack.

### B.2.3 Statistical analysis

One-way ANOVA with Tukey's post test and Student's t-test were used to determine statistical significance between conditions in GraphPad Prism (GraphPad Software, Inc., CA). In all cases,  $p < 0.05$  is indicated by a single star,  $p < 0.01$  by two stars and  $p < 0.001$  by three stars.

## B.3 Results and Discussion

FRET ratios of Fn adsorbed on mica surfaces increased with increasing curvature of mica, suggesting that Fn conformation became more compact when adsorbed on mica surfaces with a

larger curvature. Previous studies have shown that nanoroughness of substrates enhances protein adsorption and induces conformational changes of proteins, such as Fn [2,3]. Additionally, local surface geometry of nanomaterials, such as curvature of nanoparticles and nanopores, can also significantly affect protein conformation, especially when the characteristic sizes of the nanomaterial and the protein are comparable [4,5]. However, it is surprising that centimeter-scale curvature could also induce Fn conformational changes. According to the FRET calibration curve for the FRET-Fn used in this experiment (Chapter 2, **Figure 2.6**), most Fn molecules adopted unfolded conformations when adsorbed on mica surfaces, regardless of surface curvature. It should be noted that Fn conformation adsorbed on mica has been shown to depend on surface coverage [6]. Therefore, more compact Fn conformations may be observed when using higher Fn concentration for incubation.

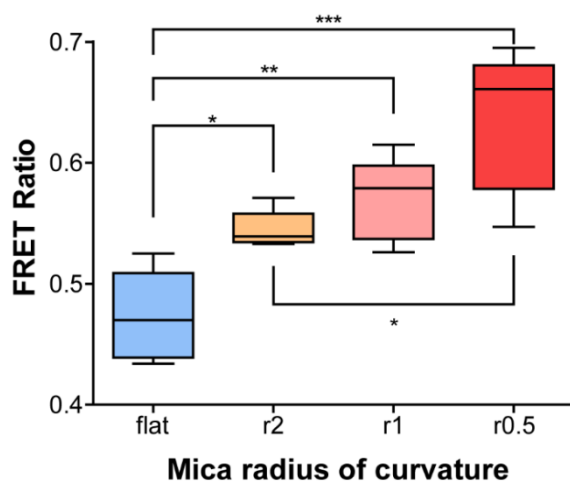


**Figure B.1** FRET ratios of Fn molecules adsorbed on freshly cleaved mica surfaces at 4 °C for 24 h: either flat mica or mica surfaces with radius of curvatures of 2 cm (r2), 1 cm (r1), and 0.5 cm (r0.5) were used. N = 5. In all cases,  $p < 0.05$  is indicated by a single star,  $p < 0.01$  by two stars and  $p < 0.001$  by three stars.

## **B.4 Outlook**

Our results show that the centimeter-scale curvature of mica surfaces could significantly affect conformation of adsorbed Fn molecules. More compact Fn conformations were detected on mica surfaces with higher curvatures. However, the mechanism of this surface curvature effect is still unclear. These results suggest that Fn conformation is not only sensitive to surface chemistry, nanoscale, and micro-scale topography/morphology, but also to macroscale curvature of underlying surfaces. Future experiments using various Fn coating concentrations, and other types of surfaces will help us better understand whether this curvature effect is dependent on surface coverage, and if it is a ubiquitous phenomenon on many types of surfaces.

## REFERENCES

- [1] R.C. Andresen Eguiluz, S.G. Cook, C.N. Brown, F. Wu, N.J. Pacifici, L.J. Bonassar, et al., Fibronectin mediates enhanced wear protection of lubricin during shear, *Biomacromolecules*. 16 (2015) 2884–2894. doi:10.1021/acs.biomac.5b00810.
- [2] M.H. Lee, P. Ducheyne, L. Lynch, D. Boettiger, R.J. Composto, Effect of biomaterial surface properties on fibronectin- $\alpha 5\beta 1$  integrin interaction and cellular attachment., *Biomaterials*. 27 (2006) 1907–16. doi:10.1016/j.biomaterials.2005.11.003.
- [3] M.B. Hovgaard, K. Rechendorff, J. Chevallier, M. Foss, F. Besenbacher, Fibronectin adsorption on tantalum: the influence of nanoroughness., *J. Phys. Chem. B*. 112 (2008) 8241–9. doi:10.1021/jp801103n.
- [4] L.-C. Sang, M.-O. Coppens, Effects of surface curvature and surface chemistry on the structure and activity of proteins adsorbed in nanopores., *Phys. Chem. Chem. Phys.* 13 (2011) 6689–98. doi:10.1039/c0cp02273j.
- [5] P. Elter, R. Lange, U. Beck, Atomic force microscopy studies of the influence of convex and concave nanostructures on the adsorption of fibronectin., *Colloids Surf. B. Biointerfaces*. 40 (2012) 139–46. doi:10.1016/j.colsurfb.2011.09.021.
- [6] J.R. Hull, G.S. Tamura, D.G. Castner, Structure and reactivity of adsorbed fibronectin films on mica., *Biophys. J.* 93 (2007) 2852–60. doi:10.1529/biophysj.107.109819.